

Published in final edited form as:

Prog Mater Sci. 2015 March 1; 68: 1–66. doi:10.1016/j.pmatsci.2014.10.002.

Advantages and Challenges of Relaxor-PbTiO₃ Ferroelectric Crystals for Electroacoustic Transducers- A Review

Shujun Zhang^{1,*}, Fei Li², Xiaoning Jiang³, Jinwook Kim³, Jun Luo⁴, and Xuecang Geng⁵

¹Materials Research Institute, Pennsylvania State University, University Park, PA, 16802, US

²Electronic Mater. Res. Lab, Key Lab Ministry of Education and International Center for Dielectric Research, Xi'an Jiaotong University, Xi'an 710049, China

³Department of Mechanical and Aerospace Engineering, North Carolina State University, Raleigh, North Carolina 27695, US

⁴TRS Technologies Inc., 2820 E. College Ave., Suite J, State College, PA, 16801, US

⁵Blatek Inc., 2820 E. College Ave., Suite F, State College, PA, 16801, US

Abstract

Relaxor-PbTiO₃ (PT) based ferroelectric crystals with the perovskite structure have been investigated over the last few decades due to their ultrahigh piezoelectric coefficients ($d_{33} > 1500$ pC/N) and electromechanical coupling factors ($k_{33} > 90\%$), far outperforming state-of-the-art ferroelectric polycrystalline Pb(Zr,Ti)O₃ ceramics, and are at the forefront of advanced electroacoustic applications. In this review, the performance merits of relaxor-PT crystals in various electroacoustic devices are presented from a piezoelectric material viewpoint. Opportunities come from not only the ultrahigh properties, specifically coupling and piezoelectric coefficients, but through novel vibration modes and crystallographic/domain engineering. Figure of merits (FOMs) of crystals with various compositions and phases were established for various applications, including medical ultrasonic transducers, underwater transducers, acoustic sensors and tweezers. For each device application, recent developments in relaxor-PT ferroelectric crystals were surveyed and compared with state-of-the-art polycrystalline piezoelectrics, with an emphasis on their strong anisotropic features and crystallographic uniqueness, including engineered domain - property relationships. This review starts with an introduction on electroacoustic transducers and the history of piezoelectric materials. The development of the high performance relaxor-PT single crystals, with a focus on their uniqueness in transducer applications, is then discussed. In the third part, various FOMs of piezoelectric materials for a wide range of ultrasound applications, including diagnostic ultrasound, therapeutic ultrasound, underwater acoustic and passive sensors, tactile sensors and acoustic tweezers, are evaluated to provide a thorough understanding of the materials' behavior under operational conditions. Structure-property-performance relationships are

© 2014 Elsevier Ltd. All rights reserved.

*Corresponding author: soz1@psu.edu; shujunzhang@gmail.com.

Publisher's Disclaimer: This is a PDF file of an unedited manuscript that has been accepted for publication. As a service to our customers we are providing this early version of the manuscript. The manuscript will undergo copyediting, typesetting, and review of the resulting proof before it is published in its final citable form. Please note that during the production process errors may be discovered which could affect the content, and all legal disclaimers that apply to the journal pertain.

then established. Finally, the impacts and challenges of relaxor-PT crystals are summarized to guide on-going and future research in the development of relaxor-PT crystals for the next generation electroacoustic transducers.

Keywords

Relaxor-PT; Ferroelectric; Piezoelectric; Crystals; Transducers; Electroacoustic

I. Introduction

1.1 General information on electroacoustic transducers

An electroacoustic transducer is a type of device that transforms an electrical signal into acoustic waves or converts an acoustic wave to an electrical signal, or, in many cases, operates in both directions. Electroacoustic transducers are versatile and include magnetostrictive, electrostatic and piezoelectric devices, among which piezoelectric transducers are the most commonly used in a diverse range of applications, such as industrial nondestructive evaluations, underwater acoustics, medical ultrasonics for diagnostics and therapy, ultrasonic cleaning, and material processing, to name a few [1–9]. The operational frequency range varies greatly depending on the applications. For example, common frequencies of 2 to 10 MHz are used in nondestructive testing and evaluation to locate flaws in materials, but lower frequencies can also be used to inspect low density materials. Medical diagnostic transducers generally operate in the frequency range of 2 to 18 MHz, though frequencies up to 50–100 MHz have been used for intravascular, ophthalmic, skin imaging and small animal imaging. The useful spectrum of underwater acoustic extends from sub-audible and audible frequencies allowing for great distances (one to several kilometers) to ultrasonic frequencies (up to > 1 MHz) where echo distances are shorter and increase accuracy of distance measurements is desirable [3,7]. Applications over this wide frequency range require numerous transducer designs. A number of geometries have been demonstrated, resulting in effective underwater acoustic transducers [10]. Each design offers a number of advantages and disadvantages associated with the geometry of the transducer. Common transducer designs include but are not limited to the following: flextensional “cymbal” transducers, where the piezoelectric active material is sandwiched between two mechanical end caps, and the primary axis of mechanical motion is perpendicular to the primary axis of acoustic radiation [10–13]; 1–3 (or 2–2) composite transducers, where a series of piezoelectric pillars (or sheets) are arranged with a predetermined lateral spacing and filled with a mechanically lossy polymer matrix, which operates in an effective longitudinal (or sliver) mode, thus offering greater bandwidth and improved acoustic impedance matching with water or tissue [10,14–20]; and tonpils transducers (Langevin transducers), where stacked piezoelectric rings are connected with a head and a tail mass resulting in longitudinal operational mode [3,10,21–22]. These underwater acoustic devices are useful in ocean engineering in many ways. For example, the precise location of specific points or objects is often critical when drilling for oil and gas in the deep ocean or laying underwater cables or pipelines, while the combination of underwater and seismic acoustics is needed for finding deposits of oil or gas under the oceans [3].

The first attempt to use ultrasound transducer for medical diagnosis was based on a transmission technique by the Dussik brothers in 1937, working in Austria [8,9]. Research into medical applications of ultrasound is usually said to have started with the work of Wood and Loomis [23], who made a comprehensive study of both the physical and biological effects of ultrasound on biological media. An extensive literature list soon started to develop, particularly after 1954, when the first compound B-scan imaging system was reported. Ultrasonics has since found usage in numerous aspects of medical procedures, including diagnostic (low power), therapeutic (intermediate power), and surgical (high power in several forms, such as heat and mechanical) applications [2]. Ultrasonic wave propagation in body tissue is, in large measure, controlled by the acoustic impedance contrast at boundaries and various scattering mechanisms presented at the different scales within tissue, such as velocity and attenuation factors. These are the basic factors that determine the effectiveness of both diagnostic and therapeutic applications of ultrasound [2].

Recent decades have seen a second revolution in electroacoustic transducers, which benefit from modern electronics as well as with increasing digitization and computer-based data processing, imaging capability to deliver in-situ processing and advanced display/visualization capabilities [2]. These advances have been combined to facilitate new applications at both low and high powers using modern instrumentation and analysis capabilities, leading to major growth and diversification of electroacoustic applications, which in turn drive the developments of new transducer materials [2–4].

1.2 History of piezoelectric materials for transducers

Piezoelectric materials are the heart of piezoelectric transducers and sensors [24–34]. Fig. 1 gives a general milestone map for piezoelectric transducer material development as a function of their respective piezoelectric performance. The piezoelectric effect was first found in 1880 by Pierre and Jacques Curie [35]. They discovered that a stress applied to crystals, such as quartz, produced an electric charge on the surface (direct effect). Conversely, an electric field applied to the surfaces produced a change in the dimensions, and hence an alternating voltage applied to a crystal produced acoustic waves in the surrounding medium. Quartz piezoelectric crystal was used as a transducer material in 1917 by Langevin, who designed the first electroacoustic transducer by sandwiching quartz between steel plates [2,3]. Rochelle salt (sodium potassium tartrate tetrahydrate) crystal was first synthesized in 1655, but its ferroelectricity and subsequent piezoelectric were demonstrated later by Valasek in 1921 [36–38], showing a stronger piezoelectric effect than quartz, and also became available in the form of synthetic crystal to provide an alternate for the electroacoustic transducers [38]. However, Rochelle salt was found to be not stable against dehydration either in vacuum or in dry air. In addition, Rochelle salt is one of few ferroelectric crystals with limited ferroelectric range and two clear Curie points [38–39]. Motivation of exploring new man-made transduction materials lead to the discovery and development of potassium dihydrogen phosphate (KDP) [40] and ammonium dihydrogen phosphate (ADP) [41] crystals in 1935 and the early 1940's, in which the structural arrangement of phosphate tetrahedral is linked by hydrogen bonding at the corners, showing relatively strong piezoelectric activity. It was generally accepted that ferroelectricity was highly correlated with the hydrogen bonds in the early Rochelle salt and KDP/ADP periods

[6,38,42–43]. The ADP crystals were then established as extremely useful for high power acoustic transducers, replacing Rochelle salt [43]. Up to 1945, the principal ultrasonic transducer materials were natural quartz and ADP crystals [3].

In the early 1940's, a breakthrough was achieved by the use of ferroelectrics that can be obtained in polycrystalline ceramic form. The first of these ferroelectrics, barium titanate (BaTiO_3), with the perovskite structure based upon corner linking of oxygen octahedra, was discovered independently by Von Hippel [44] and Goldman [45]. The first working piezoelectric ceramic transducer can be credited to Gray in 1945, who had the first clear understanding of the importance of electrical poling in establishing a remnant polar domain configuration in the ceramics and corresponding strong piezoelectric response [46]. By the early 1950s, ceramic piezoelectric transducers based on BaTiO_3 (BT) were well established in a number of both civil and military applications [38,47]. However, due to the concerns about the stability against depoling - accompanied by multi polymorphic phase transitions (PPTs) in pure BT - and the low field stability (low coercive field E_C) [38, 48–50], it was necessary to explore other ferroelectric perovskite compounds with enhanced performance [51–53]. Some of the very early basic work on pure PbTiO_3 and PbZrO_3 - PbTiO_3 (PZT) solid solution systems led to the useful outline of its phase diagram [54–56]. The milestone studies, which established the PZT system as exceptionally suitable piezoelectric material formulations, were carried out by Jaffe et al., who discovered that the nearly temperature-independent morphotropic phase boundary (MPB) in PZT was of vital importance for transducer applications, due to the abnormally high piezoelectric and electromechanical properties near the MPB compositions [57–62]. The leading position of PZT compositions was due to their strong piezoelectric effect and relatively high Curie temperature. PZTs also allowed a wide variation in chemical modification to obtain a wide range of operating parameters without serious reduction of the piezoelectric effect, where the chemical dopants included isovalent substitutes of the lead cation by base earth elements and acceptor or donor dopants on the A or B sites [61–62]. Most effects of acceptor or donor doping were attributed to the type of lattice vacancies that arose, where oxygen vacancies induced by acceptor dopants inhibited domain wall motion, while lead vacancies induced by donor dopant made the domain wall motion easier, leading to different “hard” and “soft” characteristics, respectively [63–68]. A series of formulation-labeled PZT (PZT4, PZT5A, PZT5H, PZT8, etc.) have been established to emphasize various properties. Table I summarizes several commercially available PZT ceramics which have been extensively used for more than 60 years [69–71]. It can be seen that different compositions are outstanding with regard to different characteristics and thus beneficial to different applications. The high electromechanical coupling and piezoelectric coefficient of PZT5H have led to its use in medical imaging transducers, while PZT5A is a better choice for sensing applications due to its high piezoelectric voltage coefficient and higher Curie temperature. Meanwhile, the high resistivity of the donor doped PZTs at elevated temperatures allows usage to very low frequencies (the low limit frequency of the materials is inversely proportional to the time constant $RC = \epsilon_0 K \rho$, where ϵ_0 is the vacuum permittivity, K , the dielectric constant and ρ , the resistivity). On the contrary, the low mechanical and dielectric losses of PZT4 and PZT8 compositions benefits applications in high power transducers and ultrasonic motors requiring high drive fields. Other formulations, such as PZT6 and PZT7, also found usage in

specific applications, where high temperature/time stability and low permittivity are desired, respectively [38, 69–71].

Undoubtedly, the PZT family is, by far, the most important and versatile compositional base for piezoelectric elements. In addition to PZTs, other developments in ferroelectric materials are also of major interest. In 1952, studies by Goodman uncovered the interesting and strong ferroelectric properties in lead metaniobate (PbNb_2O_6 ; PN) with a tungsten bronze structure [38,72]. It exhibits unusual properties not generally present in other piezoelectric materials and has been the subject of considerable research because of its high hydrostatic sensitivity (due to its large anisotropy, allowing a better response under hydrostatic pressures), low mechanical Q_m (being only $\ll 20$, benefiting the fabrication of wide bandwidth transducers for high frequency pulse echo measurements that require a short pulse and critical resolution) and negligible aging in a wide temperature range due to its high Curie temperature [38,73–75]. The metaniobate is a problematic ceramic to process, but easily forms solid solution with other end members such as BaNb_2O_6 with decreased Curie temperature [76], and thus has been specialized for industrial nondestructive evaluation/testing (NDE/NDT) applications. Another development in piezoelectric materials is crystal growth of LiNbO_3 (LN) and LiTaO_3 (LT) [77–79], which were synthesized for the first time in Bell laboratories and their ferroelectric properties revealed by Matthias and Remeika [80]. Both crystals have an ilmenite structure [81]. The detailed structure and properties were reviewed by Smith et al. [82] and Weis et al. [83]. Both LN and LT are well known for their low acoustic losses and are thus excellent materials for surface acoustic wave (SAW) devices [77–78]. LN, possessing relatively large electromechanical coupling factors and very high Curie temperature of 1150 °C, has been actively studied for high temperature acoustic transducer [84–86]. In addition, it has been studied for high frequency (>20MHz), broad bandwidth single-element transducer applications due to its very high acoustic velocity and low dielectric constant [87–88]. LN possesses a number of useful orientation-controlled crystal cuts, which are now extensively used in transducer applications, including compression 36° rotated y-cut and shear 163° rotated y-cut.

In the 1970s, it was deemed that further improvements in the performance of established piezoelectrics were not forthcoming. Thus, various piezoelectric composites were introduced by Newnham in 1978, through the concept of “engineered biphasic connectivity” [14]. The particular significance of piezoelectric composites is that the structurally and compositionally homogeneous ceramics or single crystals can be combined with a passive polymer material to form composites, increasing material flexibility and improving acoustic impedance matching between the active material and the medium in which the acoustic wave travels. By structurally combining a piezoelectric ceramic and a polymer with certain connectivity, the resulting composite material can successfully integrate the advantages of both materials. Several interesting connectivity patterns were developed, including 0–3, 1–3 and 2–2 structures, and are now being widely employed in transducer applications [13–20,89–110].

Another very important transduction material category is relaxor based ferroelectrics [111–117], with a partially disordered structure and polar nanoregion (PNR), leading to extremely large dielectric constant. One such material is lead magnesium niobate (PMN), first reported

in 1961 [118]. The large dielectric constant benefits the electric field induced strain level through the electrostrictive coefficient, with the advantage of very low strain hysteresis, causing PMN to be actively studied for medical and underwater transducer applications [119–125]. Analogous to PZT system, the relaxor components can form solid solutions with classic ferroelectric PT, possessing MPB regions and ultrahigh dielectric and piezoelectric properties [126–136]. Of particular importance is that some of the relaxor-PT ferroelectric solid solutions can be grown into single crystals, such as $\text{Pb}(\text{Mg}_{1/3}\text{Nb}_{2/3})\text{O}_3\text{-PbTiO}_3$ (PMN-PT) and $\text{Pb}(\text{Zn}_{1/3}\text{Nb}_{2/3})\text{O}_3\text{-PT}$ (PZN-PT). The first attempt on the crystal growth started in the early 1980s [137–138], but extensive studies on the relaxor-PT crystals have occurred since the late 1990s. The crystals were found to exhibit high electric field induced strains ($\sim 1.7\%$) and high electromechanical couplings (~ 0.9) [139–140], demonstrating the potential for improvement over PZT in electroacoustic transducer applications, which are the target piezoelectric materials in this review article.

1.3 Scope of Review

Relaxor-PT single crystals have attracted significant attention and have been actively studied over the last 20 years. Focus on the fundamental understanding of the origin of ultrahigh piezoelectricity and their merits in practical electromechanical applications, showing uniqueness and advantages of the crystals over state-of-the-art polycrystalline ceramics. Several review articles have been written on the crystal growth, property characterizations, piezoelectric mechanisms and related applications [141–154]. However, there have been no review articles surveying the “figure of merits” of relaxor-PT single crystals for various electroacoustic applications, which is very important for the material and device scientists to understand the material behavior under practically operational conditions. This review article provides an understanding of the material structure-property-device performance relationships of relaxor-PT crystals and corresponding applications, which may help the readers to better understand the materials from an application viewpoint and the acoustic devices from a functional material aspect.

II. The development of Relaxor-PT single crystals

2.1 Background

Single crystal PMN was initially reported in the early 1960s, and it was not until the early 1970s that another relaxor ferroelectric material, lead zinc niobate PZN, was reported. It was found that single crystals in the PZN-PT system could be readily grown from high temperature PbO flux [137–138]. Following studies on PZN-PT single crystals in the early 1990s [155–156], systematic studies on the piezoelectric properties of Relaxor-PT crystals poled along different crystallographic directions were reported in late 1990s and early 2000s. They showed ultrahigh piezoelectric coefficients and electromechanical coupling factors on the order of >1500 pC/N and > 0.9 respectively, far outperforming state-of-the-art ferroelectric PZT ceramics and triggering interest in crystals for various applications [157–237]. Today, relaxor ferroelectric PMN-PT crystals continue to be an exciting research area that promises even further discoveries, and have been commercialized with the help of the mature Bridgman crystal growth method [187,207,210,229,230]. However, issues of PMN-PT crystals include their low Curie temperature and ferroelectric phase transition

temperatures, low coercive field and mechanical quality factor (for high power applications). The Curie temperature T_C , rhombohedral-to-tetragonal ferroelectric phase transition temperature T_{RT} and coercive field E_C determine the temperature and field stabilities, which are major concerns for many electroacoustic applications. In addition, low T_C , T_{RT} and low E_C bring up the issues of polarization stability under various maintenance storage and driving conditions [141]. Therefore, a dc bias electric field may be required to maintain the polarization and the performance of the devices [18]. Loss in sensitivity, however, occurs when applying a dc bias, which also adds complexity and cost to the driving electronics [171]. Furthermore, though having low dielectric loss (~ 0.002 , similar to hard PZTs), the low mechanical quality factors Q_m of PMN-PT crystals, ~ 100 , have been limiting factors in high power transducers and resonance based acoustic devices [166,195,196]. Owing to the above issues observed in PMN-PT crystals, it is desired to develop new single crystal systems with broadened temperature usage range and improved reliability under thermal/electric field, and mechanical stress [141–142].

Over the last ten years, extensive effort has been focused on new crystal systems, including binary [238–268] and ternary [269–315] relaxor-PT crystal systems, in which $\text{Pb}(\text{Mg}_{1/3}\text{Nb}_{2/3})\text{O}_3\text{-PbZrO}_3\text{-PbTiO}_3$ (PMN-PZT) [269–275] and $\text{Pb}(\text{In}_{0.5}\text{Nb}_{0.5})\text{O}_3\text{-Pb}(\text{Mg}_{1/3}\text{Nb}_{2/3})\text{O}_3\text{-PbTiO}_3$ (PIN-PMN-PT) [278–289] have been actively studied due to the potential growth ability of large size and high quality crystals. With new developments in the relaxor-PT single crystals in 2010, the concept of various generation crystals was proposed by Smith [141,316]. The first generation crystals exhibit high electromechanical coupling and piezoelectric coefficients that produce transducers with larger bandwidth ($\times 2$) and higher sensitivity (+10 dB) when compared with the state-of-the-art polycrystalline ceramic technology, which already have been commercialized in medical ultrasonic imaging [139–140]. Second generation crystals extend the high electromechanical properties to a broader range of temperature, electric field and mechanical stress, expanding their design envelope by reducing the need for heat shunts and applied dc fields. Crystals with higher ferroelectric phase transition temperatures and higher coercive fields are in this category [141,153,275,278], where the potential commercialization of the ternary PIN-PMN-PT and PMN-PZT is expected. Third generation crystals include the addition of small amount of dopants to tailor the crystal's electromechanical parameters in order to meet specific device requirements. For example, Mn-doped relaxor-PT crystals have been developed, with greatly increased mechanical quality factors and high piezoelectric properties [273,296,298], which will benefit resonance based devices, such as ultrasonic transducers and motors. The detailed comparison of the three generations of crystal systems are given in Table II [161,273,278,290,304,317]. It was observed that the 2nd and 3rd generation crystals possess comparable piezoelectric and electromechanical properties to those of 1st generation crystals, but with higher ferroelectric phase transition temperatures ($\sim 30^\circ\text{C}$ higher) and higher coercive fields (double the value of 1st Gen), allowing for broader temperature usage and higher drive fields /increased signal intensities. In addition, the mechanical quality factor of 3rd generation crystals is about 5–10 times higher than those of 1st and 2nd generation crystals, offering the possibility for high power transducer applications.

2.2 General observations of relaxor-PT single crystals: Properties vs T_C and T_{RT}

Generally, the Curie temperature and ferroelectric phase transition temperature (polymorphic phase transition: PPT) are important parameters to evaluate the performance of ferroelectric materials, due to the fact that these temperatures not only relate to the material structures, but also determine the temperature usage range and temperature stability of the material properties. In polycrystalline ferroelectric materials, knowledge of the Curie temperature shows a strong relationship of dielectric and piezoelectric properties with T_C [157,318]. For relaxor-PT single crystals, however, both T_C and PPT (T_{RT}) must be considered, due to the strongly curved MPB. Thus, it is desirable to understand the general relationships, if any, for relaxor-PT single crystal systems.

Fig. 2 shows the room temperature electromechanical coupling factor (k_{33}) and piezoelectric coefficient (d_{33}) of [001]-oriented relaxor-PT-based ferroelectric single crystals as a function of Curie temperature T_C and/or rhombohedral–tetragonal phase transition temperature T_{RT} [242,252,279,305,318–328]. Fig. 2(a) depicts the electromechanical coupling k_{33} as a function of Curie temperature for various crystals with compositions near their respective MPBs, where k_{33} values were found to be on the order of 0.9 for all [001] domain-engineered rhombohedral relaxor-PT crystals, regardless of their phase transition temperatures (T_C or T_{RT}). From Fig. 2(b), however, the levels of piezoelectric coefficients (d_{33}) were found to decrease with increasing T_{RT} , other than T_C as observed for polycrystalline ceramics [167]. Thus, relaxor-PT single crystals possessing MPB compositions exhibit higher dielectric and piezoelectric properties, but lower ferroelectric phase transition temperatures and deteriorated thermal stability of the properties when compared to the rhombohedral compositions far away from MPB. The general trend of coercive field of [001]-oriented ferroelectric single crystals as a function of Curie temperature is shown in Fig. 3, where E_C was found to increase with increasing T_C [163,318]. It is of interest to note that for the same crystal system, tetragonal compositions were found to possess significantly higher coercive fields when compared with their rhombohedral counterparts, not just higher T_C . The 90° ferroelastic domain walls and high c/a ratio (c and a are the crystal lattice parameters) make the main contributions to the enhanced coercive field [373].

2.3 The uniqueness of relaxor-PT single crystals

Relaxor-PT based ferroelectric single crystals offering high performance with ultra-high electromechanical coupling and piezoelectric coefficient far out-perform state-of-the-art piezoelectric PZTs, attracting extensive attention to these crystal systems in last 20 years. In addition, the crystals exhibit several unique properties inherently associated with the engineered domain configurations, which are not existent in polycrystalline ceramics. In this section, the uniqueness of relaxor-PT crystals, including crystallographic anisotropy, high intrinsic piezoelectric, high cryogenic properties and newly developed shear vibration modes, will be discussed.

2.3.1 Crystallographic Anisotropic Characteristics

Polycrystalline ceramics such as PZT are in $\infty\infty m$ symmetry with inversion center in their unpoled status, transfer to ∞m symmetry after poling, exhibiting piezoelectric activity. Contrary to ceramics, relaxor-PT

single crystals are in macroscopic $4mm$, $mm2$ and $3m$ symmetries when poled along their crystallographic [001], [011] and [111] directions respectively, leading to strong anisotropic characteristics in their functionalities. Prior to the discussions of anisotropic behavior exhibited in relaxor-PT single crystals, engineered domain configuration [139,143,145,151,176,180,181], which is a very important concept for ferroelectric crystals, will be introduced first. A domain engineered ferroelectric crystal is one which has been poled by the application of a sufficiently large field along one of the possible polar axes of the crystal other than the zero-field polar axis, creating a set of domains in which the polarization vectors are oriented so that their angles to the poling direction are minimized [331]. In R , O and T phases, different engineered domain configurations and single domain states with different macroscopic symmetries can be achieved by poling along specific crystallographic directions, as listed in Table III.

Fig. 4 shows a Relaxor-PT single crystal boule grown by the Bridgman method, which can be separated into three different composition phases, including R phase, O/M (monoclinic) phase and T phase along the growth direction, due to the large segregation coefficient of Ti^{4+} [153,187,207]. It was observed that the crystals exhibit $4mm$ macroscopic symmetry when the crystals were poled along [001] directions, with engineered domain configurations $4R$ and $4O$ in R and O phase crystals respectively, while single domain state $1T$ is presented in T phase crystals. Meanwhile, the crystals are in $mm2$ and $3m$ symmetries when poled along [011] and [111] directions, corresponding to engineered domain configurations $2R$, $2T$ and $3O$, $3T$ respectively, with single domain states $1O$ and $1R$ obtained in O and R crystals owing to their spontaneous polarization directions being along [011] and [111]. In the notations, the numbers '1', '2' and '4' mean that there are one, two and four degenerate polarization directions in the poled crystals. The letters ' T ', ' R ' and ' O ' indicate the crystals are in tetragonal, rhombohedral and orthorhombic ferroelectric phases, respectively.

2.3.1.1 Anisotropy in rhombohedral relaxor-PT crystals: About fifty percent of the as-grown PMN-PT crystal boule is in rhombohedral phase, being in $4R$, $2R$ and $1R$ domain configurations when poled along its crystallographic directions [001], [011] and [111] respectively. The high longitudinal piezoelectric coefficients d_{33} are obtained in [001] and [011] poled rhombohedral crystals [305], while thickness shear piezoelectric coefficients d_{15} exhibit superior values in [011] and [111] poled crystals [172,293,297,306].

Of particular significance is that the $2R$ domain configuration, which exists in the [011] poled rhombohedral crystals, exhibits high longitudinal, thickness shear and transverse piezoelectric activities simultaneously [282,300,302]. In $2R$ domain configuration, there are two independent thickness shear piezoelectric coefficients, d_{15} and d_{24} , and two transverse piezoelectric coefficients, d_{31} and d_{32} , where $d_{15} \gg d_{24}$ and $-d_{32} \gg d_{31}$, due to the fact that the contribution of the polarization rotation to the shear deformation S_4 and extensional deformation S_1 in 71° domains will negate one another [302]. Furthermore, a new face shear (contour shear) vibration mode with high piezoelectric coefficient d_{36} can also be achieved in rotated $2R$ crystals ($ZXt45^\circ$ cut) [332–333], leading to a unique feature of relaxor-PT crystals, which will be discussed in 2.3.1.4. In addition to the piezoelectric properties, mechanical quality factor Q_m also shows anisotropic behavior, where the longitudinal Q_{33} for $4R$ domain configuration is on the order of 100, while the value is above 1000 in single

domain state $1R$ due to the absence of domain wall. Of interest is that both high piezoelectric coefficient d_{33} and mechanical Q_{33} were observed in $2R$ engineered domain configuration due to the fact that only 71° domains remained after polarization [334–335], which will benefit the high power applications at resonance frequency.

In order to clearly demonstrate the anisotropic behavior in R crystals, the principal properties and anisotropic ratios are given in Table IV. It can be observed that single domain rhombohedral PMN-PT crystals possess high anisotropic ratio with ultra-high transverse dielectric, shear elastic and shear piezoelectric constants, contributing to the high longitudinal piezoelectric coefficient in engineered domain configurations. For comparison, the PMN-PT ceramic counterpart was found to possess much lower anisotropic characteristics.

2.3.1.2 Anisotropy in tetragonal and orthorhombic relaxor-PT crystals: In contrast to rhombohedral crystals with $1R$ single domain state, the [001] poled tetragonal crystals show higher coercive field and higher T_C , along with the absence of ferroelectric phase transition T_{RT}/T_{OT} above room temperature and high mechanical Q_{33} , making them potentially useful for high power transducer applications [293,336]. Table V lists the principal properties and the anisotropic ratios for PIN-PMN-PT with single domain states $1O$ and $1T$. Similar to $1R$ single domain state, large property anisotropic ratios were observed, with very high transverse dielectric and shear piezoelectric constants, leading to high longitudinal piezoelectric properties in engineered domain configurations.

For tetragonal crystals with engineered domain configurations $2T$ and $3T$, on the other hand, high domain wall density can be achieved when the special poling procedure is employed, so-called domain size/wall engineering, leading to high dielectric constant of $>10,000$ and electromechanical coupling of $0.75\sim 0.78$, essential for the electrical impedance matching in high frequency 2D array medical imaging transducers [337–338].

Of particular importance in orthorhombic $1O$ crystals is the piezoelectric coefficient d_{24} , with high temperature stability and values of ~ 2000 pC/N due to the vertical R - O phase boundary in the phase diagram [339–340]. Correspondingly, in engineered domain configuration $3O$, the longitudinal coefficient d_{33} is on the order of >800 pC/N with minimal temperature variation ($<6\%$) due to the fact that the value of d_{33} in $3O$ configuration is mainly contributed by the large d_{24} value in $1O$ single domain state, taking advantage of the anisotropic piezoelectric properties [139]. This will be discussed in detail in section 3.3.3.1.

2.3.1.3 Orientation dependence of piezoelectric coefficients: In relaxor-PT crystals, the maximum longitudinal and transverse piezoelectric coefficients do not exist in single domain crystals based on their standard coordinates. As shown in Fig. 5, the highest longitudinal coefficient d_{33}^* was observed in the coordinate system with the Z' axis rotated to the [001] direction, while the highest coefficient d_{32}^* was achieved in the coordinate system with Z' , Y' and X' axes along [110], [001] and [110] directions, respectively. Therefore, in practical applications, rhombohedral relaxor-PT crystals are poled along [001] ($4R$ domain configuration) and [011] directions ($2R$ domain configuration) to obtain optimum piezoelectric coefficient d_{33}^* and d_{32}^* , respectively. This phenomenon is due to

the high level of shear coefficient d_{15} in the single domain state ($d_{15} \gg d_{33}$) [178,180,206,292,297,327,328]. It should be noted that the data used in Fig. 5 is from the rhombohedral PIN-PMN-PT crystals with a composition away from the MPB [292]. The anisotropic properties of relaxor-PT crystals with MPB compositions are similar to Fig. 5, but with much higher d_{33}^* and d_{32}^* values being on the order of ~ 2000 pC/N [290,341].

2.3.1.4 Origin of the piezoelectric anisotropy: In order to further understand the piezoelectric anisotropy of relaxor-PT ferroelectric crystals [176,179,228,233,342], the dielectric permittivity, spontaneous polarization and electrostrictive coefficients, which contribute to the piezoelectricity of ferroelectric materials, were investigated as a function of orientations. Fig. 6 shows the orientation dependence of the piezoelectric coefficient, dielectric constant (relative dielectric permittivity), polarization and electrostrictive coefficient for tetragonal relaxor-PT crystals. The maximum d_{33}^* is achieved along the direction of 48° rotation from the [001] axis [293]. The anisotropy of piezoelectric activity is determined by the orientation dependences of polarization, dielectric constant and electrostrictive coefficient. The maximum polarization is along the polar direction of the single domain crystals and decreases to zero when the direction is perpendicular to the polar axis, as given in Fig. 6(a). For the dielectric constant, on the contrary, the anisotropic characteristic depends on various factors, e.g., temperature, composition, phase transition, etc. For ferroelectric materials, the maximum dielectric constant ϵ_{33}^* is generally along the directions perpendicular to the polar axis when the material is on the proximity of the ferroelectric-ferroelectric phase transition, as revealed in Fig. 6(b). Meanwhile, the maximum ϵ_{33}^* will be along the polar direction if the ferroelectric material approaches the ferroelectric-paraelectric phase transition [178,179,343]. The anisotropy of electrostrictive coefficient Q_{33}^* is dominated by the crystal structure. For all perovskite-type materials, the orientation dependence of electrostrictive coefficient Q_{33}^* is similar, as given in Fig. 6(c), where the maximum and minimum values are along the $\langle 100 \rangle$ and $\langle 111 \rangle$ directions, respectively [344,345]. It can be seen that the polarization and electrostrictive coefficient possess stable anisotropic properties in perovskite-ferroelectrics, while the anisotropy of the dielectric constant is very sensitive to the temperature, composition, stress, etc. Thus, differences in piezoelectric anisotropy among different perovskite-ferroelectrics are dominated by the dielectric anisotropy.

2.3.2 Intrinsic and Extrinsic Contributions—Another uniqueness of relaxor-PT crystals is that the intrinsic contribution (lattice deformation), which dominates their high longitudinal piezoelectric coefficients, are on the order of ~ 90 – 95 % due to the high stability of the engineered domain configurations [133]. As a comparison, the intrinsic contribution of their polycrystalline counterparts was reported to be only 50 – 75 %, revealing the domain wall extrinsic contribution in ceramics is >25 % [343]. The extrinsic contribution in the ferroelectric materials can be quantitatively evaluated by Rayleigh analysis and high electric field measurements [346–356]. Calculated from the Rayleigh analysis, the ratios of extrinsic contribution to the total piezoelectric response for PMN-PT crystals as a function of composition are given in Fig. 7(a), where the error bars were calculated from three samples for each composition [354]. The error bars were relatively high for compositions near the phase boundaries, demonstrating that the extrinsic contribution for the compositions on the

proximity of the MPBs was not stable when compared to that of the compositions far away from the MPB, where the extrinsic contribution ratios for PMN-0.31PT and PMN-0.35PT crystals were found to be on the order of 10 %. The ratio was 7 % for tetragonal PMN-0.37PT crystal, while it was less than 5 % for all other compositions [354]. A similar trend was also observed in PIN-PMN-PT crystals, as given in Fig. 7(b) [305], where the extrinsic contribution is generally less than 5 % for rhombohedral crystals, while the values go up to 12 % for compositions in proximity of the MPB. This phenomenon was also observed in other domain engineered configurations, such as [011] poled PIN-PMN-PT:Mn crystals with 2R domain configuration, where the extrinsic contribution is only on the order of < 2 % [357–358]. This is due to the fact that Mn dopants in the crystals behave as acceptors, inducing oxygen vacancies and forming defect dipoles, clamping the extrinsic domain wall motion [141,334].

2.3.3 Piezoelectric properties at cryogenic temperatures—As discussed above, the intrinsic contribution dominates the piezoelectricity in relaxor-PT crystals, making them suitable for cryogenic temperature applications [359–368] since the extrinsic domain wall motion is greatly affected by temperature [174,179,197,340,369–372]. For example, the piezoelectric coefficients were reported to be on the order of > 900 pC/N for PIN-PMN-PT crystals at 120 K, much higher than the room temperature piezoelectric activity of polycrystalline ceramics (~750 pC/N for PZT-5H) [363].

The temperature-dependent intrinsic and extrinsic contributions of PIN-PMN-PT crystals and PMN-PT ceramics are summarized in Fig. 8(a) [363]. As expected, both intrinsic and extrinsic contributions decreased with decreasing temperature for all compositions. Based on thermodynamic analysis, the shear piezoelectric response (d_{15}) of the rhombohedral/monoclinic single domain state will decrease as temperature moves away from the polymorphic phase transition temperature (PPT) [158,178]. The reduction of shear piezoelectric response corresponds to an effective “hardening” of the polarization rotation process [180], leading to the decrease of intrinsic piezoelectricity. For PMN-PT ceramics, not only intrinsic piezoelectricity, but also the extrinsic contribution α (α is an indicative parameter for extrinsic piezoelectric contribution) drastically decreased from 280 to 40 cm/kV as the temperature decreased from 300 to 120 K, attributed to the clamping of domain wall motion [369–370]. Fig. 8(b) shows the relative variation in piezoelectric response as a function of temperature for PIN-PMN-PT crystals and compared to PMN-PT ceramics. At 120 K, the piezoelectric response was found to decrease by 27 % and 40 % for PIN-PMN-PT crystals with R and MPB compositions, respectively. The PMN-PT ceramic exhibited the largest decrease: ~75 % of the original value.

Fig. 9(a) depicts the variation of the d_{33} coefficient and value of $K_{33}P_r$ versus temperature for PMN-28PT crystals. The two curves exhibit similar variation, in good agreement with the fact that, for piezoelectric material, d_{33} is proportional to $Q_{33}P_r\epsilon_r$ (ϵ_r : relative dielectric permittivity), where Q_{33} and P_r are electrostrictive coefficient and remnant polarization, respectively. Assuming that $Q_{33}P_r$ is almost temperature independent in the cryogenic temperature range, the d_{33} curve should present a similar trend with the dielectric behavior. By extrapolation of the curves, the d_{33} value at 0 K was estimated to be 150 pC/N, similar to that of PZT ceramics. Fig. 9(b) depicts the variation of the electromechanical coupling k_{33}

and elastic constant s_{33}^E . To discuss the cryogenic electromechanical properties, Fig. 9 can be divided into three temperature regions: region I (T=10–100 K), region II (T=100–250 K) and region III (T=250–300 K) [372]. In region II, the piezoelectric, dielectric, elastic and electromechanical coupling coefficients were found to exhibit high stability with respect to temperature when compared with regions I and III. In regions I and III, the piezoelectric, dielectric and elastic coefficients were found to drastically decrease with decreasing temperature, while the coupling factor only showed decreasing tendency in region I. In region III, the crystal deviates from the R-T phase transition point, leading to the decrease of d_{33} , ϵ_{33} and s_{33}^E , while in region I, the degradation of d_{33} , ϵ_{33} and s_{33}^E cannot be explained by the same mechanism. Based on the thermodynamic analysis, the tangent of d_{33} -T curves will decrease as the crystal deviates from the phase transition point, indicating that the variation of d_{33} will decrease with the crystal deviating from the phase transition point. However, the tangent of d_{33} -T curves in region I was found to be much higher than that in region III, so the large divergence of d_{33} in region I cannot be explained based on the thermodynamic theory of traditional ferroelectrics. In addition, no abnormal reduction of piezoelectric coefficients at cryogenic temperature was observed in PZT ceramics [369]. It was proposed that the decreased d_{33} was related to the influence of temperature on the compositional fluctuation-induced random electric fields, polarization and point defects, which give rise to combinatory pinning effects on the macro domain walls motions [372]. The drastic decrease of d_{33} , ϵ_{33} and s_{33}^E of relaxor-PT crystals in temperature region I was thought to be associated with the nature of the relaxor: disordered B-site cations and polar nanoregions. With decreasing temperature, the size of polar nanoregions will increase and PNRs will transform to ferroelectric state, thus the thermal fluctuations induced by polar nanoregions (in relaxor state) may die away, leading to a decrease of piezoelectric response [368]. It is worth noting that although the piezoelectric response decreases in both regions I and III, the electromechanical coupling factor only decrease in region I, demonstrating that the phonons associated with the nature of relaxor may dominate the level of electromechanical coupling factor.

2.3.4 The development of new shear vibration modes

2.3.4.1 Thickness shear vibration modes: Table VI summarizes the thickness shear properties for various crystals with different domain configurations and compares them to commercial PZT5 and PZT8 polycrystalline ceramics [374,375]. It is evident that high shear piezoelectric coefficients and elastic compliances can be easily achieved in crystals with single domain states, such as “1R” and “1O” [162,278,292], which will benefit the broad bandwidth transducer applications (high electromechanical coupling) at low operational frequency range (large elastic compliance). In addition, the high shear elastic compliance (low frequency constant) of single crystals results in small parts for the same frequency compared to polycrystalline ceramics, allowing miniaturization of the transducers or sensors [374].

However, issues exist for the usage of shear vibration modes, including temperature instability of dielectric and piezoelectric properties, low allowable drive field stability (due to the working direction, i.e. applied electric field, is normal to the poling direction in the

thickness shear mode) [375], low mechanical quality factor (which is very important for high power application) and cross-talk effect, etc. [141]. Although large shear properties have been observed in crystals with single domain state, the single domain crystal is subject to cracking from the large electric field induced strain/stress during the poling process [330]. Fig. 10 shows the strain versus electric field curves for rhombohedral PMN-PT crystals along [001] and [111] directions [42], where very high negative strain was observed in [111] poled crystals (this value is about -0.7% for [001] poled tetragonal crystals [330]). This is due to the fact that the non- 180° ferroelastic domains are not equivalent to [111] direction, as shown in Fig. 10(b), thus leading to a very large negative strain during ferroelastic domain switching. The electric field induced strain will lead to cracks during poling, which can be avoided in multi domain state, as shown in Fig. 10(c). The [111] spontaneous strains are equivalent to [001] direction, thus the very low negative strain in crystals with $4R$ engineered domain configuration is associated with the piezoelectric coefficient other than ferroelastic domain switching. Of particular interest is that large shear d_{15} and low frequent constant, being on the order of ~ 2800 pC/N and 570 Hz·m respectively, were also obtained in engineered domain configuration “ $2R$ ”, with the advantage of no-cracking during the poling process [302], as listed in Table VI.

2.3.4.2 Face (contour) shear vibration mode: Though thickness shear exhibits ultrahigh piezoelectric coefficients, coupling factors and elastic compliances, the low field stability inherently associated with the 90° polarization rotation angle (the working direction is normal to the poling direction) will restrict their applications at high drive field condition (will be discussed in section 3.3.3.2) [141,374]. Recently, it was reported that [011] poled rhombohedral crystals possessed high face shear properties when the sample was rotated along poling direction of about 45° . That is, $Z_{t\pm 45^\circ}$ cut samples, which incorporate two extensional lateral modes [332–335], exhibit promising properties different from their thickness shear counterparts. Ultralow frequency transducers were projected based on the face shear (or d_{36}) mode in PMN-PT crystals due to their ultralow frequency constant and high piezoelectric coefficients [376,377]. In addition, due to the uniqueness of the face shear vibration in combination with high coupling and high mechanical Q_{36} , face shear crystals have been studied for tactile sensing and ultrasound motor applications [378–382]. In contrast to conventional thickness shear d_{15} , the face shear vibration mode can be repolarized; i.e., the poling electrode is the same as the active electrode [141,340,374]. The *ac* driving field level and mechanical quality factor Q_{36} of the face shear mode were reported to be significantly higher compared to thickness shear vibration modes, owing to the fact that the applied electric field in face shear vibration is along polarization direction [141,374].

The principal properties related to the face shear vibration mode for relaxor-PT crystals are reported in Table VII and compared to conventional thickness shear properties [300,333,383]. The dielectric constant for the studied crystals was found to be in the range from 4500 to 5200, while the dielectric loss was in the range of 0.1–0.2%. The elastic compliance s_{66}^E and piezoelectric coefficient d_{36} were found to be on the order of 160–200 pm^2/N and 2000–2500 pC/N respectively, with electromechanical coupling factor k_{36} being 0.80–0.83. It should be noted that the property variations observed in all shear vibration

modes are closely related to the crystal composition, following the general trend of relaxor-PT crystals [318]. The value of ~ 500 Hz·m for the ultra-low face shear frequency constant N_{36} was obtained, which is similar to the values of thickness shear modes, ~ 350 – 600 Hz·m [333]. Fig. 11 shows the comparison of the piezoelectric deformation of thickness shear and face shear vibrations. For the case of face shear mode, the frequency constant refers to the large dimension (length) of the samples, allowing for design of ultralow frequency and broad bandwidth transducers with minimized dimension [374,383]. In addition, it is important to note that the mechanical quality factor Q_{36} obtained for the face shear crystals are on the order of 150–180 (higher $Q_{36} > 350$ was observed for 3rd generation relaxor-PT crystals), significantly higher than those of the thickness shear modes, ~ 20 – 30 . The low mechanical Q_{15} is believed to relate to the ease of polarization rotation in corresponding thickness shear cuts, while the enhanced Q_{36} in face shear is due to the polarization rotation angle of 35.5° in [011] poled rhombohedral crystals [141,357]. Meanwhile, the field stability ratio of the face shear vibration mode, on the order of 100% of its respective coercive field, greatly expands the usage range for high power application, which is due to the fact that the working direction is along the poling direction in face shear vibration [335]. Above the coercive field, the crystals will be depolarized due to the micro cracks induced by the large anisotropy of the transverse strains [298].

Other uniqueness of the relaxor-PT single crystals include high coupling and low mechanical loss, leading to high figure of merit (FOM) of k^2Q_m for high power transducer applications [318], and simultaneous high piezoelectric and low strain hysteresis for high precision actuator applications [139]. These will be discussed in the following section III.

III. Figure of merits (FOM) of piezoelectric materials for various electroacoustic applications

A figure of merit is a number employed to characterize the performance or efficiency/effectiveness of a device or material, albeit the definition of FOM is difficult. It is extremely valuable to the device design process because it compels the designer to think critically about what parameters are the most meaningful to a successful design outcome.

3.1 Medical Diagnostic Ultrasound

3.1.1 Piezoelectric materials for ultrasound imaging (diagnostic)—There are many different medical imaging modalities, such as radiography, magnetic resonance imaging (MRI), computed tomography (CT), elastography, photoacoustic imaging, and ultrasound, to name a few. Among these, medical ultrasound uses high frequency broadband transducers, with advantages of real time monitoring of moving structures and no ionizing radiation, etc. [384]. Ultrasonic transducers convert electrical energy into mechanical form when generating an acoustic wave (transmitter) and convert mechanical energy into an electrical signal when detecting the echo (receiver) [2]. In general, broadband transducers should be used for medical ultrasonic imaging. The broad bandwidth response corresponds to a short pulse length, resulting in a better axial resolution which is dominated by the high electromechanical coupling factor, acoustic impedance and electrical impedance matching [385]. Fig. 12 gives a schematic view of the obstetric ultrasound imaging for a developing

fetus, with a three-port network ultrasonic imaging transducer and the operational mechanism. The transducer consists of two mechanical components including the matching and backing layers, and one electrical component, the piezoelectric element, which is the heart of the transducer. It can be seen from the figure that both transmission efficiency and reception sensitivity parameters (TP and RP , respectively) are closely associated with the thickness electromechanical coupling k_t , clamped dielectric constant ϵ_{33}^s and elastic stiffness c_{33}^D of the piezoelectric element [385]. Meanwhile, the bandwidth (e.g. -6dB fractional bandwidth) is also related to the coupling factor, where broad bandwidth can be achieved in materials possessing high coupling factor. Since the acoustic impedance of the piezoelectric materials is about $\sim 30\text{--}37$ MRayl, much higher than those of water or human tissues ($\sim 1.5\text{--}5$ MRayl), a substantial part of the emitted acoustic energy will be lost, leading to a poor resolution and sensitivity. Thus single or multi matching layer(s) with lower acoustic impedance(s) are required to further improve the front acoustic matching of the transducer. The backing material is added to the rear of the transducer in order to damp the acoustic backwave and to reduce the pulse duration [385]. In addition, the electrical impedance of the transducer needs to be matched to the resistance of the coaxial cable and electrical circuit, which is generally 50 Ohm. The electrical impedance is inversely associated with the capacitance of the transducer, thus determined by the clamped dielectric constant and dimension of the piezoelectric element [24].

Based on the above discussion, the figure of merit (FOM) of the piezoelectric element for imaging transducers is the electromechanical coupling, which accounts for the high resolution, high power efficiency and broad bandwidth [385]. The thickness coupling factor for piezoelectric materials, including the relaxor-PT single crystals and PZT ceramics, is generally on the order of 0.5–0.6 [70–71]. In order to take advantage of the ultrahigh longitudinal coupling of relaxor-PT crystals, 1–3 and 2–2 crystal/epoxy composites have been extensively studied and commercialized in various transducer applications [11–20, 386–387]. Fig. 13 gives the geometries of monolithic samples, 2–2 and 1–3 composites, with their corresponding coupling factors, which are thickness mode, sliver mode and longitudinal mode, respectively. The coupling factors of longitudinal k_{33} and sliver k_{33}' modes are found to be >0.9 and ~ 0.8 respectively, both much higher than that of thickness mode $k_t \sim 0.6$, greatly benefitting transducer applications [374,388]. Furthermore, the composites are found to possess the advantage of lower acoustic impedance associated with the passive epoxy phase, about 12–20 MRayl, much smaller than those of single crystals ($\sim 30\text{--}37$ MRayl), thus improving acoustic matching of transducers to the human body [2,385]. Table VIII lists the principal properties of relaxor-PT single crystals as compared to the state-of-the-art PZT-5H polycrystalline ceramics. The relaxor-PT crystals are found to exhibit higher electromechanical coupling factors, higher piezoelectric coefficients and higher elastic compliance when compared to PZT5H ceramics, which will benefit greater bandwidth, higher sensitivity and reduced device dimension for ultrasound transducer applications. Meanwhile, the lower dielectric loss will suppress internal heat generation, thus reducing the operating temperature rise. It should be noted that the clamped dielectric constants of relaxor-PT crystals are lower than those of ceramics, albeit their high free dielectric constants, this will impair the electrical impedance matching for array transducer

applications. In addition, the lower coercive field of crystals will deteriorate the drive stability.

3.1.2 High frequency ultrasonic imaging and the challenges of piezoelectric crystals

The medical community has increasingly looked to other ultrasonic capabilities for the potential insights that can be given to biomedical systems through improving current diagnostic ultrasonic frequency ranges, e.g. the 2–10 MHz range, and in some cases up to about 20 MHz [2]. High-frequency imaging beyond 30 MHz was reviewed by Lockwood et al. [389], including the ophthalmic ultrasound at 60 MHz, intravascular and intra-articular imaging up to 60MHz, skin imaging at 100 MHz, and some early works at 40–60 MHz investigating mouse embryonic development. Other studies used the acoustic microscope as a tool to determine tissue properties, such as those in fresh tissue at 100 MHz, which were measured by Scherba et al. [390]. Fig. 14 lists transducer operational frequencies and the corresponding imaging human tissues, with the frequency ranges from 2.5 MHz to 100 MHz [2]. Generally, higher operational frequency gives rise to higher resolution (smaller wavelength), but with less penetration. For a piezoelectric transducer, the frequency is closely related to the elastic constant (sound velocity or frequency constant) and the thickness of the piezoelectric materials, where a smaller thickness usually corresponds to a higher frequency for the same material [391–392]. Lithium niobate single crystals have been studied for high frequency transducer applications by employing 36° rotated Y-cut sample with coupling factor k_t of 0.48, clamped dielectric constant of ~40 and high elastic stiffness (high sound velocity of 7340 m/s), which makes the high frequency piezoelectric element easier [87–88, 393]. However, the coupling factor is far inferior to that of relaxor-PT crystals.

As given in Fig. 14, it should be noted that the capacitance of the piezoelectric element is inversely proportional to its thickness; in order to match the electrical impedance, it is desirable to use low dielectric constant monolithic crystals for high frequency applications. It was reported that the tetragonal monolithic PMN-PT single crystals, with coupling factors k_t of 0.6 and clamped dielectric constant of ~200–300, showed promising properties for single element transducers with operational frequency range of >40 MHz [394–395]. As discussed in section 3.1.1, the FOM for medical imaging is the coupling factor. Thus, in order to further increase the electromechanical coupling factor, 1–3 crystal/epoxy composites have been actively studied, taking advantage of the high longitudinal coupling k_{33} of relaxor-PT crystals (as shown in Fig. 13). Traditionally, the dice-and-fill method is employed to develop low- frequency (<10 MHz) 1–3 composite transducers. However, due to the physical limitation of blade and brittleness of the active materials, the traditional method cannot be used to develop high- frequency (>30 MHz) composite transducers [90–93]. With the increasing demand of high-frequency ultrasonic applications, etch-and-fill technique and facile method have been developed recently [396–397]. Using the ICP (Inductively Coupled Plasma) -RIE (Reactive Ion Etching) dry etching technique, PMN-PT single crystals can be etched to a periodic pillar pattern with a sidewall angle of >85° [398–404]. However, recent experimental data for PMNT crystal/epoxy 1–3 composites (piezoelectric composite- micromachined ultrasound transducer PC-MUT) operating at high frequencies >20 MHz exhibited a relatively large decrease in electromechanical coupling,

with values being less than 0.75, showing a strong scaling effect and leading to the question of the origin of property degradation at high frequencies [141,374,405–406].

Fig. 15 shows the electromechanical properties of relaxor-PT crystal/epoxy 1–3 composites as a function of sample thickness. For comparison, the longitudinal coupling factors (k_{33}) of

the monolithic relaxor-PT crystals were calculated by the equation $k_{33} = \sqrt{1 - \left(\frac{\epsilon_{33}^S}{\epsilon_{33}^T} \right)}$ and plotted as a function of sample thickness. Note that the corresponding resonance frequencies on the top X-axis of Fig. 15 were calculated from the frequency constants by assuming ~ 1000 Hz·m for both monolithic and 1–3 composites samples. As shown in Fig. 15, the monolithic PMN-PT crystals were found to exhibit a decrease trend in coupling (k_{33}) with decreasing the thickness of crystal, due to the degradation of the free dielectric constant [405–406]. The 20 MHz PIN-PMN-PT/epoxy 1–3 composites were found to maintain higher electromechanical coupling factors on the order of 0.80, compared to 20 MHz PMN-PT composites with coupling of only 0.74. It should be noted that all 1–3 composites have the same volume fraction and ratio of post height to width. The observed scaling effect is reported to be associated with the ferroelectric domain size, where the large domains will be clamped by the surface boundary when the physical size of samples becomes of the same order as the domain size, inhibiting the domain wall motion and restricting the polarization rotation. This can be confirmed by the domain observations, where the domain size of PMN-PT crystals was found to be on the order of 10–20 μm , while it is only about 1 μm for PIN-PMN-PT crystals, showing the advantage of the ternary system [405–406]. Similar phenomena were also reported for BT and KT single crystals, where fine domain size accounted for the enhanced piezoelectric properties [407–409]. Furthermore, in polycrystalline PMN-PT ceramics, the fine grain ceramics were found to possess improved properties [121] and scaling effect when compared to their coarse grain size counterparts, due to their smaller domain size (domain size is proportional to $\sqrt{\text{grain size}}$) [410–412]. Admittedly, the surface damage layer induced by the dicing process and the stiffness of the epoxy filler also contribute to the coupling degradation; these can be alleviated by RIE dry etching and employing soft epoxy.

In order to confirm the role of domain size on the piezoelectric properties in ultrathin samples, a field-cool poling approach was applied to PMN-PT crystals with 100 μm thicknesses, where significantly smaller domain sizes on the order of ~ 5 μm were achieved [198]. Consequently, the piezoelectric coefficient was greatly improved from 1300 pm/V (coarse domain sample ~ 20 μm) to 2200 pm/V, as shown in Fig. 16(a), due to the fact that the domain size of field-cool poled crystals is much smaller than the thickness of the samples, leading to less impact on the polarization rotation and domain wall motion from the boundary clamping [198]. The stability of the engineered domain wall was further investigated by domain observation and strain behavior measurement as a function of pulse-field and number of cycles on the thin PMN-PT crystals. With increasing the pulse electric field magnitude and cycling number, the piezoelectric coefficients were found to decrease from 2000 pm/V to 1300 pm/V, as given in Fig. 16 (b), corresponding to the enlarged domain size from 5 μm to 30 μm ($\sim 3E_C$) after 1.5×10^6 pulses, demonstrating the inferior field stability of the finer domains [198].

3.2 Therapeutic and Surgical Ultrasound

3.2.1 Piezoelectric materials for therapeutic ultrasound and surgical

applications—Low intensity ultrasound, which leads to minimal biological effects and no tissue damage, is typically used for medical diagnostic imaging. As acoustic intensity increase, other effects can also occur, specifically heating and cavitation. Therefore, ultrasound can be used as a therapeutic agent that can deliver heat and also cause non-thermal cell stimulating effects [413]. As the power increases, there is a continuum of interaction which changes from “therapy,” where there are beneficial effects on tissue, to “surgery” in which tissue is destroyed. The transition to surgery from therapy occurs simply through either increased duration of treatment or increase in the power used. The various destructive interactions can be considered in several categories [2, 413–419], including (1) high intensity focused ultrasound (HIFU), which uses a heating mechanism; (2) lithotripsy/histotripsy, which uses focused shock waves to break up hard/soft subjects, such as kidney stones or tumor tissue; and (3) a number of other high power-low frequency interactions, all using a horn or tip in contact with tissue to cause disruption. Fig. 17 gives the operational mechanisms for HIFU (a), histotripsy and its related usage for drug delivery (b). It can be seen that the acoustic pressure generated by HIFU creates tissue movement (dilatation and contraction) whose amplitude is directly related to the pressure level, as the tissue response is not perfectly elastic. Thus energy is lost and converted into heat, exceeding a threshold thermal dose equivalent to 56 °C for 1 s, producing tissue coagulative necrosis and cell death [2]. The operational frequency range for HIFU is generally in the range of 0.8 ~2 MHz with acoustic pressure up to 70 MPa. On the contrary, the mechanism of histotripsy is controlled acoustic cavitation, where the ultrasound pressure changes (compressive and rarefactive pressures) induced microbubbles in the human body. The formation, oscillation and collapse of microbubbles create localized stresses and pressures at the cellular and subcellular level resulting in cellular destruction [1–5,9,392–394,414–418].

The use of ultrasound to promote drug delivery was first reported by Fellingner and Schmid, who developed a successful treatment for polyarthritis by using ultrasound to drive hydrocortisone ointment into the inflamed tissues [420]. The technique of driving drug molecules across the percutaneous barrier to the target area using ultrasonic perturbation is termed “sonophoresis” or “phonophoresis” [421]. Since then, a wide variety of drug/ultrasound combinations have been implemented for sonophoresis. Most recently, ultrasound application has been used to promote delivery of high molecular weight proteins through intact skin. In addition to sonophoresis research, ultrasound has been shown to enhance the effects of several therapeutic drug classes, including chemotherapeutic, thrombolytic, and gene-based drugs, where the drugs are only released at the site of the tumor, while the patient’s total body exposure to the drugs would be limited. This, for certain types of cancer, could help reduce the unpleasant side effects of the chemotherapy [415,422]. Furthermore, ultrasound contrast agents, which were originally developed for diagnostic ultrasound, have been shown to augment the delivery and effectiveness of certain drugs. These ultrasound contrast agents can also be used as drug carriers for responsive and targeted drug delivery in the presence of ultrasound insonation. Meanwhile, the presence of microbubbles will enormously enhance delivery of genetic material, proteins and smaller chemical agents/drugs [416]. The operational frequency for lithotripsy/histotripsy is

relatively low, being in the range of 0.25~0.5 MHz, with intensity up to 30 MPa, frequency range up to 2 MHz for drug delivery application, and acoustic pressure of 0.2~8 MPa [423].

The Langevin type transducer is generally accepted for medical surgical applications, such as Harmonic scalpel which is cutting instrument used during surgical procedures to simultaneously cut and coagulate tissue, and ultrasonic surgical handpieces for neurosurgery and orthopedic surgery, etc. All these surgery ultrasounds are operated at low frequency range and resonance mode, with a “horn” type of displacement amplification mechanism. Fig. 18 shows this type medical surgical ultrasound device, such as ultrasonic scissors and scalpel, and the original steel portion of the Langevin transducer can be modified with a “horn” concept to increase the displacement amplitude. By tapering the metal tip portion, the displacement level can be significantly amplified, which can be used for ultrasonic cutters and cavitation [419]. For these applications, in order to achieve high intensity, the ultrasound transducer is driven by tone bursts at resonance frequency with low duty cycle (~20 %).

3.2.2 Advantages and Challenges of Relaxor-PT Crystals—From a material viewpoint, the medical therapy and surgery require operation at resonance frequency; thus, a high mechanical quality factor Q_m is preferable because of the high-power output without heat generation. Meanwhile, other properties, such as high electromechanical coupling factor (relates to the bandwidth and efficiency/sensitivity of the transducer) and high piezoelectric coefficient (relates to the output acoustic power), are desirable for therapeutic/surgical applications. It is also notable that the actual mechanical vibration amplitude at the resonance frequency is directly proportional to Q_m value (i.e., displacement amplification factor), while the power dissipation (heat generation) from the piezoelectric elements in ultrasonic transducer operated at resonance frequency is inversely proportional to the mechanical Q_m [3,10,296,388]. Thus, the FOM of materials for high power therapeutic/surgical applications is the product of dQ_m and/or k_2Q_m [424]. In ferroelectrics, the Q_m is mainly affected by the existence of domain wall motion and polarization rotation, where the polarization rotation angle was found to play an important role in the determination of Q_m value in relaxor-PT crystals because of the inherent anisotropic characteristics [141,334,346]. Table IX gives the loss and quality factors for relaxor-PT crystals as a function of polarization rotation angle. With increasing the polarization rotation angle from 0 to 90°, the piezoelectric coefficients were found to greatly increase with mechanical quality factors going down (or losses increase), resulting in the high piezoelectric d and loss for thickness shear vibration mode and low piezoelectric d and loss for longitudinal vibration mode in single domain states [141,334]. Of particular significance is that the [011] poled relaxor-PT crystals with 2R engineered domain configuration exhibit high piezoelectric coefficients, yet possess low mechanical loss due to the smaller polarization rotation angle on the order of 35.5° [334]. Table X lists the principal properties of 2nd generation and 3rd generation relaxor-PT crystals along various crystallographic directions, compared to state-of-the-art “hard” PZT8 polycrystalline ceramics. It can be observed that single crystals exhibit ultrahigh piezoelectric and electromechanical couplings, leading to high FOM when compared to PZT8 ceramics. Of particular interest is that [011] poled PIN-PMN-PT:Mn crystals were found to possess $d \cdot Q_m$ of five times that of PZT8 ceramics.

Furthermore, the high elastic compliance (three times higher than that of PZT8) allows lower operational frequency or smaller device dimensions when compared to PZT8. It should be noted that single crystals exhibit low phase transition temperature and low coercive field (and internal bias), which will deteriorate the thermal stability (temperature usage range) and field stability (power limitation). These are the issues need to be addressed.

For polycrystalline ceramics, a consequence of high Q_m is the sacrifice of electromechanical couplings. As shown in Fig. 19, the coupling k_{33} is found to decrease with increasing mechanical Q_m values. Thus, both high Q_m and high coupling cannot be simultaneously achieved in polycrystalline ceramics [425]. Of particular significance is that for domain engineered relaxor-PT crystal systems, in contrast to ceramics, the mechanical Q_m values can be improved without sacrificing the electromechanical coupling [318]. As shown in Fig. 19, the modified crystal systems exhibit different levels of Q_m , in the range of 70–2000, while maintaining ultrahigh electromechanical coupling on the order of >0.85 , demonstrating the 3rd generation relaxor-PT crystals to be unique piezoelectrics and potential materials for high power electromechanical applications [273,296,304,336, 357,358,426,427].

3.3 Underwater acoustics

As underwater acoustic technology matured it began to have significant commercial applications such as depth sounding to provide detailed ocean bottom mapping [3]. Bottom mapping techniques can be readily extended to the exploration of the underwater oil/gas or mineral mining, underwater cable or pipeline inspections and oceanographic research. In addition, it also has commercial importance in the fishing industry where transducers have been developed specifically for locating schools of fish [1–3]. The underwater acoustic transducer can be categorized into active and passive types, where active transducer uses a sound transmitter and a receiver, while passive transducer listens without transmitting.

3.3.1 Piezoelectric materials for underwater active transducer applications—

Fig. 20 shows the sketch for underwater electroacoustic transducers used to locate a large school of fish. In addition to the FOM of materials for high power transducer applications, other factors also need to be considered for underwater acoustic transducers. For example, it is desirable that the underwater transducers operate at the low frequency range with miniaturized dimensions, high drive fields and high duty cycles [6–7]. Furthermore, as with other electroacoustic transducers, a prestress is required for the underwater transducer package, thus affecting the piezoelectric behavior.

The FOM of the piezoelectric materials for underwater acoustic applications is dQ_m relating to the acoustic velocity and/or k_2Q_m being associated with the electroacoustic efficiency [388]. In addition, it can be observed from the acoustic efficiency equation that dielectric loss also plays an important role for the performance of underwater transducers [3]. However, due to the nonlinear characteristics of ferroelectrics, such as domain wall motion and phase transition, the measured losses strongly depend on the amplitude of the drive field [10,200,216,296,428–433], which is closely related to the practical transducer applications. These measured values are referred to as large signal losses, to be separated from the small

signal losses (measured at $V_{rms} = 1V$). Fig. 21 shows the mechanical loss and dielectric loss as a function of drive field. The longitudinal mechanical loss was measured at driving resonance frequency for different crystal systems and phases, as given in Fig. 21 (a). All the mechanical losses were found to increase with increasing the drive field, and were saturated when the fields were above 0.15 kV/cm [141,296]. Of particular interest is that the saturated loss for [001] poled tetragonal PIN-PMN-PT crystals was found to be much lower than those of rhombohedral crystals, due to the absence of domain wall (single domain state), while the ternary crystals were found to possess lower loss when compared to their binary counterparts, being related to the higher Curie temperature and coercive field [336]. The dielectric loss was measured as a function of drive field at 1 kHz frequency, as shown in Fig. 21 (b), exhibiting similar trend for different crystal systems [429]. The compositions far away from MPB show lower dielectric loss, while the acceptor doped PIN-PMN-PT crystals possess much lower loss when compared to the undoped counterparts, due to the stabilization of the domain wall motion by internal bias [429].

Transducers operating at low frequency with high output power require large displacement of the radiating surfaces [10]. Some geometries of underwater transducers are given in Fig. 22. As first demonstrated by Langevin, the addition of end (tail) mass to a piezoelectric stack lowers the resonance frequency of the tonpilz, allowing for low frequency operations without requiring prohibitive stack lengths [3,6,10]. An electric field is generally applied along the polarization of the piezoelectric stack via the sandwiched electrodes, resulting in a 33-mode operation. Actuation from the piezoelectric stack causes the head mass to radiate acoustic energy into the surrounding water, while the tail mass is not in contact with the surrounding water. The head and tail masses offer additional parameters to the stack length when determining the fundamental resonance frequency, and this design can be scaled from 1–100 kHz frequency [10]. The presence of the stress bolt and compressive stress bias reduces the dependence on high quality surface preparation of the piezoelectric elements [10]. It can be observed that different piezoelectric vibrations can be employed in the underwater acoustic transducers, including the above mentioned longitudinal 33 mode, which gives the high electromechanical coupling of >0.9 and piezoelectric coefficient of >1500 pC/N. The transverse vibration 32 mode can be used to generate large displacement taking advantage of the length dimension, with electromechanical coupling of ~ 0.9 and piezoelectric coefficient of -1500 pC/N, which was reported to allow lower drive and bias voltages while simplifying the construction with minimal impact on transducer effective coupling, size and bandwidth [321,434–438]. More recently, single crystals with shear vibration modes drew attentions for low frequency acoustic transducer applications, due to the ultrahigh elastic compliance, piezoelectric coefficient and coupling factor. The schematics of the designed transducers using thickness shear and face shear vibrations are presented in Fig. 22 (b), where the parallelepiped shaped piezoelectric elements disposed between and attached to the tail mass and the head mass through the elongated shaft extending from the head and within the cavity of the tail mass [376]. In this way, the piezoelectric deformation of the shear vibration modes (including the thickness shear and face shear) will generate large displacement of the head mass at low frequency range.

All these designs will allow the low driving electric field to have large displacements, closely associated with the piezoelectric coefficients, the displacement amplification factor (Q_m) and the dimension of the piezoelectric elements. Table XI lists the principal properties of the shear vibrations modes and compared to longitudinal and transverse vibration modes. The thickness shear vibration mode was found to exhibit ultrahigh piezoelectric and electromechanical properties, but with very low mechanical quality factor, due to the fact that the polarization rotation angle is 90° in thickness shear, thus giving rise to high dielectric, piezoelectric and loss. Of particular significance is that the high elastic compliance leads to very low frequency constants, benefit the low operating frequency or miniaturization of the devices, which will be discussed in section 3.3.3.

3.3.2 Piezoelectric materials for passive sensor (hydrophone) applications—

Hydrophones are one important category of piezoelectric sensors, which detect the acoustic pressure signals and noise in water while producing an output voltage proportional to pressure [3,17,440]. Fig. 23 gives schematic of the hydrophone operational mechanism. Acoustic pressure is considered to be effectively hydrostatic as the wavelengths of sounds in low frequency range are much larger than the sensor dimensions [3]. The voltage produced under hydrostatic pressure is used to measure the sensitivity of a hydrophone. In this regard, a useful parameter to evaluate piezoelectric materials for use in hydrophones is the voltage coefficient g_h , which relates output voltage to the hydrostatic stress. Another parameter is the hydrostatic charge coefficient d_h , which describes polarization resulting from a change in stress, with $d_h = d_{33} + d_{31} + d_{32}$ (for poled polycrystalline ceramics, $d_{31} = d_{32}$). A useful figure of merit (FOM) for hydrophone materials is the product of the voltage and charge coefficients, $d_h \times g_h$ [3,102,342,441]. A basic limitation on hydrophone performance is the electrical noise generated internally, which must not exceed the total sea noise, including the noise from ships, fish, waves, etc., as shown in Fig. 23 [3]. At far below the resonance frequency, the energy dissipation is mainly dominated by the dielectric loss. Thus the alternative FOM has been proposed to take into account the dielectric loss of the sensors, which is given by $(d_h \times g_h / \tan \delta)$ [3,442–443]. Other desirable properties for hydrophone sensors include, but are not limited to, low density for good acoustic impedance matching with water; and minimal variation of d_h and g_h with pressure, temperature, and/or frequency [17,444–445].

PZT ceramics and relaxor-PT single crystals have been widely used for medical transducer applications; however, they have limited utility in transducers under hydrostatic conditions because of their relatively low hydrostatic piezoelectric coefficients, due to d_{33} about twice the magnitude and opposite in sign from d_{31} , thus leading to a relatively low d_h which is generally on the order of 40–70 pC/N for perovskite ferroelectric ceramics [342]. In addition, the high permittivity results in low g_h coefficients. There has been a longtime interest in developing piezoelectric composites for underwater hydrophone applications because of their high hydrostatic sensitivity, good acoustic impedance matching to water, and high-pressure tolerance [15,92–93,97–102,107–110]. Piezocomposite hydrophones are dominated by 1–3 type connectivity in which the arrangement of piezoelectric material and polymer will reduce the influence of the 31 and 32 transverse extensional modes and produce a significant improvement in hydrostatic voltage sensitivity, with a high FOM.

Other engineered connectivities, such as parallel-connected 2-2 composites, which are stacks of piezoelectric ceramic sheets separated by passive polymer layers, have also been investigated [97–99,101,105]. Recently, 2-2 lamellar composites consisted of relaxor-PT single crystals have been theoretically studied, giving a promising FOM of $16 \text{ pm}^2/\text{N}$ for a crystal volume of 25 % [107–109]. The 2-2 composite takes advantage of the strong anisotropic behavior of $[011]_{\text{C}}$ poled single crystals, with macroscopic $mm2$ symmetry, in which the d_{33} and d_{31} are both positive while d_{32} is negative. The contribution of d_{32} to the hydrostatic d_{h} value is greatly reduced when the polymer layers are perpendicular to the 2 direction (Y axis, as shown in Fig. 24, where the $[011]_{\text{C}}$ direction is along Z axis, and $[01\bar{1}]_{\text{C}}$ $[100]_{\text{C}}$ are the X and Y axes, respectively), with minimal reduction of the d_{33} and d_{31} values. Thus, the hydrostatic piezoelectric d_{h} is significantly improved [99,141]. In addition, the dielectric constant of 2-2 composite is much lower than that of the crystal phase due to the ultralow dielectric of the passive epoxy phase, leading to a higher piezoelectric voltage coefficient g_{h} .

Table XII gives comparison of the hydrostatic properties for various piezoelectric materials, including polymer, ceramics, crystals and composites. The lead metaniobate was found to possess high FOM value, but with relatively low dielectric constant [72]. Of particular interest is that the 2-2 crystal/epoxy composites comprised of $[011]$ poled relaxor-PT crystals, with the lamellar direction parallel to X axes, show increased hydrostatic properties, due to the fact that the large negative d_{32} coefficients are greatly eliminated in this structure [99]. The hydrostatic properties of the 2-2 composites were found to be significantly enhanced by adding stiff faceplate, decreasing the Young's modulus and Poisson's ratio of the epoxy matrix. The highest FOM value, being on the order of $92 \text{ pm}^2/\text{N}$, was achieved in O-soft+bubbles 2-2 composites (where O means orthorhombic crystal, soft means epoxy with low Young's modulus and bubbles means micro bubbles being added in the epoxy to further decrease the Poisson's ratio of the epoxy), with a_1/d_{h} (normalized pressure coefficient of the hydrostatic piezoelectric variation) being on the order of $0.031 \text{ ppm}/\text{Pa}$, while R-soft+bubbles 2-2 composite was found to possess FOM value of $11 \text{ pm}^2/\text{N}$, with much higher pressure stability [99]. The hydrostatic piezoelectric properties, together with further optimizing the structural design, will make the 2-2 lamellar composites comprised of $[011]$ poled relaxor-PT single crystals promising for hydrostatic transducer applications [99].

3.3.3 External Field Stability of Piezoelectric Properties

3.3.3.1 Thermal stability of the piezoelectric properties: The thermal stability of dielectric and piezoelectric properties is very important for most electromechanical applications, such as medical imaging and underwater acoustic. In general, the dielectric and piezoelectric responses of relaxor-PT ferroelectric crystals exhibit relatively large temperature variation, owing to the multiple polymorphic phase transitions (PPTs) lying in or near the temperature range of -50 – 100°C [18,141,318]. Based on thermodynamic analysis of perovskite single crystals, the temperature dependence of the transverse dielectric permittivity is strongly related to the ferroelectric phase transitions. Fig. 25 (a) shows the temperature dependent piezoelectric variation of 10 single domain state crystals,

where the shear piezoelectric coefficient d_{24} was found to maintain similar value till T_{OT} transition temperature, with variation being less than 6 %, much less than that of d_{15} in the same temperature range, which was found to be on the order of ~200 % [339]. This phenomenon can be explained by the fact that the piezoelectric coefficients follow the same trend as the dielectric permittivity as a function of temperature, where the permittivity is greatly enhanced when approaching the MPB [339–340,446–448]. As given in Fig. 26, in $1O$ single domain state, two independent thickness shear vibrations exist, including d_{15} and d_{24} . When the sample is poled along $[011]_C$ and electrode on $(011)_C$ face, the applied electric field E_1 is along $[011]_C$ direction, leading to the piezoelectric shear deformation d_{15} , where the polarization will rotate from $[011]_C$ to $[001]_C$ direction, which is the spontaneous polarization of tetragonal phase. Thus, the temperature dependent d_{15} is related to the strongly curved O - T phase boundary, accounting for the strong temperature dependent behavior. On the contrary, for piezoelectric shear d_{24} deformation, the sample is poled along $[011]_C$ direction and electrode on $(100)_C$ face, the applied field E_2 is along $[100]_C$ direction, where the polarization will rotate from $[011]_C$ to $[111]_C$ direction, which is associated with the spontaneous polarization of rhombohedral phase; thus the temperature dependent thickness shear d_{24} corresponds to the vertical O - R phase boundary [339–340,449], exhibiting high thermal stability. As expected, the longitudinal coefficient d_{33} along $[111]_C$ direction for crystals with $3O$ engineered domain configuration, which is dominated by the value of d_{24} in $1O$ single domain state, was found to show temperature independent behavior (with variation of <6 % in the studied temperature range), yet with high value of ~900 pC/N, as given in Fig. 26 (b) [141,139,374].

3.3.3.2 Drive field stability: Ferroelectrics exhibit nonlinear properties under high drive field, owing to the interfaces (domain wall and/or phase boundary) motion [346,354]. The piezoelectric and dielectric responses of relaxor-PT single crystals generally increase with increasing drive field up to a threshold value, above which the samples will be depolarized and lose the piezoelectric activity [171,450]. The threshold value is closely related to the respective coercive field of ferroelectrics, which is on the order of 2–10 kV/cm for relaxor-PT crystals, depending on the phase and composition. For the longitudinal vibration mode, the allowable drive field level can generally go up to three times of their respective coercive fields when the transducer is driven by a pulse field, as shown in Figure 14 [198]. In the case of thickness shear vibrations, however, it is a totally different scenario, due to the fact that the working direction of thickness shear is perpendicular to the poling direction, where the allowable drive field is much lower than the respective coercive field [374,375]. As listed in Table XIII, the field stability ratios (allowable drive field level divided by coercive field) of pure relaxor-PT single crystals were found to be on the order of ~40% for thickness shear modes, less than half of the coercive field, regardless of crystal systems, whereas the 2nd generation crystals, such as PIN-PMN-PT, offer the advantage of higher allowable drive fields owing to their higher coercive fields, being double the value of PMN-PT binary counterparts [141,375]. Of particular significance is that for the acceptor (Mn) modified relaxor-PT single crystals (3rd generation crystals), internal bias was found to be on the order of 0.6–1.2kV/cm [143,273,298], leading to the enhanced allowable drive field, with field stability ratio increasing to >65 %, which is much higher than those of pure counterparts [375]. Furthermore, it should be noted that the drive field stability of relaxor-

PT crystals can also be enhanced by applying the uniaxial stress to crystals [451], which will be discussed in the following section.

3.3.3.3 Uniaxial prestress: Electroacoustic transducers with tonpilz structures (widely used for underwater acoustic, ultrasonic medical surgery, NDT/NDE, ultrasonic cleaning, to name a few) includes the piezoelectric elements, tail mass and head mass, and the stress bolt connecting the head and tail masses by running through the piezoelectric elements. When tightened, this bolt generates a compressive stress bias through the piezoelectric elements. These piezoelectric materials tend to fail under relatively small tensile stress (often 10–20 MPa without special surface preparation), but can survive very high compressive stress [10]. With no stress bolt present, actuation of the piezoelectric elements would result in equal operation under tension and compression, but the compressive stress bias prevents operating in tension and allows the transducer to operate at much higher drive levels [10]. Thus, it is desirable to understand the piezoelectric behavior under uniaxial prestress.

Fig. 27 shows the strain-electric field (S-E) loops measured at 5 kV/cm bipolar electric field and 0–20 MPa prestress for 3rd generation crystals (PIN-PMN-PT:Mn). As shown in Fig. 27 (a), when the bipolar electric field is below 5 kV/cm (coercive field is about 7 kV/cm) [298], the crystal sample showed linear strain-field relationship with no concern of depoling, and the piezoelectric coefficient was calculated from the slope of S-E loop and found to be 1700 pm/V. With an increasing prestress, domain reversal occurs, as demonstrated by the typical butterfly strain loops, with greatly decreased coercive field (from ~7 kV/cm to 1.5 kV/cm) and negative strain level (from 0.9 ‰ to 0.13 ‰). Meanwhile, the piezoelectric coefficient was found to increase to 2500 pm/V at prestress of 10MPa, and then slightly decreased to 2000 pm/V at 20 MPa, and the negative strain was found to be zero when the prestress was further increased to 40 MPa (not shown here), revealing the loss of piezoelectricity [452]. This phenomenon can be explained by the stress induced phase transition and depolarization, as shown in Fig. 28. In crystals with a *4R* engineered domain configuration, 71° and 109° ferroelastic domains exist, with polarization vectors pointing to [111], $\bar{1}\bar{1}\bar{1}$, $\bar{1}\bar{1}\bar{1}$ and [111] directions [181,340]. As the compressive stress is applied along [001] direction, the polar vectors of [001] oriented rhombohedral crystals will rotate from $\langle 111 \rangle$ to $\langle 011 \rangle$ directions, as shown in Fig. 28 (a)–(b). It is proper to believe that the compressive stress induces the rhombohedral crystals approaching *R-O* phase transition, and is responsible for the increase of piezoelectric coefficient at prestress of 10 MPa. With further increasing the compressive stress, the crystals may transform to the *O* phase or be depolarized by the stress as shown in Fig. 28 (c)–(d). Thus, the piezoelectric coefficient was found to decrease at prestress of 20 MPa and disappear at prestress of 40 MPa.

In order to maintain the linear strain behavior and avoid the depolarization under prestress, *dc* bias is generally applied to the piezoelectric materials [10,18,325]. Fig. 27 (b) shows the bipolar strain behavior at 10 MPa uniaxial prestress and applied *ac* field of 5 kV/cm, as a function of *dc* bias. The S-E loop measured at 10 MPa and zero *dc* bias exhibits a typical butterfly shape, with negative strain being on the order of 0.13 ‰, indicating that domain switch will occur if the crystal is driven by *ac* field under certain prestress, which will induce strain nonlinearity and deteriorate the drive field stability. It is interesting to note

when a positive dc bias field was applied to the crystal, the center of the electric field was shifted toward the positive side. As a result of the increased amplitude of the positive dc bias field, the field-induced strain was extended as well on the negative side of the ac field, leading to a negative strain of 1.3 %. It is quite obvious that the driving electric field range, in which the crystal exhibits a linear strain response, is expanded to ± 4 kV/cm or ± 6 kV/cm respectively when a 2 kV/cm or 4 kV/cm dc bias is applied, indicating that the reduced linear range of the strain response for PIN-PMN-PT:Mn crystals under an uniaxial prestress could be recovered by application of a positive dc bias to the crystal [452]. Of particular interest is that the strain loops show similar slopes, leading to a similar piezoelectric coefficient of ~ 2400 – 2500 pm/V, demonstrating that the dc bias field being on the order of < 4 kV/cm has minimal effect on the piezoelectricity.

Fig. 29 shows the bipolar strain behavior of transverse vibration for PIN-PMN-PT:Mn crystals at 5 kV/cm ac field and various transverse prestress levels, with measurements on pure crystals given in the small inset for comparison. It was found that all the strain curves for doped crystals are linear and non-hysteretic, demonstrating no domain reversal occurs at 5 kV/cm under different prestress conditions; however, large hysteresis was observed for pure crystals, revealing that an ac field (~ 5 kV/cm) induces domain wall motion and leads to depolarization in pure crystals. This can be explained by the enhanced coercive field (~ 7 kV/cm) and existence of internal bias (~ 0.6 kV/cm) of manganese modified crystals [298], which will clamp domain wall motion and stabilize the domains. The corresponding piezoelectric coefficient d_{32} as a function of prestress for doped and pure crystals are given in Fig. 29 (b), where one can see that the piezoelectric coefficient of PIN-PMN-PT:Mn crystals is about -1450 pm/V at 0 MPa and decreased to ~ -1000 pm/V at 21 MPa [453]. Of particular significance is that the piezoelectric coefficients measured with decompression sweep are similar to the values with loading sweep, indicating the ac driving field at 5 kV/cm has minimal effect on the piezoelectric properties of manganese modified crystals. On the contrary, it was found that the piezoelectric coefficients for pure PIN-PMN-PT crystals with both deep rhombohedral and MPB compositions decreased greatly under the combination of ac electric field and prestress, being on the order of 400 pm/V at 21 MPa, maintaining the same values during decompression sweep, indicative of the occurrence of depolarization [453].

In order to understand the piezoelectric properties under the combination of ac electric field and transverse stress, schematic of $[011]_C$ poled rhombohedral relaxor-PT single crystal is given in Fig. 30. For $[011]_C$ poled R crystals, 180° ferroelectric domains and 109° ferroelastic domains reversed with applying electric field along $[011]_C$ direction. Only 71° ferroelastic domains remain with polarization vectors pointing at $[111]_C$ and $[\bar{1}\bar{1}\bar{1}]_C$ directions, exhibiting “ $2R$ ” engineered domain configuration [181]. The polarization rotates from $\langle 111 \rangle_C$ directions to $[011]_C$ direction via Cm monoclinic $(011)_C$ plane under an applied electric field along $[011]_C$ direction, while the transverse compressive stress along $[100]_C$ direction will move the polarization vectors away from the stress field direction and favor the poling state along $[011]_C$. Apparently, $[100]_C$ transverse preload tends to increase the transverse extensional piezoelectric d_{32} values under $[011]_C$ electric field, via the MPB shift with the mechanical stress. The R - O MPB was thought to shift to lower PT content

with increasing compressive stress, indicating that the studied R crystal is approaching the R - O phase boundary with increasing stress, thus leading to higher piezoelectric properties [324,454–455], analogue to the [001] prestress on [001] poled R crystals (shown in Fig. 28). However, if the composition of the studied crystal is on the proximity of MPB region, both the electric field and preload stress are cooperative driving forces for the R to O phase transformation [226]. This leads to a dramatic drop in the strain level along $[100]_C$ direction due to the field/stress induced orthorhombic single domain state, accounting for the significantly decreased d_{32} [453]. On the other hand, the ac bipolar drive field with magnitude of respective coercive field will induce domain reversal and lead to depolarization under transverse stress, even for the composition away from the MPB. In addition, the ac field will induce microcracks in the crystals under transverse compression due to the large anisotropic characteristics in $[011]$ poled crystals with $mm2$ macroscopic symmetry, where the depolarization is unrecoverable during the decompression sweep, as in the case of pure PIN-PMN-PT crystals. The manganese modified crystals, however, show depolarization-resistant behavior. This is due to the fact that the enhanced coercive field and existence of internal bias favor the poling state as a result of clamped domain wall motion and reduced polarization rotation, demonstrating that the 3rd generation crystals (for example, PIN-PMN-PT:Mn) are promising for acoustic transducer applications [453].

Fig. 31 shows the P - E curves as a function of compressive uniaxial prestress for thickness shear-mode PIN-PMN-PT crystals with $1T$ and $2R$ domain structures, respectively [451]. It should be noted that P - E loops were used for the thickness shear vibrations, instead of strain curves, due to the limitation of the measurement fixture. It was reported that the allowable drive field for thickness shear vibration is about ~40 % of its respective coercive field [375]. Thus, the P - E loops exhibit large hysteresis at the drive field of 4kV/cm ($> \frac{1}{2}E_C$), under zero uniaxial stress for both $1T$ and $2R$ domain configurations due to the irreversible domain wall motion, leading to the depolarization of the samples. Of particular significance is that the hysteretic properties of both $1T$ and $2R$ crystals were greatly reduced by applying compressive stress to the crystals, owing to the stabilized domains by the compression prestress, as shown in Fig. 32. Therefore, the allowable electric fields can be enhanced by applying uniaxial compressive stress perpendicular to the poling direction, which were found to increase to 4.5 kV/cm and 4 kV/cm for $1T$ crystals at compressive stress of 25 MPa and $2R$ crystals at 55 MPa, respectively [451]. With applying compressive stress, though the shear piezoelectric response decreased due to the decreased dielectric permittivity [340,456–458], as confirmed by the decreased slope of the P - E loops, the level of allowable drive field increased. Therefore, the improvement in maximum shear-strain is expected by applying compressive stress. The S_{\max} of $1T$ crystals was increased by 38 % under compressive stress of 25 MPa (from 0.5 % to 0.7 %), while the S_{\max} of $2R$ crystals was increased by 50 % under compressive stress of 55 MPa (from 0.7 % to 1.0 %). In addition, the dielectric loss factors can be evaluated by the hysteresis area of the P - E loops [141,459]. The values are on the order of 20 % and 50 % for $2R$ and $1T$ crystals, respectively, at electric field of 4 kV/cm without applying stress, being reduced to the order of 4 % by applying compressive stresses of 55 MPa and 25 MPa for $2R$ and $1T$ crystals, respectively, which will benefit the general transducer applications (reduced heat generation). Thus, the results indicated that the allowable drive electric field of the thickness shear-mode crystals can be enhanced by

applying compressive stress perpendicular to the polar direction (the same direction of the applied ac field) and lead to increased shear strain [451].

3.3.4 Cross-talk associated with shear modes—Cross-talk is a complex phenomenon in electromechanical applications, electrically or mechanically, which will produce an error in the measured output signal for sensing applications and lead to a high noise level, or introduce extra displacement other than the required; thus, it is important to understand the piezoelectric cross-talk and the approach to eliminate the effect [460]. For example, the thickness shear piezoelectric d_{16} , on the order of -1700 pC/N, was observed in crystals with [111] poled rhombohedral relaxor-PT crystals ($1R$ single domain state) and strongly cross-talks with piezoelectric d_{15} [332]. Under this condition, the [111]/(110) samples will generate an electric signal E_1 under both S_5/T_5 and S_6/T_6 strain/stress, as shown in Fig. 33, which hinders the detection of signal S_5/T_5 and S_6/T_6 independently. Thus, it is desirable to reduce or eliminate the cross-talk effect in practical applications. It was reported that d_{16} can be eliminated by rotating the sample around X -axis with angle of

$\alpha = \arctan\left(\frac{-d_{16}}{d_{15}}\right)$ [332,461,462]. Another approach to obtain thickness shear samples without cross-talk includes the utilization of domain configurations other than $1R$ single domain state, such as $1T$ and $1O/2R$ with macroscopic symmetries of $4mm$ and $mm2$, respectively, where the d_{16} value is zero [321,374]. It should be noted that for face shear vibration, cross-talk from extensional vibrations d_{31} or d_{32} can be eliminated by rotating the sample along Z -axis with angle of $\alpha = \arctan\left(\frac{d_{31}}{-d_{32}}\right)$ or $\alpha = \arctan\left(\frac{-d_{32}}{d_{31}}\right)$, respectively, without sacrificing the large d_{36} [374,463] as shown in Fig. 34 (a), however, the other d_{32} or d_{31} mode yet presents. This is due to the fact that for $Zt\theta$ cut plate with $mm2$ symmetry, there exist $s'_{16} = s'_{26} \neq 0$ and $d'_{31} = d'_{32} \neq 0$. Thus, the face shear is always coupled to face longitudinal mode [464–465].

It is known that elastic matrix of $4mm$ crystals, such as $[001]_C$ poled relaxor-PT crystals is the same as that of 42 , which only possesses face shear piezoelectric coefficients d_{14} and d_{36} . However, the face shear mode cannot be excited through piezoelectric effect if d_{36} is zero in $4mm$ symmetry. It is observed that when Euler rotation is made for $4mm$ plate, face shear d_{36} exists under the rotated coordinate:

$$d'_{36} = \frac{1}{2} \sin\theta \sin 2\theta \sin 2\psi (d_{33} - d_{31} - d_{15})$$

Here θ and ψ are the second and third Euler angles. It is seen from the equation that is d'_{36} independent of the first Euler angle ϕ (i.e the rotation about Z -axis). When one of θ and ψ is zero, $d'_{36} = 0$. Thus, different from $mm2$ symmetry, any single-rotated $4mm$ plate, such as $Zt\theta$ cut, cannot support face shear mode. The non-vanished d_{36} can appear for the double-rotated $ZXlt \theta/\psi$ cut plate as shown in Fig. 34 (b), where the thickness and other two edges of the plate are along Z -, Y - X - axes, respectively. To get such a plate, the coordinate is rotated first about X -axis by θ , then rotated about new Z -axis (Z') by ψ . It is seen from the equation that

when $\theta = \cos^{-1}(\sqrt{\frac{1}{3}})$ and $\psi = \frac{\pi}{4}$, d'_{36} reaches its maximum and $(d'_{36})_{\max} = 0.385(d_{33} - d_{31} - d_{15})$. For the double-rotated cut, there exist $s'_{16} = s'_{26} \neq 0$, $d'_{31} = d'_{32} \neq 0$, which are similar to *Zt* 45° rotated *mm2* plate. The calculated results are listed in Table XIV and compared to those of *Zt* 45° rotated *mm2* plate. For the double-rotated *4mm* plate, the electromechanical coupling factor k_{36} is much less than *Zt* 45° *mm2* plate, but with similar value of d_{36} , being on the order of >1500 pC/N. Of particular significance is that the transverse piezoelectrics are much less than those of the face shear piezoelectric $d'_{31} = d'_{32} \ll d'_{36}$, promising for sensing applications demanding no crosstalks.

It should be noted that the piezoelectric cross-talk can also be reduced or eliminated by specifically designed sensor/transducer structures. To illustrate this idea, we give an example of a sensor design by using *24* shear mode of *IR* relaxor-PT crystals. From piezoelectric coefficient matrix (Fig. 33), it is known that the piezoelectric coefficients d_{21} and d_{22} play as cross-talks for shear mode d_{24} in *IR* relaxor-PT crystals. Figure 35 gives the special design to eliminate the impact of piezoelectric coefficients d_{21} and d_{22} . By this design, the electric signal induced by stress T_1 and T_2 can be eliminated, while the electric signal induced by shear stress T_4 is doubled. Compared to the *15*-mode, the particular merit of *24*-mode in *IR* domain configuration is that the crystal doesn't need to be rotated by a special angle and cut again after poling for eliminating the cross-talk effect, meanwhile, keep the same properties as *15*-mode [466].

3.4 Piezoelectric tactile sensors

Tactile sensor is a device that is able to detect a given property, such as pressure, force, temperature, elasticity, etc., of a contact event in a predetermined area and subsequent pre-processing of the signals [467,468]. Tactile sensors have been broadly applied in automotive, electronics, intelligent machinery, defense and biomedical industry.

3.4.1 Piezoelectric materials and FOM for tactile sensors—Among numerous types of tactile sensors including piezoresistive, capacitive, piezoelectric, optical, and ultrasonic wave types (as given in Fig. 36), piezoelectric type is cost effective, simple, and highly sensitive to dynamic contact deformation [468]. However, the piezoelectric sensor based on direct piezoelectricity (or direct piezoelectric sensing) requires additional electrical circuitry for a quasi-static tactile sensing [469]. On the other hand, piezoelectric resonators including bulk acoustic wave (BAW) and surface acoustic wave (SAW) resonators are capable of both dynamic and static measurements. This type of piezoelectric sensing is also called resonant piezoelectric sensing or acoustic wave sensing. In contrast to direct piezoelectric sensors, the sensing performance of these resonant piezoelectric tactile/bio sensors is heavily dependent on the resonance properties of piezoelectric materials [470,471].

In the medical field, piezoelectric tactile sensors have been developed for measuring the elastic stiffness of tissues [472–475]. Examples include the endoscopic sensor in minimally invasive surgery (MIS) [476–477], the smart skin used in diagnosing the breast tumor or prostate gland disease, and also sensors for the intraocular pressure (IOP) in the human eye

[478]. Typical resonator sensors measure changes in the resonant frequency caused by interaction between piezoelectric resonator and target materials. The change in the resonant frequency is directly proportional to the applied force by the Sauerbrey equation [479]. The local distribution of the applied mechanical stress can be detected by measuring the fundamental frequency shift of the resonator array. A relatively new tactile sensing technique, which uses the relationship between electrical impedance of the piezoelectric resonator and acoustic load impedance of the front load, has been developed for the fingerprinting application [480]. The electrical impedance of piezoelectric elements at particular frequency is changed when an object is applied to the front surface of a sensor. This change is related to the acoustic impedance of the applied objects. As a result, the distribution of the acoustic load impedance of the object can be mapped by measuring the electrical impedance of each element of the array in a rapid fashion. This device can be highly sensitive as a biometric sensor compared to capacitive and thermal tactile sensors since the contrast ratio of acoustic impedance between air and tissue is 4000:1, while that of thermal conductivity is about 8:1 and dielectric permittivity is 32:1 [481]. For these reasons, this acoustic impedance sensing is promising for applications in the biomedical industry (artificial skin sensor) and service robotics (touch screen and fingerprint reader).

The most known material of direct piezoelectric tactile sensor is PVDF piezoelectric polymer. Although piezoelectric ceramics and single crystals have much higher piezoelectricity, the piezoelectric polymers are preferred in non-resonant tactile sensing application due to their high piezoelectric voltage g coefficients, excellent flexibility and biocompatibility [482–483]. On the other hand, acceptor doped ceramics and quartz crystals with high mechanical quality factors were adopted in the resonance-based tactile sensors, where the variation of resonant frequency and impedance at resonance are sensing parameters [484–485]. The key material properties of the conventional piezoelectric materials for the tactile sensing applications are presented in Table XV. Therefore, the FOM of the piezoelectric materials for the non-resonant type piezoelectric tactile sensor can be defined as piezoelectric voltage coefficient ($g_{ij}=d_{ij}/\epsilon$), while the FOM of resonant type tactile sensor can be dQ_m or k_2Q_m , which is similar to the high power ultrasound transducer applications.

3.4.2 Advantages and Challenges of Relaxor-PT Crystals—The FOM of dQ_m or k_2Q_m among various relaxor-PT crystals is shown in Table X and XI, which suggests that Mn-doped PIN-PMN-PT crystals exhibit the highest dQ_m of 1050×10^3 pC/N, being much higher than quartz and acceptor doped ceramics. Of interest is that the face-shear mode relaxor-PT crystals have drawn research attention due to their high piezoelectric coefficients (e.g. d_{36} of 1600–2800 pC/N) and ultrahigh elastic compliances ($s_{66}^E > 120 \text{ pm}^2/\text{N}$). More importantly, unlike thickness shear mode, the face shear mode was found to possess much higher mechanical quality factor Q_m (> 120 , compared to ~ 30 for thickness shear mode) and can be easily repolarized since the poling electrodes are the same as the active electrodes [335]. These unique properties suggest the need of further study on face shear mode single crystals for potential advanced applications.

By using the face-shear mode PMN-PT single crystal resonators, a new type of tactile sensor has been developed [378–380]. In this reported sensor configuration, the thin polymer layer (silicone rubber) was used as a sensing layer and attached to the large surface of a face shear mode resonator. The electrical impedance amplitude changes induced by the applied surface loads were measured. The sensitivity or the ratio of electrical impedance change to the surface load variations was calculated and compared among thickness mode, thickness-shear mode and face-shear mode single crystal piezoelectric resonators. Fig. 37 presents the results of measured electrical impedance changing with acoustic load impedance in three different modes at resonant frequency. One can observe that for the face-shear mode resonator, the electrical impedance increased rapidly with the increasing acoustic impedances of surface loads at the resonant frequency. This is in stark contrast to the findings from thickness and thickness-shear mode resonators with similar sizes. Specifically, the ratio of electrical impedance shift to the applied acoustic impedance of the face-shear mode resonator was found to be at least 20 times and 90 times higher than those of thickness-shear mode and thickness mode resonators, respectively.

In addition to the single element acoustic load sensor, face shear mode tactile sensor array was developed by Kim *et al* [378]. The 8×8 tactile sensor array is composed of aforementioned sensors. The face shear mode PMN-PT single crystal plates (820×820×300 μm^3) were also used as an active material. One difference of the sensing element is that polydimethylsiloxane (PDMS) was used as the sensing layer instead of the silicone rubber. This is because PDMS is transparent, flexible and has low acoustic impedance. Based on the sensing element design, the array exhibited the spatial resolution of 1.1 mm, which is high enough as a tactile sensor application. The fabricated array was tested with different liquids such as water and isopropyl alcohol (IPA) due to their different acoustic impedance: 1.5 MRayl (water) and 0.9 MRayl (IPA), respectively. The electrical impedance change due to the applied liquid drop was measured using impedance analyzer. The sensor array with a water drop and corresponding mapped image is shown in Fig. 38. The dark elements in the mapped image show larger electric impedance shift due to the water drop. On the other hand the bright area indicated small impedance shift at the resonant frequency. The electrical impedance shift variation is caused by surface force distribution on the sensing array and the droplet thickness variation. Going forward, the challenge of current piezoelectric tactile sensing technology by both resonant and non-resonant types is temperature dependency [483,489], and this is also the limitation of relaxor-PT crystals. Thus, temperature-independent properties of domain-engineered crystals can be considered together with aforementioned FOM for tactile sensor applications.

3.5 Acoustic Tweezers

Acoustic tweezers is a device that can remotely capture and manipulate target particles using acoustic waves. Acoustic tweezers has been widely researched for medical, biological, and chemical applications [490,491]. Optical tweezers has been the most well-known and widely used contact-free method due to its high precision, but it is also known to have several drawbacks. First, optical tweezers works only for optically transparent and shallow media. Second, the target particles can be damaged due to the high intensity of a focused laser. Third, it is difficult to be miniaturized since the required apparatus are bulky, expensive, and

complicated [492,493]. These problems can be relieved to some degree by using acoustic tweezers because of its relative simplicity, independence to the targets' material properties, and non-invasiveness to biological objects. Thus, acoustic tweezers has been actively researched over the last two decades.

3.5.1 Piezoelectric materials for acoustic tweezers—Based on the numerous reported acoustic tweezing methods, the operation mode can be categorized into (a) standing bulk acoustic wave (SBAW), (b) standing surface acoustic wave (SSAW), and (c) single beam mode (Fig. 39).

(a) Standing bulk acoustic wave: In order to superpose two or more beams, multiple ultrasonic transducers or one transducer with a reflector are used for the SBAW mode manipulation [494]. In the standing wave field, the stationary points of the zero acoustic pressure amplitude (pressure node) coincide with the maximum velocity (velocity anti-node) [495]. The gradient of the acoustic pressure (Bernoulli pressure) leads to a steady-state acoustic radiation force. Thus, the particles are typically trapped in the pressure node (velocity anti-node) of the standing wave field [496,497], and then the trapped particles are manipulated by changing the frequency of the acoustic waves [494]. In this mode, the general operating frequency range was from 1 to 15 MHz, and PZT4 piezoelectric ceramic transducers were used in the reported studies because of their relatively high Q_m [498,499]. (b) Standing surface acoustic wave mode: For the integration of a manipulation system with microfluidics, particle manipulations using SSAW was developed [500]. SSAW tweezers is composed of two equal inter-digital transducers (IDTs) and a microfluidic channel. The most of IDTs for SSAW tweezers are made of Y+128° X-propagation lithium niobate (LiNbO_3) due to its high coupling factor in SAW generation [500,501]. The interference of two SAWs at the fluid in the microchannel generates a standing wave field. Therefore, the microparticles are aligned and patterned inside the microchannel [502]. In comparison with SBAW, SSAW has several advantages. First, the frequency can be easily increased up to hundreds of megahertz for highly precise manipulations. Second, SSAW tweezers can be easily integrated into a microsystem, because the reflector is not necessary, whereas SBAW requires almost perfect acoustic reflection from the microchannel, but microchannels are usually made of PDMS, which has a poor acoustic reflection in fluid [502]. (c) Single beam acoustic wave: The single beam acoustic trapping can manipulate a single particle by using a single acoustic beam, while the standing wave approach only works for trapping a group of particles [503,504]. For the single beam tweezing, highly focused ultrasound beam is necessary because it generates a negative radiation force that pulls the particle towards the focal point. A sharp acoustic intensity variation along the lateral direction of the acoustic beam is the requirement for the single beam tweezers [505]. It was reported that tightly focused beams at 96 MHz and 200 MHz are able to capture lipid particles with a size of 50 μm and 10 μm in diameter, respectively [504,506]. Large aperture and thin thickness of the piezoelectric component is usually desired for very high frequency (> 100 MHz) focused ultrasound with a sharp focus. Therefore, zinc oxide (ZnO) film and LiNbO_3 single crystals have been broadly utilized for high frequency focused ultrasound transducers due to their low dielectric permittivity and acceptable electro-mechanical couplings [504,507].

3.5.2 Advantages and Challenges of Relaxor-PT Crystals—Although the LiNbO_3 single crystal is the dominant piezoelectric material for SSAW and single beam tweezers, the superior piezoelectric and dielectric properties of relaxor-PT single crystals have also been studied for particle manipulations using microfluidic devices [508,509] and needle transducers [510]. The common motivation to use PMN-PT single crystals is the miniaturization of the ultrasound transducer with an acceptable radiation force. For miniaturized transducers, high dielectric constant of active material is desirable because the transducer can maintain acceptable electrical impedance [510]. In addition, high piezoelectricity and electro-mechanical coupling are always a plus in focused ultrasound. Therefore, it is fair to say that relaxor-PT single crystal is a promising candidate for acoustic tweezers due to its superior piezoelectric, dielectric, and couplings compared to PZT, ZnO , and LiNbO_3 .

The Needle transducers for ultrasonic imaging and tweezing made of PMN-PT single crystals were developed by Hsu *et al.* (Fig. 40) [510]. At the resonant frequency, the maximum displacement of the target particle was measured to determine the distance through which the target particle can be pulled by the trapping force. This result showed that the PMN-PT single beam tweezers can manipulate a microparticle (15 μm) with the size smaller than the wavelength of the ultrasound wave (24 μm) [510]. The microfluidic device for standing BAW tweezing was developed using PMN-33%PT single crystals (Fig. 41) [508]. The polystyrene particles were trapped at the center of the cavity within 200 ms after the electric field was applied at resonant frequency [508]. This result shows that the PMN-33%PT single crystals can be promising to generate enough amplitude of the standing wave field in miniaturized tweezers.

FOM of piezoelectric materials for acoustic tweezers can then be determined on the basis of the acoustic tweezers types. For SBAW and SSAW acoustic tweezers, mechanical Q_m and piezoelectricity of piezoelectric materials are the key parameters to consider. In the aspect of SAW based tweezers, the PMN-PT crystal has more promising points than LiNbO_3 , which is the most-used piezo-substrate for SAW. PMN-PT crystals with MPB composition showed lower surface acoustic velocity, higher coupling factor, and lower power flow angle (PFA) than those of LiNbO_3 [511]. The low acoustic wave velocity is required for high manipulation resolution at miniaturized dimension, and low power flow angle is advantageous for reduced acoustic attenuation and improve electromechanical performance of SAW devices. The maximum coupling factor, minimum velocity, and minimum PFA of Y-cut PMN-PT single crystal are 0.35, 1156 m/s, and 1.5°, respectively, whereas the LiNbO_3 substrate has those parameters of 0.2, 3300 m/s, and 7°, respectively [511]. Therefore, the PMN-PT crystals have great merits for miniaturized SSAW tweezers. On the other hand, the single beam tweezers showed more promising performance for the precise manipulation of a single microparticle compared to SBAW or SSAW tweezers. For the single beam tweezers, high acoustic power at the resonant frequency is required. The operation frequency is not usually modulated during a particle manipulation. Therefore, the FOM of piezoelectric materials for the single beam acoustic tweezers can be similar to high power therapeutic applications (dQ_m and/or $k^2 Q_m$). Thus, the Mn-doped PIN-PMN-PT can show better performance than PMN-PT crystal in single beam tweezing application, because

the Mn:PIN-PMN-PT has much higher dQ_m (1050×10^3) than PMN-PT crystals ($\sim 420 \times 10^3$). Although high resonance performance may be most important for the single beam tweezers, the miniaturized transducer for imaging and tweezing, as in [510], need to be designed aiming both high power and wide bandwidth. Moreover, desirable dielectric property for miniaturized transducers also conflicts with the large aperture and high frequency (>100 MHz) design. Therefore, one may design a SBAW, a SSAW or a single beam acoustic tweezers using respective piezoelectric materials to meet the specific application requirements.

3.6 Ultrasonic Motors

Ultrasonic motor (USM) is a motor operated by the ultrasonic vibration. The applied electrical signal is converted to the elastic waves in active material attached to a stator, and then the friction tip on the stator can excite the rotor by ultrasonic vibration. Miniaturized motors have been in great demand in various electromechanical systems such as camera modules, deformable mirrors, precision positioning adaptive structures in aerospace applications and biomedical instruments [513].

3.6.1 Piezoelectric Materials for Ultrasonic Motors—The USMs are known to have high efficiency and accuracy in millimeter or micrometer scale, whereas the conventional electromagnetic (EM) motors are suggested with very low power density and poor efficiency, accuracy, and reliability [514]. Thus, numerous designs of USMs have been developed such as travelling wave motors, wobbling mode motors, shear mode disk rotary motor, and hybrid mode linear motors [367,513,515]. All these piezoelectric ultrasonic motors operating in friction drive mechanism at resonance exhibit quick response, high resolution in positioning, low profile, and high power density [513,516,517]. These motors usually adopt piezoelectric materials in the driving components, and operate at resonance for the maximum electric-to-mechanical energy conversion [382,518].

Hard piezoelectric materials with a high mechanical quality factor Q_m are considered proper driving materials in order to minimize heat generation and maximize the displacement at resonance [518]. For example, PZT4 and PZT8 ceramics that have Q_m of 500 and 1000, respectively, have been often used in piezo-motor applications [513,515]. Other piezoelectric material properties such as piezoelectric coefficients, electromechanical couplings, dielectric constants, etc. are also important parameters to be considered in USMs for high energy density. As an example, the energy density (U) in a USM under a lateral mode resonance driving can be simplified as the following equation [519].

$$U = \frac{1}{2} Q_{m31}^2 k_{31}^2 \varepsilon_{33} E^2 = \frac{1}{2 s_{11}^E} Q_{m31}^2 d_{31}^2 E^2$$

where k_{31} is the electromechanical coupling factor, ε_{33} is the dielectric constant, E is the electric field, d_{31} is the piezoelectric coefficient, and s_{11}^E is the elastic compliance of a piezoelectric material. This equation shows that high mechanical quality factor, electromechanical coupling factor, and dielectric constant are advantageous for high energy density of USMs [520].

Therefore, the FOM can be closely related to the energy density shown in the above equation and can be determined as $Q_m^2 k_{ijkl}^2 \varepsilon_{ij}$ ($i, j, k, l = 1, 2, 3$). This FOM is similar to that of materials for the therapeutic and surgical high power ultrasound. The advantages and challenges for this application are also similar to the high power ultrasound applications described in section 3.2.2. The difference is that the piezo-motors usually operate in more than two modes including a lateral mode (31 mode), thickness mode, and shear mode, whereas the high power ultrasound usually only involves one vibration mode.

3.6.2 Advantages and Challenges of Relaxor-PT Single Crystals—Generally, in spite of their high piezoelectric and dielectric properties, relaxor-PT single crystals are not optimal driving materials for piezo-motors due to their relatively low Q_m . However, for miniaturized USM designs working in non-continuous mode, the heat generation by the loss is not an issue, and hence relaxor-PT crystals can be used as a driving material because of their high dielectric constants and electromechanical couplings. Ci *et al.* developed a standing wave PMN-PT single crystal ultrasonic linear motor operating in high-order face shear modes (FS-2 and FS-3 modes) and compared with a larger size piezo-ceramic motor [382]. Fig. 42 schematically shows the USM with motion trajectories of the two non-isomorphic in-plane face-shear vibration modes [382]. Face shear mode of the PMN-PT crystal was utilized for the USM design due to its prominent electromechanical coupling (0.77–0.83) and higher Q_m (100–450). The prototyped face shear mode motor exhibited large generating force (e.g. 1.0 N) at a relatively low driving voltage (50 V_{pp}), which is really impressive compared to even larger size PZT motors [382,521].

In addition to the high Q_m and high coupling, the high coercive field E_c is also advantageous to USMs operating at their resonance frequency since higher driving field can be applied to improve the energy density, according to the above equation. Therefore, the second generation crystals, PIN-PMN-PT, were adopted to develop a double-mode piezoelectric rectangular plate actuator due to the higher E_c (~5 kV/cm), which is one of the simplest designs of piezoelectric motors [514]. The first longitudinal (L1) and the second bending (B2) mode were excited to generate an elliptical motion of the frictional tip (Fig. 43) [522]. The displacement of the developed motor along the longitudinal direction was ~0.11 μm under 5 V input voltage, which is comparable to the performance of the multilayer piezo-ceramic motors [514].

Considering the fact that the mechanical quality factor and coupling factors equally affect the energy density, the 3rd generation relaxor-PT crystals can be a promising driving material due to their even higher Q_m . For example, [001]_C poled Mn:PIN-PMN-PT crystal shows k_{31} of 0.49, Q_{31} of 500, and $\varepsilon_{33}^T/\varepsilon_0$ of 3810 [304], and then the FOM is 229×10^6 , which is much larger than those of conventional hard piezo-ceramics including PZT8 and PZT4 ceramics, with FOM of 90×10^6 and 35×10^6 , respectively (Table XVI).

3.6.3 Relaxor-PT Single Crystal Cryogenic Motors—In addition to the high energy density of relaxor-PT single crystal USMs, excellent cryogenic properties of relaxor-PT crystals, as described in section 2.3.3, are also attractive characteristics of relaxor-PT single crystal USMs. PMN-PT single crystal wobbling mode linear piezo-motor and PMN-PT

single crystal traveling wave linear and rotary motors were developed recently for cryogenic actuation applications [367].

Fig. 44 shows a PMN-PT single crystal piezomotor based on wobbling mode with center coupling [359]. Two PMN-PT single crystal ring stacks were fabricated with segmented electrodes to apply one pair of voltage signals with a $\pi/2$ phase difference such that a “wobbling motion” at the center part of the stator was excited with high efficiency. The motor was driven at 41.5 kHz, and operated successfully from room temperature down to $-200\text{ }^{\circ}\text{C}$ [359]. Fig 45 shows the design of a single crystal traveling wave USM [366]. The motor was made of nine PMN-PT single crystal isosceles trapezoids, which were bonded on a titanium-alloy ring forming uni-morph structures and operated on a nine wavelengths (9λ) flexure traveling wave principle. The measured maximum torque output of this PMN-PT traveling wave motor was 1.5 kg-cm, the minimum step resolution was $0.072^{\circ}/\text{step}$, and the power consumption at a 25 % duty cycle was 2 W. This motor successfully operated in a liquid-nitrogen environment of 77 K under a load.

The cryogenic performance of the 2nd generation crystal motor was also reported. The wobbling mode linear motor using PIN-PMN-PT was developed and the cryogenic performance was characterized by Li *et al.* [523]. The measured cryogenic performance was prominent in comparison with that of the previously reported PZT ceramic based motor. The maximum linear speed of 75 mm/s at room temperature was decreased to 45 mm/s at the cryogenic temperature of $-175\text{ }^{\circ}\text{C}$. Although there was 50% decrement of the speed at the cryogenic temperature, this performance still shows great merits of the 2nd generation crystal in comparison for the cryogenic motor application in comparison with the conventional PZT ceramic based motor, which could work well at temperatures above $-80\text{ }^{\circ}\text{C}$, and stopped working completely at $-100\text{ }^{\circ}\text{C}$ [523].

The published work suggests that PMN-PT single crystal motors have a significant torque improvement relative to PZT ones, under relatively low voltages in cryogenic environments. The second generation and third generation relaxor-PT single crystals may be even more promising for cryogenic motors due to their increased quality factor Q_m and coercive field E_c .

IV. Summary

4.1 Impact and Significance of Relaxor-PT Crystals

Relaxor-PT single crystals have been some of the most important materials among the piezoelectric families, due to their ultrahigh piezoelectric coefficients and electromechanical coupling factors on the order of $>1500\text{ pC/N}$ and >0.9 (k_{33}), respectively, far outperforming state-of-the-art ferroelectric PZT ceramics. PMN-PT, as the first generation relaxor-PT crystals, have been successfully commercialized in medical diagnostic transducers, showing great advantages compared to their PZT ceramic counterparts. In addition to the ultrahigh piezoelectric properties, relaxor-PT crystals show strong anisotropic characteristics as well, resulting in some new piezoelectric modes which do not exist in ceramic counterparts, such as independent giant thickness shear piezoelectric coefficients d_{15}/d_{24} in [011] poled orthorhombic crystals with $mm2$ macroscopic symmetry and face shear d_{36} mode in [011]

poled rotated rhombohedral crystals. These properties can be unique in designing new and high performance piezoelectric devices for specific applications including miniaturized underwater transducer and biomedical sensing.

4.2 Challenges

Relaxor-PT crystals possess great advantages over conventional polycrystalline ceramics, being successfully employed for commercial medical imaging. Lots of challenges, however, are still present for the growth and utilization of relaxor-PT crystals, specifically for applications with operations over wide temperature range and at high power conditions, such as high power therapeutic transducers and underwater transducers. These challenges include, but are not limited to: how to achieve large crystals with homogeneous composition (related to crystal cost and property variation), how to enhance the coercive field (related to the input power), how to increase ferroelectric phase transition temperature T_{RT} (related to the temperature usage range), how to achieve temperature independent dielectric and piezoelectric properties (related to reliability and stability) and how to improve the mechanical quality factor (related to the output power). With respect to materials design, some improvements have been achieved in the second and third generation crystals, where the coercive field, T_{RT} and mechanical quality factor have been enhanced to some extents. In addition to materials design, researches on device design and modeling are also being challenged for better utilization of relaxor-PT crystals in new applications. By proper design, it is expected that the shortcomings of relaxor-PT crystals can be avoided in practical applications.

4.3 Future Research

PMN-PT and PIN-PMN-PT crystals have been successfully grown along $\langle 001 \rangle$ crystallographic direction, with 50–100 mm in diameter and 100–200 mm in length, by using the modified Bridgman method. However, the chemical inhomogeneity of the as-grown relaxor-PT crystals yet persists, albeit much improvement has been achieved by continuous top-feeding growth method. It is desirable to focus the research on the chemical homogeneity along the axial and radial directions of the crystals with efforts on the modified growth technique.

In addition, it is well accepted that relaxor-PT crystals show great advantages in piezoelectric devices, however, the applications have been mainly focused on some traditional areas, where PZT ceramics have been maturely utilized. In these areas, relaxor-PT crystal devices are generally designed following the techniques of PZT-ceramic devices. Although the devices may exhibit much improved performance when PZT ceramics are replaced by relaxor-PT crystals, new functionalities weren't achieved in these devices. In the future, designing devices with specific functionalities by utilizing relaxor-PT crystals is important and worthy of more research attention. As discussed in this review, relaxor-PT crystals exhibit lots of novel properties which do not exist in PZT ceramics. Thus, new devices for specific applications can be designed by considering these novel properties. For example, by using the piezoelectric face shear mode, relaxor-PT crystals have shown great potential for underwater acoustic and tactile sensing applications.

With the advancements of material and device developments, it is expected in the near future that various new electroacoustic transducers based on relaxor-PT crystals could play an increasingly important role in the respects of bio-detection, human health, security and life science.

Acknowledgements

This work was supported by ONR and NIH under Grant No. 2P41EB002182-15A1.O. Authors from NC State (X. Jiang and J. Kim) acknowledge the partial financial support from NIH under the Grant No. 1R01EB015508. The authors would like to thank Prof. Thomas R. Shrout for the helpful discussion and strong support, Prof. Wenhua Jiang for the discussion on face shear vibration, Ms. Yue Sun for the help on the schematic figures, Ms. Christie Jiang for the proof-reading.

Nomenclature

d_{ijk}	piezoelectric coefficient measured in the standard coordinate system, pC/N
d_{ijk}^*	piezoelectric coefficient measured/calculated in the rotated coordinate system, pC/N
d_h	hydrostatic piezoelectric charge coefficient, pC/N
g_h	hydrostatic piezoelectric voltage coefficient, Vm/N
K_{ijT}	dielectric constant under constant strain
K_{ijS}	dielectric constant under constant stress
k_{ip}/k	electromechanical coupling factor
k_t	electromechanical coupling factor for thickness mode
s_{iiE}	elastic compliance, m ² /N
Q_m	mechanical quality factor
T_C	Curie temperature, °C
T_{RT}	rhombohedral-tetragonal phase transition temperature, °C
T_{OT}	orthorhombic-tetragonal phase transition temperature, °C
E_C	coercive field, kV/cm
E_{int}	internal bias field, kV/cm
$Q_{\lambda\mu}$	electrostrictive coefficient, m ⁴ /C ²
ϵ_{33S}	dielectric permittivity under constant strain, F/m
ϵ_{33T}	dielectric permittivity under constant stress, F/m
c_{33D}	elastic stiffness under constant electric displacement, N/m ²
ρ	density, g/cm ³
c	elastic stiffness, N/m ²
v	vibration velocity of transducer surface, m/s

$\tan\delta$	dielectric loss
P_{disp}	dissipated power
ω	angular frequency
Y_r	Young's modulus
S	strain
P	acoustic power
R_r	radiation resistance
R	internal mechanical resistance
η_{ea}	electroacoustic efficiency
V_{rms}	the amplitude of measurement voltage
N_{ij}	frequency constant
NDT/NDE	non-destructive testing/evaluation
LN	LiNbO ₃
LT	LiTaO ₃
BT	BaTiO ₃
SAW	surface acoustic wave
BAW	bulk acoustic wave
SBAW	standing bulk acoustic wave
SSAW	standing surface acoustic wave
PNR	polar nanoregion
PMN	lead magnesium niobate
PMN-PT	Pb(Mg _{1/3} Nb _{2/3})O ₃ -PbTiO ₃
PZN-PT	Pb(Zn _{1/3} Nb _{2/3})O ₃ -PbTiO ₃
FOM	figure of merits
PZT	PbZrO ₃ -PbTiO ₃
PZT4, PZT5A, PZT5H, PZT8, etc.	impurities-labeled PZT
PIN-PMN-PT	Pb(In _{0.5} Nb _{0.5})O ₃ -Pb(Mg _{1/3} Nb _{2/3})O ₃ -PbTiO ₃
PMN-PZ-PT	Pb(Mg _{1/3} Nb _{2/3})O ₃ - PbZrO ₃ -PbTiO ₃
PYNT	Pb(Yb _{0.5} Nb _{0.5})O ₃ -PbTiO ₃
BSPT	BiScO ₃ -PbTiO ₃
PC-MUT	piezoelectric composite- micromachined ultrasound transducer

HIFU	high intensity focused ultrasound
MPB	morphotropic phase boundary
PPT	polymorphic phase transition
IOP	intraocular pressure
PDMS	polydimethylsiloxane
IPA	isopropyl alcohol
IDT	inter-digital transducers
V_{pp}	peak-to-peak voltage
10, 30, 40, 1T, 2T, 3T, 1R, 2R, 4R	various domain configurations for relaxor-PT crystals

References

1. Carlin, B. Ultrasonics. New York: McGraw-Hill; 1960.
2. Ensminger, D.; Bond, LJ. Ultrasonics: Fundamentals, Technologies, and Applications. New York: CRC Press; 2011.
3. Sherman, CH.; Butler, JL. Transducers and Arrays for underwater sound. New York: Springer; 2007.
4. Narouze, SN. Atlas of ultrasound- guided procedures in interventional pain management. New York: Springer; 2010.
5. Cheeke, JDN. Fundamentals and applications of ultrasonic waves. New York: CRC Press; 2012.
6. Mason WP. Sonics and ultrasonics: early history and applications. IEEE Trans Sonics Ultrason. 1976; SU-23:224–232.
7. Urick, RJ. Principles of underwater sound. CA: Peninsula Publishing; 1996.
8. Graff, K. Historical highlights in ultrasonics-2; IEEE International Ultrasonics, Ferroelectrics and Frequency Control Joint 50th Anniversary Conference; 2004. p. 5-10.
9. Hill CR. Medical ultrasonics: an historical review. British J Radiology. 1973; 46:899–905.
10. Sherlock, NP. PhD Dissertation. PA: The Pennsylvania State University; 2010. Relaxor-PT single crystals for broad bandwidth, high power sonar projectors.
11. Newnham, RE.; Dogan, A. Metal-electroactive Ceramic Composite Transducer. US Patent. 5729077. 1998.
12. Zhang J, Hughes WJ, Bouchilloux P, Meyer RJ Jr, Uchino K, Newnham RE. A class V flexensional transducer: the cymbal. Ultrasonics. 1999; 37:387–393.
13. Newnham RE, Zhang J, Meyer RJ Jr. Cymbal Transducers: A Review. Proceedings of the 2000 12th IEEE International Symposium on Applications of Ferroelectrics. 2000; 1:29–32.
14. Newnham RE, Skinner DP, Cross LE. Connectivity and piezoelectric-pyroelectric composites. Mater Res Bull. 1978; 13:525–536.
15. Newnham RE, Bowen LJ, Klinker KA, Cross LE. Composite piezoelectric transducers. Materials and Design. 1980; 2:93–106.
16. Smith WA, Auld BA. Modeling 1–3 composite piezoelectrics: thickness-mode oscillations. IEEE Trans Ultrason Ferroelectr Freq Contr. 1991; 38:40–47.
17. Akdogan EK, Allahverdi M, Safari A. Piezoelectric composites for sensor and actuator applications. IEEE Trans Ultrason Ferroelectr Freq Contr. 2005; 52:746–775.
18. Chen J, Panda R. Review: commercialization of piezoelectric single crystals for medical imaging applications. IEEE Ultrason Symposium. 2005:235–240.

19. Chen, J.; Panda, R.; Gururaja, TR.; Beck, H. Single crystal thickness and width cuts for enhanced ultrasonic transducer. US Patent. 6465937 B1. 2002.
20. Chen, J.; Panda, R.; Rafter, PG.; Gururaja, TR. Wideband piezoelectric transducer for harmonic imaging. US Patent. 6532819 B1. 2003.
21. Meyer RJ Jr, Montgomery TC, Hughes WJ. Tonpiliz Transducers Designed Using Single Crystal Piezoelectrics. IEEE/MTS Proceedings of Oceans. 2002:2328–2333.
22. Snook KA, Rehrig PW, Hackenberger WS, Jiang X, Meyer RJ Jr, Markley D. Advanced Piezoelectric Single Crystal Based Transducers for Naval Sonar Applications. IEEE Ultrason Symposium. 2005:1065–1068.
23. Wood RW, Loomis AL. The physical and biological effects of high frequency sound waves of great intensity. Phil Mag. 1927; 4(S7):417–436.
24. Mason, WP. Piezoelectric Crystals and their Application to Ultrasonics. New York: Van Nostrand; 1950.
25. Ikeda, T. Fundamentals of piezoelectricity. New York: Oxford University Press; 1990.
26. Cady, WG. Piezoelectricity: An introduction to the theory and applications of electromechanical phenomena in crystals. New York: Dover Publications; 1964.
27. Nye, JF. Physical properties of crystals: their representation by tensors and matrices. New York: Oxford University Press; 1957.
28. Heywang, W.; Lubitz, K.; Wersing, W. Piezoelectricity: Evolution and future of a technology. Berlin: Springer-Verlag; 2008.
29. Safari, A.; Akdogan, EK. Piezoelectric and acoustic materials for transducer applications. New York: Springer; 2008.
30. Jaffe, B.; Cook, WR.; Jaffe, H. Piezoelectric ceramics. New York: Academic Press; 1971.
31. Lines, ME.; Glass, AM. Principles and applications of ferroelectrics and related materials. New York: Oxford University Press; 1977.
32. Xu, YH. Ferroelectric materials and their applications. New York: Elsevier; 1991.
33. Uchino, K. Ferroelectric devices. New York: Marcel Dekker; 1999.
34. Setter, N. Piezoelectric materials in devices. Switzerland: Lausanne; 2002.
35. Curie J, Curie P. Development by pressure of polar electricity in hemihedral crystals with inclined faces. Bull Soc Fr Mineral. 1880; 3:90–102.
36. Valasek J. Piezoelectric and Allied Phenomena in Rochelle Salt. Phys Rev. 1921; 17:475–481.
37. Valasek J. Properties of Rochelle Salt Related to the Piezo-electric Effect. Phys Rev. 1922; 20:639–664.
38. Cross LE, Newnham RE. History of ferroelectrics, Ceramics and Civilization, Vol. III: High technology ceramics- past, present and future. American Ceramic Society. 1987:289–305.
39. Jaffe H. Polymorphism of Rochelle salt. Phys Rev. 1937; 51:43–47.
40. Slater JC. Theory of the transition in KH_2PO_4 . J Chem Phys. 1941; 9:16–33.
41. Mason WP. The elastic, piezoelectric and dielectric constants of ammonium dihydrogen phosphate. Phys Rev. 1946; 69:173–194.
42. Jin L, Li F, Zhang SJ. Decoding the fingerprint of ferroelectric loops: comprehension of the material properties and structures. J Am Ceram Soc. 2014; 97:1–27.
43. Keller AC. Submarine detection by Sonar. Trans AIEE. 1947; 66:1217.
44. Hippel AV, Breckenridge RG, Chesley FG, Tisza L. High dielectric constant ceramics. Ind Eng Chem. 1946; 38:1097–1109.
45. Wul BM, Goldman IM. Dielectric constants of titanates of metals of the second group, C. R. Acad, Sci. USSR. 1945; 46:139–154.
46. Gray, B. Transducer and method of making same. US Patent. 2486560. 1946.
47. Mason WP. Use of temperature and time stabilized barium titanate ceramics in transducers, mechanical wave transmission systems and force measurements. Acustica. 1954; 4:200–202.
48. Bhalla AS, Guo RY, Roy R. The perovskite structure- a review of its role in ceramic science and technology. Mat Res Innovation. 2000; 4:3–26.
49. Ogawa S. On polymorphic change of barium titanate. J Phys Soc Jpn. 1946; 1:32–33.

50. Megaw H. Crystal structure of barium titanate. *Nature*. 1945; 155:484–485.
51. Merz W. Domain properties in BaTiO₃. *Phys Rev*. 1952; 88:421–422.
52. Hippel, A von. Ferroelectricity, Domain Structure, and Phase Transitions of Barium Titanate. *Rev Modern Phys*. 1950; 22:221–237.
53. Cross, LE. Ferroelectric Ceramics: Tailoring Properties for Specific Applications. In: Setter, N.; Colla, EL., editors. *Ferroelectric Ceramics: Tutorial reviews, theory, processing and applications*. Switzerland: Birkhauser Verlag; 1993. p. 1-87.
54. Shirane G, Takeda A. Phase transitions in solid solutions of PbZrO₃ and PbTiO₃. I. Small concentrations of PbTiO₃. *J Phys Soc Jpn*. 1952; 7:5–11.
55. Shirane G, Takeda A. Phase transitions in solid solutions of PbZrO₃ and PbTiO₃. II. X-ray study. *J Phys Soc Jpn*. 1952; 7:12–17.
56. Sawaguchi E. Ferroelectricity vs antiferroelectricity in the solid solution of PbZrO₃:PbTiO₃. *J Phys Soc Jpn*. 1953; 8:615–629.
57. Jaffe B, Roth RS, Marzullo S. Piezoelectric properties of lead zirconate-lead titanate solid solution ceramics. *J Appl Phys*. 1954; 25:809–810.
58. Jaffe B, Roth RS, Marzullo S. Properties of piezoelectric ceramics in the solid solution series lead titanate-lead zirconate oxide- tin oxide and lead titanate-lead hafnate. *J Res Natl Bur Stand*. 1955; 55:239–243.
59. Jaffe H. Titanate ceramics for electromechanical purposes. *Ind Eng Chem*. 1950; 42:264–268.
60. Berlincourt D, Cmolik C, Jaffe H. Piezoelectric properties of polycrystalline lead titanate-lead zirconate compositions. *Proc IRE*. 1960; 48:220–223.
61. Haertling GH. Ferroelectric Ceramics: History and Technology. *J Am Ceram Soc*. 1999; 82:797–818.
62. Jaffe H, Berlincourt DA. Piezoelectric Transducer Materials. *Proc IEEE*. 1965; 53:1372–1386.
63. Carl K, Härdtl KH. Electrical After-effects in Pb(Ti,Zr)O₃ Ceramics. *Ferroelectrics*. 1978; 17:473–486.
64. Robels U, Arlt G. Domain Wall Clamping in Ferroelectrics by Orientation of Defects. *J Appl Phys*. 1993; 73:3454–3460.
65. Härdtl KH. Electrical and mechanical losses in ferroelectric ceramics. *Ceram Inter*. 1982; 8:121–127.
66. Uchino K, Zheng JH, Chen YH, Du XH, Ryu J, Gao Y, et al. Loss mechanisms and high power piezoelectrics. *J Mater Sci*. 2006; 41:217–228.
67. Carl K, Härdtl KH. Electrical after-effects in Pb(Ti,Zr)O₃ ceramics. *Ferroelectrics*. 1978; 17:473–486.
68. Gallego-Juarez JA. Piezoelectric ceramics and ultrasonic transducers. *J Phys E: Sci Instrum*. 1989; 22:814–816.
69. Cross, LE. Ferroic materials and composites: past, present and future. In: Somiya, S., editor. *Advanced Ceramics III*. New York: Elsevier; 1990. p. 71-102.
70. Berlincourt, D. Piezoelectric Crystals and Ceramics. In: Mattiat, OE., editor. Chapter 2 in *Ultrasonic Transducer Materials*. New York: Plenum Press; 1971.
71. Berlincourt, DA.; Curran, DR.; Jaffe, H. Chapter 3 in *Physical acoustics: principle and methods*. New York: Academic Press; 1964. Piezoelectric and piezomagnetic materials and their function in transducers.
72. Goodman G. Ferroelectric Properties of Lead Metaniobate. *J Am Ceram Soc*. 1953; 36:368–372.
73. Francombe MH. Polymorphism in lead metaniobate. *Acta Crystallogr*. 1956; 9:683–684.
74. Lewis B, Thomas LA. Piezoelectric ceramics based on PbNb₂O₆. *Proc. Intl Conf Solid State Phys Electron Telocommun Brussels*. 1958; 4:883–885.
75. Rybjanets AN, Razumovskaja ON, Reznitchenko LA, Komarov VD, Turik AV. Lead titanate and lead metaniobate porous ferroelectric ceramics. *Integr Ferroelectr*. 2004; 63:197–200.
76. Venet M, Zabotto FL, Eiras JA, Garcia D. Improvement of the phase diagram for the pseudobinary PbNb₂O₆-BaNb₂O₆ system. *J Appl Phys*. 2009; 105:124106.

77. Volk, T.; Wohlecke, M. Lithium niobate, Defect, photorefraction and ferroelectric switching. Berlin: Springer-Verlag; 2008.
78. Shur, VY. Lithium niobate and lithium tantalite-based piezoelectric materials, Chapter 6, Advanced Piezoelectric Materials: Science and technology. Uchino, K., editor. New York: Woodhead Publishing, CRC Press; 2010.
79. Yamada T, Niizeki N, Toyoda H. Piezoelectric and elastic properties of lithium niobate single crystals. *Jpn J Appl Phys.* 1967; 6:151–155.
80. Matthias BT, Remeika JP. Ferroelectricity in the ilmenite structure. *Phys Rev.* 1949; 76:1886–1887.
81. Schweinler HC. Ferroelectricity in the ilmenite structure. *Phys Rev.* 152(87):5–11.
82. Smith RT, Welsh FS. Temperature dependence of the elastic, piezoelectric, and dielectric constant of lithium tantalite and lithium niobate. *J Appl Phys.* 1971; 42:2219–2230.
83. Weis RS, Gaylord TK. Lithium niobate: summary of physical properties and crystal structure. *Appl Phys A.* 1985; 37:191–203.
84. Kirk KJ, Scheit CW, Schmarje N. High temperature acoustic emission tests using lithium niobate piezocomposite transducers. *Insight.* 2007; 49:142–145.
85. Kirk KJ, McNab A, Cochran A, Hall I, Hayward G. Ultrasonic arrays for monitoring cracks in an industrial plant at high temperatures. *IEEE Trans Ultrason Ferroelectr Freq Contr.* 1999; 46:311–319.
86. Baba A, Searfass CT, Tittmann BR. High temperature ultrasonic transducer up to 1000°C using lithium niobate single crystal. *Appl Phys Lett.* 2010; 97:232901.
87. Cannata JM, Ritter TA, Chen WH, Silverman RH, Shung KK. Design of efficient, broadband single element (20–80MHz) ultrasonic transducers for medical imaging applications. *IEEE Trans Ultrason Ferroelectr Freq Contr.* 2003; 50:1548–1557.
88. Zhou QF, Cannata JM, Guo HK, Huang CZ, Marmarelis VZ, Shung KK. Half-thickness inversion layer high frequency ultrasonic transducers using LiNbO₃ single crystal. *IEEE Trans Ultrason. Ferroelectr Freq Contr.* 2005; 52:127–133.
89. Dang ZM, Yuan JK, Zha JW, Zhou T, Li ST, Hu GH. Fundamentals, processes and applications of high permittivity polymer-matrix composites. *Prog. Mater. Sci.* 2012; 57:660–723.
90. Shen ZY, Li JF, Chen RM, Zhou QF, Shung KK. Microscale 1–3 type (Na,K)NbO₃ based Pb-free piezocomposites for high frequency ultrasonic transducer applications. *J. Am. Ceram. Soc.* 2011; 94:1346–1349. [PubMed: 21637726]
91. Shen ZY, Xu Y, Li JF. Fabrication and electromechanical properties of microscale 1–3 type piezoelectric composites using (Na,K)NbO₃ based Pb-free piezoceramics. *J. Appl. Phys.* 2009; 105:104103.
92. Gururaja TR, Schulze WA, Cross LE, Newnham RE, Auld BA, Wang YZ. Piezoelectric composite materials for ultrasonic transducer applications. Part I: resonant modes of vibration of PZT rod-polymer composites. *IEEE Trans Sonics Ultrason.* 1985; SU32:481–498.
93. Newnham RE, Safari A, Giniewicz J, Fox BH. Composite piezoelectric sensors. 1984; 60:15–21.
94. Klicker KA, Biggers JV, Newnham RE. Composites of PZT and epoxy for hydrostatic transducer applications. *J Am Ceram Soc.* 1981; 64:5–9.
95. Gibson RF. A review of recent research on mechanics of multifunctional composite materials and structures. *Compos Struct.* 2010; 92:2793–2810.
96. Uchino, K. Piezoelectric composite materials. In: Uchino, K., editor. Chapter 9, Advanced Piezoelectric Materials: Science and technology. New York: Woodhead Publishing, CRC Press; 2010.
97. Zhang QM, Chen J, Wang H, Zhao J, Cross LE. A new transverse piezoelectric mode 2-2 piezocomposite for underwater transducer applications. *IEEE Trans Ultrason Ferroelectr Freq Contr.* 1995; 42:774–781.
98. Geng XC, Zhang QM. Evaluation of piezocomposites for ultrasonic transducer applications-influence of the unit cell dimensions and the properties of constituents on the performance of 2-2 piezocomposites. *IEEE Trans Ultrason Ferroelectr Freq Contr.* 1997; 44:857–872.

99. Li LL, Zhang SJ, Xu Z, Geng XC, Wen F, Luo J, ShROUT TR. Hydrostatic piezoelectric properties of [011] poled PMN-PT single crystals and 2-2 lamellar composites. *Appl Phys Lett*. 2014; 104:032909. [PubMed: 24753619]
100. Smith WA. Modeling 1–3 composite piezoelectrics: Hydrostatic response. *IEEE Trans Ultrason Ferroelectr Freq Contr*. 1993; 40:41–49.
101. Li L, Sottos NR. Improving hydrostatic performance of 1–3 piezocomposites. *J Appl Phys*. 1995; 77:4595–4603.
102. Safari A, Halliyal A, Bowen LJ, Newnham RE. Flexible composite transducers. *J Am Ceram Soc*. 1982; 65:207–209.
103. Jiang X, Yuan JR, Cheng A, Cao P, Snook K, Hackenberger W. Microfabrication of piezoelectric composite ultrasound transducers (PC-MUT). 2006 IEEE Ultrasonics Symposium. 2006:922–925.
104. Smith WA. New opportunities in ultrasonic transducers emerging from innovations in piezoelectric materials. *Proc. SPIE*. 1992; 1733:3–26.
105. Cao WW, Zhang QM, Zhao JZ, Cross LE. Effects of face plates on surface displacement profile in 2-2 piezoelectric composites. *IEEE Trans Ultrason Ferroelectr Freq Contr*. 1995; 42:37–41.
106. Geng X, Zhang QM. Resonance modes and losses in 1–3 piezocomposites for ultrasonic transducer applications. *J Appl Phys*. 1999; 85:1342–1350.
107. Topolov VY, Krivoruchko AV, Bowen CR, Panich AA. Hydrostatic Piezoelectric Coefficients of the 2–2 Composite Based on [011]-poled 0.71 PMN-0.29 PT Single Crystal. *Ferroelectrics*. 2010; 400:410–416.
108. Topolov VY, Bowen CR, Krivoruchko AV. Role of domain orientations in forming the hydrostatic performance of novel 2-2 single crystal/polymer composites. *Ferroelectrics*. 2013; 444:84–99.
109. Topolov, VY.; Bowen, CR. *Electromechanical properties in composites based on ferroelectrics*. London: Springer; 2009.
110. Smith W, Shaulov A, Auld B. Design of piezocomposites for ultrasonic transducers. *Ferroelectrics*. 1989; 91:155–162.
111. Cross LE. Relaxor Ferroelectrics. *Ferroelectrics*. 1987; 76:241–267.
112. Samara GA. The Relaxational Properties of Compositionally Disordered ABO₃ Perovskites. *J Phys: Condens Matter*. 2003; 15:R367–R411.
113. Ye ZG. Relaxor Ferroelectric Complex Perovskites: Structure, Properties and Phase Transitions. *Key Eng. Mater*. 1998:155–156. 81–122.
114. Ye ZG. Relaxor ferroelectric PMN: Properties and present understanding. *Ferroelectrics*. 1996; 184:193–208.
115. Bokov AA, Ye ZG. Recent progress in relaxor ferroelectrics with perovskite structure. *J Mater Sci*. 2006; 41:31–52.
116. Samara GA. The Relaxational Properties of Compositionally Disordered ABO₃ Perovskites. *J Phys: Condens Matter*. 2003; 15:R367–R411.
117. Cowley RA, Gvasaliya SN, Lushnikov SG, Roessli B, Rotaru GM. Relaxing with relaxors: a review of relaxor ferroelectrics. *Adv Phys*. 2011; 60:229–327.
118. Smolenskii GA, Isupov VA, Agranovskaya AI, Krainik NN. New Ferroelectrics of Complex Composition. IV. *Sov Phys-Solid State*. 1961; 2:2651–2654.
119. Damjanovic D, Newnham. Electrostrictive and piezoelectric materials for actuator applications. *J. Intell. Mater. Syst. Struct*. 1992; 3:190–208.
120. Herbert, JM. *Electrocomponent science monographs*. Vol. 3. New York: Gordon and Breach; 1982. *Ferroelectric transducers and sensors*.
121. Uchino K, Nomura S, Cross LE, Newnham RE, Jang SJ. Review: Electrostrictive effect in perovskites and its transducer applications. *J. Mater. Sci*. 1981; 16:569–578.
122. Chen J, Shurland A, Perry J, Ossmann B, Gururaja TR. Electrostrictive transducers for medical ultrasonic applications. *IEEE IUSS*. 1996:27–30.
123. Sherrit S, Mukherjee BK. Electrostrictive materials: characterization and applications for ultrasound. *SPIE*. 3341:196–207.

124. Rittenmyer KM. Electrostrictive ceramics for underwater transducer applications. *J. Acoust. Soc. Am.* 1994; 95:849–856.
125. Newnham, RE. Tunable transducers: nonlinear phenomena in electroceramics. National Institute of Standards and Technology Special Publication 804, Chemistry of electronic ceramic materials; Proceedings of the International Conference held in Jackson; August 17–22, 1990; WY.
126. Alberta, EF. PhD Dissertation. PA: The Pennsylvania State University; 2003. Relaxor based solid solutions for piezoelectric and electrostrictive applications.
127. Tang H, Zhang M, Zhang S, Feng YJ, Li F, Shrout TR. Investigation of dielectric and piezoelectric properties in $\text{Pb}(\text{Ni},\text{Nb})\text{O}_3\text{-PbHfO}_3\text{-PbTiO}_3$ ternary system. *J Euro Ceram Soc.* 2013; 33:2491–2497.
128. Wang HF, Jiang B, Shrout TR, Cao WW. Electromechanical properties of fine-grain 0.7PMN-0.3PT ceramics. *IEEE Trans Ultrason Ferroelectr Freq Control.* 2004; 51:908–912. [PubMed: 15301011]
129. Tang H, Zhang S, Feng YJ, Shrout TR. Piezoelectric property and strain behavior of PYN-PH-PT polycrystalline ceramics. *J Am Ceram Soc.* 2013; 96:2857–2863.
130. Alberta EF, Bhalla AS. Piezoelectric and dielectric properties of transparent PNN-PZT ceramics. *Inter J Inorgan Mater.* 2001; 3:987–995.
131. Hao H, Zhang S, Shrout TR. Dielectric and piezoelectric properties of MPB composition in the (0.8-x)PMT-0.2PZ-xPT ternary system. *J Am Ceram Soc.* 2008; 91:2232–2235.
132. Wang DW, Cao MS, Zhang S. Investigation of ternary system $\text{PbSnO}_3\text{-PMN-PT}$ with morphotropic phase boundary compositions. *J Euro Ceram Soc.* 2012; 32:441–448.
133. Wang DW, Cao MS, Zhang S. Phase diagram and properties of PIN-PMN-PT polycrystalline ceramics. *J Euro Ceram Soc.* 2012; 32:433–439.
134. Hao H, Zhang S, Shrout TR. Dielectric, piezoelectric and electromechanical properties for MPB compositions in the PMT-PZ-PT ternary system. *J Appl Phys.* 2009; 105:024104.
135. Alberta EF, Bhalla AS. Investigation of the lead indium niobate-lead magnesium niobate solid solution. *Mater Lett.* 1999; 40:114–117.
136. Wang DW, Cao MS, Zhang S. Investigation of ternary system $\text{PbHfO}_3\text{-PbTiO}_3\text{-Pb}(\text{Mg}_{1/3}\text{Nb}_{2/3})\text{O}_3$ with morphotropic phase boundary compositions. *J Am Ceram Soc.* 2012; 95:3220–3228.
137. Kuwata J, Uchino K, Nomura S. Phase Transitions in the $\text{Pb}(\text{Zn}_{1/3}\text{Nb}_{2/3})\text{O}_3\text{-PbTiO}_3$ System. *Ferroelectrics.* 1981; 37:579–582.
138. Kuwata J, Uchino K, Nomura S. Dielectric and Piezoelectric Properties of $0.91\text{Pb}(\text{Zn}_{1/3}\text{Nb}_{2/3})\text{O}_3\text{-}0.09\text{PbTiO}_3$ Single Crystals. *Jpn J Appl Phys.* 1982; 21:1298–1302.
139. Park SE, Shrout TR. Ultrahigh Strain and Piezoelectric Behavior in Relaxor Based Ferroelectric Single Crystals. *J Appl Phys.* 1997; 82:1804–1811.
140. Park SE, Shrout TR. Relaxor Based Ferroelectric Single Crystals for Electro-mechanical Actuators. *Mater Res Innovations.* 1997; 1:20–25.
141. Zhang SJ, Li F. High performance ferroelectric relaxor-PT single crystals: status and perspective. *J Appl Phys.* 2012; 111:031301.
142. Park SE, Hackenberger W. High performance single crystal piezoelectrics: applications and issues. *Curr Opin Solid State Mater Sci.* 2002; 6:11–18.
143. Yamashita Y, Hosono Y, Harada K, Yasuda N. Present and future of piezoelectric single crystals and the importance of B-site cations for high piezoelectric response. *IEEE Trans Ultrason Ferroelectr Freq Control.* 2002; 49:184–192. [PubMed: 11885676]
144. Luo NN, Li YY, Xia ZG, Li Q. Progress in lead based ferroelectric and antiferroelectric single crystals: composition modification, crystal growth and properties. *CrystEngComm.* 2012; 14:4547–4556.
145. Ye ZG. Crystal chemistry and domain structure of relaxor piezocrystals. *Curr Opin Solid State Mater Sci.* 2002; 6:35–44.
146. Zhang S, Randall C, Shrout TR. Recent Developments in High Curie Temperature Perovskite Single Crystals. *IEEE Trans Ultrason Ferroelectr Freq Contr.* 2005; 52:564–569.

147. Li XB, Luo HS. The growth and properties of relaxor-based ferroelectric single crystals. *J Am Ceram Soc.* 2010; 93:2915–2928.
148. Sun EW, Cao WW. Relaxor based ferroelectric single crystals: growth, domain engineering, characterization and applications. *Prog Mater Sci.* 2014; 65:124–210. [PubMed: 25061239]
149. Davis M. Picturing the elephant: giant piezoelectric activity and the monoclinic phases of relaxor ferroelectric single crystals. *J Electroceram.* 2007; 19:23–45.
150. Zhang SJ, Li F, Sherlock NP, Luo J, Lee HJ, Xia R, et al. Recent developments on high Curie temperature PIN-PMN-PT ferroelectric crystals. *J Cryst Growth.* 2011; 318:846–850.
151. Luo J, Zhang SJ. Advances in the growth and characterization of relaxor-PT based ferroelectric single crystals. *Crystals.* 2014; 4:306–330.
152. Zhou QF, Lam KH, Zheng HR, Qiu WB, Shung KK. Piezoelectric single crystal ultrasonic transducers for biomedical applications. *Prog Mater Sci.* 2014; 66:87–111. [PubMed: 25386032]
153. Chen Y, Lam K, Zhou D, Yue Q, Yu Y, Wu J, Qiu W, Sun L, Zhang C, Luo H, Chan H, Dai JY. High performance relaxor-based ferroelectric single crystals for ultrasonic transducer applications. *Sensors.* 2014; 14
154. Jiang XN, Kim JW, Kim KR. Relaxor-PT single crystal piezoelectric sensors. *Crystals.* 2014; 4
155. Shrout TR, Chang ZP, Kim N, Markgraf S. Dielectric behavior of single crystal near the (1-x)Pb(Mg_{1/3}Nb_{2/3})O₃-xPbTiO₃ morphotropic phase boundary. *Ferroelectr Lett.* 1990; 12:63–69.
156. Ye ZG, Tissot P, Schmid H. Pseudo-binary Pb(Mg_{1/3}Nb_{2/3})O₃-PbTiO₃ phase diagram and crystal growth of Pb(Mg_{1/3}Nb_{2/3})O₃. *Mater Res Bull.* 1990; 25:739–748.
157. Park SE, Shrout TR. Characteristics of relaxor-based piezoelectric single crystals for ultrasonic transducers. *IEEE Trans Ultrason Ferroelectr Freq Contr.* 1997; 44:1140–1147.
158. Fu H, Cohen RE. Polarization rotation mechanism of ultrahigh electromechanical response in single-crystal piezoelectrics. *Nature.* 2000; 403:281–283. [PubMed: 10659840]
159. Service RF. Materials science shape-changing crystals get shiftier. *Science.* 1997; 275:1878.
160. Zhang R, Jiang B, Jiang WH, Cao WW. Anisotropy in domain engineered 0.92Pb(Zn_{1/3}Nb_{2/3})O₃-0.08PbTiO₃ single crystal and analysis of its property fluctuations. *IEEE Trans Ultrason Ferroelectr Freq Contr.* 2002; 49:1622–1627.
161. Zhang R, Jiang B, Cao WW. Elastic, piezoelectric, and dielectric property of multidomain 0.67Pb(Mg_{1/3}Nb_{2/3})O₃-0.33PbTiO₃ single crystals. *J Appl Phys.* 2001; 90:3471–3475.
162. Zhang R, Jiang B, Cao WW. Single domain properties of 0.67PMN-0.33PT single crystals under electric field bias. *Appl Phys Lett.* 2003; 82:787–789.
163. Zhang S, Laurent L, Jeong D, Zhang QM, Randall CA, Shrout TR. Growth and characterization of Fe-doped Pb(Zn_{1/3}Nb_{2/3})O₃-PbTiO₃ single crystals. *J Appl Phys.* 2003; 93:9257.
164. Liu S, Ren W, Mukherjee BK, Zhang SJ, Shrout TR, Rehrig P, et al. The piezoelectric shear strain coefficient of <111> oriented Pb(Zn_{1/3}Nb_{2/3})O₃-PbTiO₃ piezocrystals. *Appl Phys Lett.* 2003; 83:2886–2888.
165. Hlinka J, Kamba S, Petzelt J, Kulda J, Randall CA, Zhang SJ. Origin of “waterfall” effect in phonon dispersion of relaxor of perovskites. *Phys Rev Lett.* 2003; 91:107602. [PubMed: 14525505]
166. Zhang S, Lebrun L, Randall CA, Shrout TR. Growth and electric properties of (Mn,F)-codoped 0.92Pb(Zn_{1/3}Nb_{2/3})O₃-0.08PbTiO₃ single crystals. *J Cryst Growth.* 2004; 267:204–212.
167. Hana P, Burianova L, Furman E, Zhang SJ, Shrout TR, Cross LE. Effect of electric field on hydrostatic piezoelectric coefficients of single domain PZN-PT crystals. *Integr Ferroelectr.* 2004; 63:63–71.
168. Jeong D, Zhang SJ, Hwang HB. Dependence of domain stability on the thickness of tetragonal 0.88Pb(Zn_{1/3}Nb_{2/3})O₃-0.12PbTiO₃ single crystal. *J Korean Phys Soc.* 2004; 44:1531–1534.
169. Zhang S, Lebrun L, Randall C, Shrout TR. Orientation dependence properties of modified 0.88Pb(Zn_{1/3}Nb_{2/3})O₃-0.12PbTiO₃ single crystals. *Phys Stat Sol (a).* 2005; 202:151–157.
170. Shanthi M, Hoe KH, Lim CYH, Lim LC. Overpoling-induced property degradation in Pb(Mg_{1/3}Nb_{2/3})O₃-PbTiO₃ single crystals of near-morphotropic phase boundary compositions. *Appl Phys Lett.* 2005; 86:262908.

171. Zhang SJ, Luo J, Xia R, Rehrig PW, Randall CA, Shrout TR. Field-induced piezoelectric response in $\text{Pb}(\text{Mg}_{1/3}\text{Nb}_{2/3})\text{O}_3\text{-PbTiO}_3$ single crystals. *Solid State Commun.* 137:16–20. 3006.
172. Zhang S, Laurent L, Liu S, Rhee S, Randall CA, Shrout TR. Piezoelectric shear coefficient of $\text{Pb}(\text{Zn}_{1/3}\text{Nb}_{2/3})\text{O}_3\text{-PbTiO}_3$ single crystals. *Jpn J Appl Phys.* 2002; 41:L1099–L1102.
173. Davis M, Damjanovic D, Setter N. Electric-field-, temperature-, and stress induced phase transitions in relaxor ferroelectric single crystals. *Phys Rev B.* 2006; 73:014115.
174. Dammak H, Renault A, Gaucher P, Thi M, Calvarin G. Origin of the giant piezoelectric properties in the [001] domain engineered relaxor single crystals. *Jpn J Appl Phys.* 2003; 42:6477–6482.
175. Ye ZG. High performance piezoelectric single crystals of complex perovskite solid solutions. *MRS Bull.* 2009; 34:277–283.
176. Davis, M. Ph.D. dissertation. Lausanne, Switzerland: Swiss Federal Institute of Technology-EPFL; 2006. Phase transition, anisotropy and domain engineering: The Piezoelectric Properties of Relaxor-ferroelectric Single Crystals.
177. Davis M, Damjanovic D, Setter N. Electric field, temperature and stress induced phase transitions in relaxor ferroelectric single crystals. *Phys Rev B.* 2006; 73:014115.
178. Damjanovic D, Budimir M, Davis M, Setter N. Monodomain versus polydomain piezoelectric response of 0.67PMN-0.33PT single crystals along nonpolar directions. *Appl Phys Lett.* 2003; 83:527–529.
179. Damjanovic D, Budimir M, Davis M, Setter N. Piezoelectric anisotropy: Enhanced piezoelectric response along nonpolar directions in perovskite crystals. *J Mater Sci.* 2006; 41:65–76.
180. Davis M, Budimir M, Damjanovic D, Setter N. Rotator and extender ferroelectrics: importance of the shear coefficient to the piezoelectric properties of domain engineered crystals and ceramics. *J Appl Phys.* 2007; 101:054112.
181. Davis M, Damjanovic D, Hayem D, Setter N. Domain engineering of the transverse piezoelectric coefficient in perovskite ferroelectrics. *J Appl Phys.* 2005; 98:014102.
182. Davis M, Damjanovic D, Setter N. Temperature dependence of the direct piezoelectric effect in relaxor-ferroelectric single crystals: intrinsic and extrinsic contributions. *J Appl Phys.* 2006; 100:084103.
183. Davis M, Damjanovic D, Setter N. Direct piezoelectric effect in relaxor-ferroelectric single crystals. *J Appl Phys.* 2004; 95:5679–5684.
184. Hajjaji A, Pruvost S, Sebald G, Lebrun L, Guyomar D, Benkhoucha K. Mechanism of depolarization with temperature for <001> PZN-PT single crystals. *Acta Materialia.* 2009; 57:2243–2249.
185. Kobor D, Guiffard B, Lebrun L, Hajjaji A, Guyomar D. Oxygen vacancies effect on ionic conductivity and relaxation phenomenon in undoped and Mn doped PZN-4.5PT single crystals. *J Phys D: Appl Phys.* 2007; 40:2920–2926.
186. Kobor D, Tine M, Hajjaji A, Lebrun L, Pruvost S, Guyomar D. Comparative characterization of rhombohedral and tetragonal PZN-PT single crystals. *AIP Advances.* 2011; 1:022133.
187. Benayad A, Sebald G, Lebrun L, Guiffard B, Pruvost S, Guyomar D, Beylat L. Segregation study and segregation modeling of Ti in PMN-PT single crystal grown by Bridgman method. *Mater Res Bull.* 2006; 41:1069–1076.
188. Tikhomirov O, Labardi M, Ascoli C, Allegrini M, Lebrun L. Imaging of ferroelectric polarization in PMN-PT crystals by scanning electro-optic microscopy. *Appl Phys Lett.* 2006; 88:152910.
189. Lu Y, Jeong DY, Cheng ZY, Zhang QM, Luo HS, Yin ZW, Viehland D. Phase transitional behavior and piezoelectric properties of the orthorhombic phase of PMN-PT single crystals. *Appl Phys Lett.* 2001; 78:3109–3111.
190. Oakley CG, Zippo MJ. Single crystal piezoelectrics: a revolutionary development for transducers. 2000 IEEE Ultrasonics Symposium. :1157–1167.
191. Colla EV, Yushin NK, Viehland D. Dielectric properties of PMN-PT single crystals for various electrical and thermal history. *J Appl Phys.* 1998; 83:3298–3304.
192. Bai FM, Wang NG, Li JF, Viehland D, Gehring PM, Xu GY, Shirane G. X-ray and neutron diffraction investigations of the structural phase transformation sequence under electric field in 0.7PMN-0.3PT crystal. *J Appl Phys.* 2004; 96:1620–1627.

193. Viehland D, Amin A, Li JF. Piezoelectric instability in $\langle 011 \rangle$ oriented $\text{Pb}(\text{BI}_{1/3}\text{BII}_{2/3})\text{O}_3$ -PT crystals. *Appl Phys Lett*. 2001; 79:1006–1008.
194. Tian J, Han PD, Payne DA. Measurements along the growth direction of PMN-PT crystals: dielectric, piezoelectric and elastic properties. *IEEE Trans Ultrason Ferroelectr Freq Contr*. 2007; 54:1895–1902.
195. Priya S, Uchino K. Dielectric and piezoelectric properties of the Mn-substituted PZN-PT single crystal. *J Appl Phys*. 2002; 91:4515–4520.
196. Priya S, Uchino K, Viehland D. Fe- substituted 0.92PZN-0.08PT single crystals: A “hard” piezocrystal. *Appl Phys Lett*. 2002; 81:2430–2432.
197. Priya S, Viehland D, Uchino K. Importance of structural irregularity on dielectric loss in PMN-PT crystals. *Appl Phys Lett*. 2002; 80:4217–4219.
198. Lin DB, Lee HJ, Zhang SJ, Li F, Li ZR, Xu Z, Shrout TR. Influence of domain size on the scaling effects in PMN-PT ferroelectric crystals. *Scripta Mater*. 2011; 64:1149–1151.
199. Priya S, Ryu J, Uchino K, Viehland D. Mechanical aging behavior of oriented PMN-PT and PZN-PT single crystals. *Appl Phys Lett*. 2001; 79:2624–2626.
200. Priya S, Kim HW, Ryu J, Zhang SJ, Shrout TR, Uchino K. Modeling of fatigue behavior in relaxor piezocrystals: improved characteristics by Mn substitution. *J Appl Phys*. 2002; 92:3923–3927.
201. Chabok HR, Zhou QF, Alagha S, Tian J, Han PD, Shung KK. Thickness dependent characteristics of high permittivity PMN-0.32PT single crystal for high frequency medical imaging. *Ferroelectrics*. 2011; 422:70–76. [PubMed: 22162876]
202. Chang WY, Huang WB, Bagal A, Chang CH, Tian J, Han PD, Jiang XN. Study on dielectric and piezoelectric properties of 0.7PMN-0.3PT single crystal with nano-patterned composite electrode. *J Appl Phys*. 2013; 114:114103. [PubMed: 24170960]
203. Lim CL, Rajan KK. High homogeneity high performance flux grown PZN-PT single crystals. *J Cryst Growth*. 2004; 271:435–444.
204. Rajan KK, Shanthi M, Chang WS, Jin J, Lim LC. Dielectric and piezoelectric properties of [001] and [011] poled relaxor ferroelectric PZN-PT and PMN-PT single crystals. *Sens Actua A: Phys*. 2007; 133:110–116.
205. Lim LC, Shanthi M, Rajan KK, Lim CYH. Flux growth of high homogeneity PMN-PT single crystals and their property characterization. *J Cryst Growth*. 2005; 282:330–342.
206. Jin J, Rajan KK, Lim LC. Properties of single domain PZN-PT single crystal. *Jpn J Appl Phys*. 2006; 45:8744–8747.
207. Luo HS, Xu GS, Xu HQ, Wang PC, Yin ZW. Compositional homogeneity and electrical properties of lead magnesium niobate titanate single crystals grown by a modified Bridgman technique. *Jpn J Appl Phys*. 2000; 39:5581–5585.
208. Xu GS, Luo HS, Xu HQ, Yin ZW. Third ferroelectric phase in PMNT single crystals near the morphotropic phase boundary composition. *Phys Rev B*. 2001; 64:020102.
209. Peng J, Luo HS, Lin D, Xu HQ, He TH, Jin WQ. Orientation dependence of transverse piezoelectric properties of 0.7PMN-0.3PT single crystals. *Appl Phys Lett*. 2004; 85:6221–6223.
210. Xu GS, Luo HS, Guo YP, Gao YQ, Xu HQ, Qi ZY, Zhong WZ, Yin ZW. Growth and piezoelectric properties of PMN-PT crystals by the modified Bridgman technique. *Solid State Commun*. 2001; 120:321–324.
211. Guo YP, Luo HS, Chen KP, Xu HQ, Zhang XW, Yin ZW. Effect of composition and poling field on the properties and ferroelectric phase stability of PMN-PT crystals. *J Appl Phys*. 2002; 92:6134–6138.
212. Luo LH, Dietze M, Solterbeck CH, Luo HS, Es-Souni M. Tuning the functional properties of PMN-PT single crystals via doping and thermoelectrical treatments. *J Appl Phys*. 2013; 114:224112.
213. Wang HX, Xu HG, Luo HS, Yin ZW, Bokov AA, Ye ZG. Dielectric anomalies of the relaxor-based 0.9PMN-0.1PT single crystals. *Appl Phys Lett*. 2005; 87:012904.
214. Amin A, Cross LE, Lee HY. Evolution of a nonspontaneous, high piezoelectric coupling symmetry axis in relaxor ferroelectric single crystals. *J Appl Phys*. 2007; 101:114103.

215. Rajapurkar A, Ural SO, Zhuang YA, Lee HY, Amin A, Uchino K. Piezoelectric loss performance in PMN-PT single crystals. *Jpn J Appl Phys.* 2010; 49:071502.
216. Zhuang Y, Ural SO, Gosain R, Tuncdemir S, Amin A, Uchino K. High power piezoelectric transformers with PMN-PT single crystals. *Appl Phys Exp.* 2009; 2:121402.
217. McLaughlin EA, Liu TQ, Lynch CS. Relaxor ferroelectric PMN-32%PT crystals under stress, elastic field and temperature loading: II-33-mode measurements. *Acta Mater.* 2005; 53:4001–4008.
218. Noheda B, Cox DE, Shirane G, Park SE, Cross LE, Zhong Z. Polarization rotation via a monoclinic phase in the piezoelectric 92%PZN-8%PT. *Phys Rev Lett.* 2001; 86:3891–3894. [PubMed: 11329350]
219. Hlinka J, Kamba S, Petzelt J, Kulda J, Randall CA, Zhang S. Diffuse scattering in $\text{Pb}(\text{Zn}_{1/3}\text{Nb}_{2/3})\text{O}_3$ with 8% PbTiO_3 by quasi-elastic neutron scattering. *J Phys: Condens Matter.* 2003; 15:4249–4257.
220. Okawara C, Amin A. dc field effect on stability of piezoelectric PZN-0.06PT single crystals under compressive stress. *Appl Phys Lett.* 2009; 95:072902.
221. Viehland D. Effect of uniaxial stress upon the electromechanical properties of various piezoelectric ceramics and single crystals. *J. Am Ceram Soc.* 2006; 89:775–785.
222. Liu T, Lynch CS. Ferroelectric properties of [110], [001] and [111] poled relaxor single crystals: measurements and modeling. *Acta Mater.* 2003; 51:407–416.
223. Liu, TQ. PhD dissertation. Georgia Institute of Technology; 2004. Electromechanical behavior of relaxor ferroelectric crystals.
224. Webber, KG. PhD dissertation. Georgia Institute of Technology; 2008. Effect of domain wall motion and phase transformations on nonlinear hysteretic constitutive behavior in ferroelectric materials.
225. Li, F. PhD dissertation. Xi'an Jiaotong University; 2012. Piezoelectric behaviors of relaxor-PT ferroelectric crystals: mechanisms and characterization.
226. McLaughlin EA, Liu T, Lynch CS. Relaxor ferroelectric PMN-32%PT crystals under stress and electric field loading: I-32 mode measurements. *Acta Mater.* 2004; 52:3849–3857.
227. Wada S, Park SE, Cross LE, Shrout TR. Engineered domain configuration in rhombohedral PZN-PT single crystals and their ferroelectric related properties. *Ferroelectrics.* 1999; 221:147–145.
228. Oates WS, Lynch CS, Njiwa ABK, Lupascu DC. Anisotropic fracture behavior in ferroelectric relaxor PZN-4.5%PT single crystals. *J Am Ceram Soc.* 2005; 88:1838–1844.
229. Wang LH, Xu Z, Li ZR, Li F. Bridgman growth and thermal analysis of PMN-PT single crystals. *Mater Sci Eng B.* 2010; 170:113–116.
230. Luo J, Rehrig P, Hackenberger W. Bridgman growth of large size and compositionally uniform relaxor ferroelectric PMN-PT crystals. *IEEE ISAF.* 2006:257–260.
231. Zhao XY, Fang B, Cao H, Guo Y, Luo HS. Dielectric and piezoelectric performance of PMN–PT single crystals with compositions around the MPB: influence of composition, poling field and crystal orientation. *Mater Sci Eng B.* 2002; 96:254–262.
232. Webber KG, Robinson HC, Rossetti GA, Lynch CS. A distributed step like switching model of the continuous field driven phase transformations observed in PMN-xPT relaxor ferroelectric single crystals. *Acta Mater.* 2008; 56:2744–2749.
233. Liu G, Jiang WH, Zhu JQ, Cao WW. Electromechanical properties and anisotropy of single- and multi- domain 0.72PMN-0.28PT single crystals. *Appl Phys Lett.* 2011; 99:162901. [PubMed: 22087049]
234. Xian Y, Zhang R, Cao W. Orientation dependence of electromechanical properties of relaxor based ferroelectric single crystals. *J Mater Sci.* 2011; 46:63–68. [PubMed: 25214674]
235. Xiang Y, Zhang R, Cao W. Optimization of piezoelectric properties for [001]c poled $0.94\text{Pb}(\text{Zn}_{1/3}\text{Nb}_{2/3})\text{O}_3-0.06\text{PbTiO}_3$ single crystals. *Appl Phys Lett.* 2010; 96:092902.
236. Wang Z, Zhang R, Sun E, Cao WW. Contributions of domain wall motion to complex electromechanical coefficients of $0.62\text{Pb}(\text{Mg}_{1/3}\text{Nb}_{2/3})\text{O}_3-0.38\text{PbTiO}_3$ crystals. *J Appl Phys.* 2010; 107:014110.

237. Wu T, Zhao P, Bao MQ, Bur A, Hockel JL, Wong K, et al. Domain engineered switchable strain states in ferroelectric (011) PMN-PT single crystals. *J Appl Phys.* 2011; 109:124101.
238. Yamashita Y, Harada K. Crystal growth and electrical property of lead scandium niobate-lead titanate binary single crystals. *Jpn J Appl Phys.* 1997; 36:6039–6042.
239. Bing YH, Ye ZG. Effects of chemical compositions on the growth of relaxor ferroelectric $\text{Pb}(\text{Sc}_{1/2}\text{Nb}_{1/2})_{1-x}\text{Ti}_x\text{O}_3$ single crystals. *J Cryst Growth.* 2003; 250:118–125.
240. Bing YH, Ye ZG. Synthesis, phase segregation and properties of piezo/ferroelectric $\text{Pb}(\text{Sc}_{1/2}\text{Nb}_{1/2})_{1-x}\text{Ti}_x\text{O}_3$ single crystals. *J Cryst Growth.* 2006; 287:326–329.
241. Zhang S, Rehrig P, Randall C, Shrout R. Crystal Growth and Electrical Properties of $\text{Pb}(\text{Yb}_{1/2}\text{Nb}_{1/2})\text{O}_3$ - PbTiO_3 Perovskite Single Crystal. *J Cryst Growth.* 2002; 234:415–420.
242. Zhang S, Rhee S, Randall C, Shrout R. Dielectric and Piezoelectric Properties of High Curie Temperature Single Crystals in the $\text{Pb}(\text{Yb}_{1/2}\text{Nb}_{1/2})\text{O}_3$ - $x\text{PbTiO}_3$ Solid Solution Series. *Jpn J Appl Phys.* 2002; 41:722–726.
243. Zhang SJ, Lebrun L, Rhee S, Eitel R, Randall CA, Shrout TR. Crystal Growth and Characterization of New High Curie Temperature (1-x) BiScO_3 - $x\text{PbTiO}_3$ Single Crystals. *J Cryst Growth.* 2002; 236:210–216.
244. Bing YH, Ye ZG. Effects of growth conditions on the domain structure and dielectric properties of $\text{Pb}(\text{Sc}_{1/2}\text{Nb}_{1/2})_{1-x}\text{Ti}_x\text{O}_3$ single crystals. *Mater Sci Eng B.* 2005; 120:72–75.
245. Yamashita Y, Shimanuki S. Synthesis of lead scandium niobate-lead titanate pseudo binary system single crystals. *Mater Res Bull.* 1996; 31:887–895.
246. Guo Y, Luo H, He T, Yin Z. Peculiar properties of a high Curie temperature $\text{Pb}(\text{In}_{1/2}\text{Nb}_{1/2})\text{O}_3$ - PbTiO_3 single crystal grown by the modified Bridgman technique. *Solid Stat Commun.* 2002; 123:417–420.
247. Yasuda N, Ohwa H, Kume M, Hayashi K, Hosono Y, Yamashita Y. Crystal growth and electrical properties of lead indium niobate-lead titanate binary single crystals. *J Cryst Growth.* 2001; 229:299–304.
248. Yasuda N, Ohwa H, Kume M, Yamashita Y. Piezoelectric properties of a high Curie temperature $\text{Pb}(\text{In}_{1/2}\text{Nb}_{1/2})\text{O}_3$ - PbTiO_3 binary system single crystal near a morphotropic phase boundary. *Jpn J Appl Phys.* 2000; 39:L66–L68.
249. Yasuda N, Mori N, Ohwa H, Hosono Y, Yamashita Y, Iwata M, et al. Crystal growth and some properties of lead indium niobate-lead titanate single crystals produced by solution Bridgman method. *Jpn J Appl Phys.* 2002; 41:7007–7010.
250. Guo Y, Luo H, He T, Pan X, Yin Z. *Mater Res Bull.* 2003; 38:857–864.
251. Duan ZQ, Xu GS, Wang XF, Yang DF, Pan XM, Wang PC. Electrical properties of a high Curie temperature $\text{Pb}(\text{In}_{1/2}\text{Nb}_{1/2})\text{O}_3$ - PbTiO_3 single crystal grown by the solution Bridgman technique. *Solid Stat Commun.* 2005; 134:559–563.
252. Zhang S, Randall CA, Shrout TR. High Curie temperature piezocrystals in the BiScO_3 - PbTiO_3 perovskite system. *Appl Phys Lett.* 2003; 83:3150–3152.
253. Zhang S, Randall CA, Shrout TR. Electromechanical properties in rhombohedral BiScO_3 - PbTiO_3 single crystals as a function of temperature. *Jpn J Appl Phys.* 2003; 42:L1152–L1154.
254. Yasuda N, Ohwa H, Kume M, Hosono Y, Yamashita Y, Ishino S, et al. *Jpn J Appl Phys.* 2001; 40:5664–5667.
255. Hosono Y, Harada K, Yamashita Y, Dong M, Ye ZG. *Jpn J Appl Phys.* 2000; 39:5589–5592.
256. Hosono Y, Yamashita Y, Sakamoto H, Ichinose N. *Jpn J Appl Phys.* 2003; 42:5681–5686.
257. Hosono Y, Yamashita Y, Sakamoto H, Ichinose N. *Jpn J Appl Phys.* 2002; 41:L1240–L1242.
258. Luo J, Hackenberger W, Zhang S, Shrout TR. *IEEE Ultrasonic Symp.* 2008:261–264.
259. Zhang S, Lebrun L, Rhee S, Randall CA, Shrout TR. Shear mode piezoelectric properties of $\text{Pb}(\text{Yb}_{1/2}\text{Nb}_{1/2})\text{O}_3$ - PbTiO_3 Single Crystals. *Appl Phys Lett.* 2002; 81:892–894.
260. Wang W, Liu D, Zhang QH, Ren B, Zhang YY, Jiao J, et al. *J Appl Phys.* 2010; 107:084101.
261. Zhang YY, Liu DA, Zhang QH, Wang W, Ren B, Zhao XY, et al. Complete set of material constants of $\langle 011 \rangle$ -poled rhombohedral single-crystal $0.25\text{Pb}(\text{In}_{1/2}\text{Nb}_{1/2})\text{O}_3$ - $0.47\text{Pb}(\text{Mg}_{1/3}\text{Nb}_{2/3})\text{O}_3$ - 0.28PbTiO_3 . *J Electro Mater.* 2011; 40:92–96.

262. Zhang YY, Li XB, Liu DA, Zhang QH, Wang W, Ren B, et al. The compositional segregation, phase structure and properties of $\text{Pb}(\text{In}_{1/2}\text{Nb}_{1/2})\text{O}_3\text{-Pb}(\text{Mg}_{1/3}\text{Nb}_{2/3})\text{O}_3\text{-PbTiO}_3$ single crystal. *J Cryst Growth*. 2011; 318:890–894.
263. Zhou D, Cheung K, Lam K, Chen Y, Chiu Y, Dai J, et al. *Rev Sci Instrum*. 2011; 82:055110. [PubMed: 21639541]
264. Yan WX, Xia ZG, Li Q, Zhang SF. Growth and electrical performance of PMN-PT-PFN single crystals. *Mater Res Bull*. 2009; 44:1256–1260.
265. Duan ZQ, Xu GS, Wang XF, Yang DF. Growth and electrical properties of PIN-PT crystals by the solution Bridgman method. *J Cryst Growth*. 2005; 275:E1907–E1911.
266. Zhang S, Randall CA, Shrout TR. Characterization of perovskite piezoelectric single crystals of $0.43\text{BiScO}_3\text{-}0.57\text{PbTiO}_3$ with high Curie temperature. *J Appl Phys*. 2004; 95:4291–4295.
267. Zhang SJ, Randall CA, Shrout TR. Dielectric and piezoelectric properties of BS-PT crystals with morphotropic phase boundary composition. *Jpn J Appl Phys*. 2004; 43:6199–6203.
268. Kong LP, Wang LH, Zhang SJ, Tschauer O, Zhao YS, Yang WG, et al. *in situ* structural characterization of PYN-PT crystals under high pressure-temperature. *Appl Phys Lett*. 2012; 101:062904.
269. Li Q, Zhang YL, Xia ZG, Chu XC. MPB design and crystal growth of PMN-PT-PZ relaxor ferroelectrics. *J Cryst Growth*. 2011; 318:851–855.
270. Zhang SJ, Lee SM, Kim DH, Lee HY, Shrout TR. Characterization of high T_C PMN-PZ-PT single crystals fabricated by solid state crystal growth. *Appl Phys Lett*. 2007; 90:232911.
271. Amin A, Lee HY, Kelly B. High transition temperature lead magnesium niobate-lead zirconate titanate single crystals. *Appl Phys Lett*. 2007; 90:242912.
272. Zhang SJ, Lee SM, Kim DH, Lee HY, Shrout TR. Temperature dependence of the dielectric, piezoelectric and elastic constants for PMN-PZ-PT piezocrystals. *J Appl Phys*. 2007; 102:114103.
273. Zhang SJ, Lee SM, Kim DH, Lee HY, Shrout TR. Characterization of Mn modified PMN-PZ-PT single crystals for high power broad bandwidth transducers. *Appl Phys Lett*. 2008; 93:122908. [PubMed: 19529783]
274. Xia ZG, Li Q, Zhang SF. Growth and characterization of PMN-PT-PZ single crystals with high rhombohedral /tetragonal phase transition temperature. *Solid Stat Commun*. 2008; 145:38–42.
275. Zhang SJ, Lee SM, Kim DH, Lee HY, Shrout TR. Electromechanical properties of PMN-PZT piezoelectric single crystals near morphotropic phase boundary compositions. *J Am Ceram Soc*. 2007; 90:3859–3862.
276. Finkel P, Robinson H, Stace J, Amin A. Study of phase transitions in ternary lead indium niobate-lead magnesium niobate-lead titanate relaxor ferroelectric morphotropic single crystals. *Appl Phys Lett*. 2010; 97:122903.
277. Finkel P, Benjamin K, Amin A. Large strain transduction utilizing phase transition in relaxor-ferroelectric PIN-PMN-PT single crystals. *Appl Phys Lett*. 2011; 98:192902.
278. Zhang SJ, Luo J, Hackenberger W, Shrout TR. Characterization of PIN-PMN-PT ferroelectric crystal with enhanced phase transition temperatures. *J Appl Phys*. 2008; 104:064106.
279. Tian J, Han PD, Huang XL, Pan HX, Carroll JF, Payne DA. Improved stability for piezoelectric crystals grown in the lead indium niobate-lead magnesium niobate-lead titanate system. *Appl Phys Lett*. 2007; 91:222903.
280. Xu GS, Chen K, Yang DF, Li JB. Growth and electrical properties of large size PIN-PMN-PT crystals prepared by the vertical Bridgman technique. *Appl Phys Lett*. 2007; 90:032901.
281. Hosono Y, Yamashita Y, Hirayama K, Ichinose N. Dielectric and piezoelectric properties of PIN-PMN-PT single crystals. *Jpn J Appl Phys*. 2005; 44:7037–7041.
282. Zhang SJ, Luo J, Hackenberger W, Sherlock NP, Meyer RJ Jr, et al. Electromechanical characterization of PIN-PMN-PT crystals as a function of crystallographic orientation and temperature. *J Appl Phys*. 2009; 105:104506. [PubMed: 24753628]
283. Wang X, Zhang HW, Lin D, Wang S, Zhao XY, Chen JW, et al. An effective growth method to improve the homogeneity of relaxor ferroelectric single crystal PIN-PMN-PT. *Cryst Res Tech*. 2014; 49:122–128.

284. Wang X, Xu Z, Li ZR, Chen HB. Study on the inhomogeneity of PIN-PMN-PT single crystal along the growth direction. *Solid Stat Commun.* 2010; 150:1425–1428.
285. Han, PD. Process for the preparation of piezoelectric crystal elements. US Patent. 7908722 B2. 2011.
286. Matsushita, M.; Iwasaki, Y. Piezoelectric single crystal device. US. 20060091353 A1. 2006.
287. Han, PD. Piezoelectric crystal elements of shear mode and process for the preparation thereof. US. 20070290579 A1. 2007.
288. Luo, J.; Hackenberger, WS. Method of making ternary piezoelectric crystals. US Patent. 7972527 B2. 2011.
289. Luo, J.; Hackenberger, WS. Method of making ternary piezoelectric crystals. US Patent. 8597535 B2. 2013.
290. Liu XZ, Zhang SJ, Luo J, Shrout TR, Cao WW. Complete set of material constants of $\text{Pb}(\text{In}_{1/2}\text{Nb}_{1/2})\text{O}_3\text{-Pb}(\text{Mg}_{1/3}\text{Nb}_{2/3})\text{O}_3\text{-PbTiO}_3$ single crystal with morphotropic phase boundary composition. *J Appl Phys.* 2009; 106:074112.
291. Wan YH, Li ZR, Chen HB, Li F, Xu Z, Fan SJ, Yao X. Variations of composition and dielectric properties of PIN-PMN-PT single crystal along growth direction. *J Appl Phys.* 2013; 113:124105.
292. Liu XZ, Zhang SJ, Luo J, Shrout TR, Cao WW. A complete set of material properties of single domain 0.26PIN-0.46PMN-0.28PT single crystals. *Appl Phys Lett.* 2010; 96:012907.
293. Li F, Zhang SJ, Xu Z, Wei XY, Luo J, Shrout TR. Electromechanical properties of tetragonal PIN-PMN-PT ferroelectric crystals. *J Appl Phys.* 2010; 107:054107.
294. Zhao P, Goljahi S, Dong W, Wu T, Finkel P, Sahul R, et al. The strength of PIN-PMN-PT single crystals under bending with a longitudinal electric field. *Smart Mat Struct.* 2011; 20:055006.
295. Wang X, Xu Z, Li ZR, Li F, Chen HB, Fan SJ. Growth of the relaxor based ferroelectric single crystals PIN-PMN-PT by vertical Bridgman technique. *Ferroelectrics.* 2010; 401:173–180.
296. Sherlock NP, Zhang SJ, Luo J, Meyer RJ Jr, Shrout TR. Large signal, dynamic properties of low loss modified PMNT single crystals. *J Appl Phys.* 2010; 107:074108.
297. Sun EW, Cao WW, Jiang WH, Han PD. Complete set of material properties of single domain PIN-PMN-PT single crystal and the orientation effects. *Appl Phys Lett.* 2011; 99:032901.
298. Zhang SJ, Luo J, Li F, Meyer RJ Jr, Hackenberger W, Shrout TR. Polarization fatigue in PIN-PMN-PT single crystals. *Acta Mater.* 2010; 58:3773–3780. [PubMed: 20652090]
299. Dong WD, Finkel P, Amin A, Lynch CS. Giant electro-mechanical energy conversion in [011] cut ferroelectric single crystals. *Appl Phys Lett.* 2012; 100:042903.
300. Sun EW, Zhang SJ, Luo J, Shrout TR, Cao WW. Elastic, dielectric, and piezoelectric constants of PIN-PMN-PT single crystal poled along [011]_C. *Appl Phys Lett.* 2010; 97:032902. [PubMed: 20714370]
301. Finkel P, Murphy CJ, Stace J, Bussmann K, Heitmann A, Amin A. Elastic stability of high coupling ternary single crystals. *Appl Phys Lett.* 2013; 102:182903.
302. Zhang SJ, Li F, Luo J, Xia R, Hackenberger W, Shrout TR. Investigation of single and multi-domain PIN-PMN-PT crystals with mm2 symmetry. *Appl Phys Lett.* 2010; 97:132903. [PubMed: 20981273]
303. Dong W, Finkel P, Amin A, Lynch CS. Mechanical energy harvesting utilizing phase transition in 32 mode relaxor-ferroelectric PIN-PMN-PT single crystals. *Proceeding of SPIE.* 2012; 8343:834308.
304. Luo J, Hackenberger W, Zhang SJ, Shrout TR. A high Q_m relaxor ferroelectric single crystal: growth and characterization. *IEEE- Ultrasonic proceeding.* 2010:68–71.
305. Li F, Zhang SJ, Lin DB, Luo J, Xu Z, Wei XY, et al. Electromechanical properties of PIN-PMN-PT single crystals. *J Appl Phys.* 2011; 109:014108.
306. Zhang SJ, Liu G, Jiang WH, Luo J, Cao WW, Shrout TR. Characterization of single domain PIN-PMN-PT crystals with monoclinic phase. *J Appl Phys.* 2011; 110:064108.
307. Sun P, Zhou QF, Zhu BP, Wu DW, Hu CL, Cannata JM, et al. Design and fabrication of PIN-PMNPT single crystal high frequency ultrasound transducers. *IEEE Trans Ultrason Ferroelectr Freq Contr.* 2009; 56:2760–2763.

308. Sun EW, Zhang R, Wu FM, Cao WW. Complete matrix properties of [001] and [011] poled 0.33PIN-0.38PMN-0.29PT single crystals. *J Alloys Compounds*. 2013; 553:267–269.
309. Li F, Zhang SJ, Xu Z, Wei XY, Luo J, Shrout TR. Investigation of electromechanical properties and related temperature characteristics in domain engineered tetragonal PIN-PMN-PT crystals. *J Am Ceram Soc*. 2010; 93:2731–2734.
310. Sun EW, Zhang R, Wu FM, yang B, Cao WW. Influence of manganese doping to the full tensor properties of 0.24PIN-0.47PMN-0.29PT single crystals. *J Appl Phys*. 2013; 113:074108.
311. Liu G, Jiang WH, Zhu JQ, Cao WW. Pure low frequency flexural mode of [011] poled relaxor-PT single crystals excited by k_{32} mode. *Appl Phys Lett*. 2012; 100:213501. [PubMed: 22711914]
312. Wu FM, yang B, Sun EW, Zhang R, Xu DP, Zhou J, Cao WW. Polarization raman study on phase transitions in PIN-PMN-PT single crystal. *J Alloys Compounds*. 2012; 551:98–100.
313. Sun EW, Cao WW, Han PD. Complete set of material properties of [011] poled 0.24PIN-0.46PMN-0.30PT single crystal. *Mater Lett*. 2011; 65:2855–2857. [PubMed: 21857760]
314. Zhou QF, Zhu BP, Wu DW, Hu CH, Cannata JM, Tian J, et al. PIN-PMN-PT single crystal high frequency ultrasound transducers for medical applications. *IEEE IUS*. 2008:1433–1436.
315. Chen RM, Wu JC, Lam KH, Yao LH, Zhou QF, Tian J, et al. Thermal-independent properties of PIN-PMN-PT single crystal linear array ultrasonic transducers. *IEEE Trans Ultrason Ferroelectr Freq Contr*. 2012; 59:2777–2784.
316. Smith WA. Office of Naval Research, continuing advocacy of the fundamental studied on the Relaxor-PT crystal materials for more than 20 years, first proposed the nomenclature of the varieties of piezocrystals at 2010 Navy Workshop of Acoustic Transduction Materials and Devices.
317. Zhang S, Lee SM, Kim DH, Lee HY, Shrout TR. Elastic, piezoelectric and dielectric properties of 0.71PMN-0.29PT crystals obtained by solid-state crystal growth. *J Am Ceram Soc*. 2008; 91:683–686.
318. Zhang SJ, Shrout TR. Relaxor-PT single crystals: Observations and developments. *IEEE Trans Ultrason Ferroelectr Freq Contr*. 2010; 57:2138–2146.
319. Zhang SJ, Yu FP. Piezoelectric materials for high temperature sensors. *J Am Ceram Soc*. 2011; 94:3153–3170.
320. Han, P.; Tian, J.; Yan, W. Bridgman growth and properties of PMN-PT based single crystals. In: Ye, ZG., editor. *Handbook of Advanced Dielectric, Piezoelectric and Ferroelectric Materials – Synthesis, Characterization and Applications*. England: Woodhead Publishing Ltd., Cambridge; 2008. p. 3-37.
321. Hackenberger, W.; Luo, J.; Jiang, XN.; Snook, KA.; Rehrig, PW.; Zhang, SJ., et al. Recent developments and applications of piezoelectric crystals. In: Ye, ZG., editor. *Handbook of Advanced Dielectric, Piezoelectric and Ferroelectric Materials – Synthesis, Characterization and Applications*. England: Woodhead Publishing Ltd., Cambridge; 2008. p. 73-100.
322. Rhim, SM.; Shin, MC.; Lee, SG. Piezoelectric single crystals for medical ultrasonic transducers. In: Ye, ZG., editor. *Handbook of Advanced Dielectric, Piezoelectric and Ferroelectric Materials – Synthesis, Characterization and Applications*. England: Woodhead Publishing Ltd., Cambridge; 2008. p. 101-129.
323. Cao, WW. Full-set Material Properties and Domain Engineering Principles of Ferroelectric Single Crystals. In: Ye, ZG., editor. *Handbook of Advanced Dielectric, Piezoelectric and Ferroelectric Materials – Synthesis, Characterization and Applications*. England: Woodhead Publishing Ltd., Cambridge; 2008. p. 235-265.
324. Damjanovic, D.; Davis, M.; Budimir, M. Enhancement of Piezoelectric Properties in Perovskite Crystals by Thermally, Compositionally, Electric Field and Stress-induced Instabilities. In: Ye, ZG., editor. *Handbook of Advanced Dielectric, Piezoelectric and Ferroelectric Materials – Synthesis, Characterization and Applications*. England: Woodhead Publishing Ltd., Cambridge; 2008. p. 304-332.
325. Zhang, SJ.; Luo, J.; Snyder, DW.; Shrout, TR. High performance, high temperature piezoelectric crystals. In: Ye, ZG., editor. *Handbook of Advanced Dielectric, Piezoelectric and Ferroelectric Materials – Synthesis, Characterization and Applications*. England: Woodhead Publishing Ltd., Cambridge; 2008. p. 130-157.

326. Bing, YH.; Ye, ZG. Piezo- and Ferroelectric (1-x)PSN-xPT Solid Solution System. In: Ye, ZG., editor. Handbook of Advanced Dielectric, Piezoelectric and Ferroelectric Materials – Synthesis, Characterization and Applications. England: Woodhead Publishing Ltd., Cambridge; 2008. p. 173-204.
327. Yamashita, YJ.; Hosono, Y. High Curie Temperature Piezoelectric Single Crystals of the PIN-PMN-PT Ternary Materials system. In: Ye, ZG., editor. Handbook of Advanced Dielectric, Piezoelectric and Ferroelectric Materials – Synthesis, Characterization and Applications. England: Woodhead Publishing Ltd., Cambridge; 2008. p. 205-234.
328. Lim, LC. Flux growth and characterization of PZN-PT and PMN-PT single crystals. In: Ye, ZG., editor. Handbook of Advanced Dielectric, Piezoelectric and Ferroelectric Materials – Synthesis, Characterization and Applications. England: Woodhead Publishing Ltd., Cambridge; 2008. p. 38-72.
329. Jones JL, Slamovich EB, Bowman KJ. Domain texture distributions in tetragonal lead zirconate titanate by x-ray and neutron diffraction. *J Appl Phys.* 2005; 97:034113.
330. Li F, Wang LH, Jin L, Xu Z, Zhang S. Achieving single domain relaxor-PT crystals by high temperature poling. *Cryst Eng Comm.* 2014; 16:2892–2897.
331. Bell AJ. Phenomenologically derived electric field-temperature phase diagrams and piezoelectric coefficients for single crystal barium titanate under fields along different axes. *J Appl Phys.* 2001; 89:3907–3914.
332. Han PD, Yan WL, Tian J, Huang XL, Pan HX. Cut directions for the optimization of piezoelectric coefficients of lead magnesium niobate-lead titanate ferroelectric crystals. *Appl Phys Lett.* 2005; 86:052902.
333. Zhang S, Jiang W, Meyer RJ Jr, Li F, Luo J, Cao WW. Measurements of face shear properties in Relaxor-PT single crystals. *J Appl Phys.* 2011; 110:064106.
334. Zhang S, Sherlock N, Meyer RJ Jr, Shrout TR. Crystallographic dependence of loss in domain engineered Relaxor-PT single crystals. *Appl Phys Lett.* 2009; 94:162906. [PubMed: 19654880]
335. Zhang S, Li F, Jiang W, Luo J, Meyer RJ Jr, Cao W, Shrout TR. Face shear piezoelectric properties of relaxor-PbTiO₃ single crystals. *Appl Phys Lett.* 2011; 98:182903. [PubMed: 21629563]
336. Kong LP, Liu G, Zhang S, Liu HZ. Importance of tetragonal side morphotropic phase boundary in modified Relaxor-PT crystals for high power transducer applications. *J Appl Phys.* 2013; 114:144106.
337. Lin D, Zhang S, Li ZR, Li F, Xu Z, Wada S, Luo J, Shrout TR. Domain size engineering in tetragonal PIN-PMN-PT crystals. *J Appl Phys.* 2011; 110:084110.
338. Shen ZY, Tang YX, Zhang S, Luo J, Li YM, Shrout TR. Enhanced piezoelectric activity and temperature stability of [111] oriented orthorhombic PMN-PT single crystals by domain size engineering. *Script Mater.* 2014; 72–73:17–20.
339. Li F, Zhang SJ, Xu Z, Wei XY, Luo J, Shrout TR. Temperature independent piezoelectric shear response in relaxor-lead titanate based crystals. *Appl Phys Lett.* 2010; 97:252903. [PubMed: 21245942]
340. Li F, Zhang SJ, Xu Z, Wei XY, Shrout TR. Critical property in Relaxor-PT single crystals- Shear piezoelectric response. *Adv Funct Mater.* 2011; 21:2118–2128. [PubMed: 21960942]
341. Zhang R, Jiang B, Cao WW. Orientation dependence of piezoelectric properties of single domain 0.67Pb(Mn_{1/3}Nb_{2/3})O₃–0.33PbTiO₃ crystals. *Appl Phys Lett.* 2003; 82:3737–3739.
342. Newnham, RE. Properties of materials: anisotropy, symmetry and structure. New York: Oxford University Press; 2005.
343. Damjanovic D. A morphotropic phase boundary system based on polarization rotation and polarization extension. *Appl Phys Lett.* 2010; 97:062906.
344. Li F, Jin L, Xu Z, Wang DW, Zhang S. Electrostrictive effect in PMN-xPT crystals. *Appl Phys Lett.* 2013; 102:152910.
345. Li F, Jin L, Xu Z, Zhang SJ. Electrostrictive effect in ferroelectrics: An alternative approach to improve piezoelectricity. *Appl Phys Rev.* 2014; 1:011103.
346. Damjanovic, D. Hysteresis in piezoelectric and ferroelectric materials. In: Mayergoyz, I.; Bertotti, G., editors. Chapter 4 in The science of hysteresis. Vol. 3. New York: Elsevier; 2005.

347. Eitel RE, Shrout TR, Randall CA. Nonlinear Contributions to the Dielectric Permittivity and Converse Piezoelectric Coefficient in Piezoelectric Ceramics. *J Appl Phys*. 2006; 99:124110.
348. Hall DA. Review Nonlinearity in Piezoelectric Ceramics. *J Mater Sci*. 2001; 36:4575–4601.
349. Damjanovic D, Demartin M. The Rayleigh Law in Piezoelectric Ceramics. *J Phys D: Appl Phys*. 1996; 29:2057–2060.
350. Gharb NB, Trolier-McKinstry S. Dielectric Nonlinearity of $\text{Pb}(\text{Yb}_{1/2}\text{Nb}_{1/2})\text{O}_3\text{-PbTiO}_3$ Thin Films with {100} and {111} Crystallographic Orientation. *J Appl Phys*. 2005; 97:064106.
351. Bassiri-Gharb N, Fujii I, Hong E, Trolier-McKinstry S, Taylor DV, Damjanovic D. Domain wall contributions to the properties of piezoelectric thin films. *J Electroceram*. 2007; 19:47–65.
352. Bernal A, Zhang S, Bassiri-Gharb N. Effects of orientation and composition on the extrinsic contributions to the dielectric response of relaxor ferroelectric single crystals. *Appl Phys Lett*. 2009; 95:142911.
353. Trolier-McKinstry S, Bassiri-Gharb N, Damjanovic D. Piezoelectric nonlinearity due to motion of 180° domain walls in ferroelectric materials at subcoercive fields: a dynamic poling model. *Appl Phys Lett*. 2006; 88:202901.
354. Li F, Zhang SJ, Xu Z, Wei XY, Luo J, Shrout TR. Composition and phase dependence of the intrinsic/extrinsic piezoelectric activity in domain engineered $(1-x)\text{PMN-xPT}$ crystals. *J Appl Phys*. 2010; 108:034106. [PubMed: 20806001]
355. Damjanovic D. Contributions to the Piezoelectric Effect in Ferroelectric Single Crystals and Ceramics. *J Am Ceram Soc*. 2005; 88:2663–2676.
356. Pramanick A, Damjanovic D, Nino JC, Jones JL. Subcoercive Cyclic Electrical Loading of Lead Zirconate Titanate Ceramics I: Nonlinearities and Losses in the Converse Piezoelectric Effect. *J Am Ceram Soc*. 2009; 92:2291–2299.
357. Huo X, Zhang S, Liu G, Zhang R, Luo J, Sahul R, et al. Elastic, dielectric and piezoelectric characterization of [011] poled PIN-PMN-PT: Mn single domain crystals. *J Appl Phys*. 2012; 112:124113. [PubMed: 23341689]
358. Huo X, Zhang S, Liu G, Zhang R, Luo J, Sahul R, et al. Elastic, dielectric and piezoelectric characterization of rhombohedral Mn modified PIN-PMN-PT crystals poled along [011] direction. *J Appl Phys*. 2013; 113:074106.
359. Dong SX, Yan L, Wang NG, Viehland D, Jiang XN, Rehrig P, et al. A small, linear, piezoelectric ultrasonic cryomoter. *Appl Phys Lett*. 2005; 86:053501.
360. Jiang XN, Rehrig PW, Hackenberger W, Shrout TR. Cryogenic actuators and motors using single crystal piezoelectrics. *AIP Conference Proceedings*. 2006; 823:1783–1789.
361. Woody SC, Smith ST, Jiang XN, Rehrig P. Performance of single crystal PMN-32%PT stacked actuators with application to adaptive structures. *Rev Sci Instrum*. 2005; 76:075112.
362. Xu TB, Jiang XN, Su J. A piezoelectric multilayer stacked hybrid actuation/transduction system. *Appl Phys Lett*. 2011; 98:243503.
363. Li F, Zhang SJ, Xu Z, Wei XY, Luo J, Shrout TR. Piezoelectric activity of relaxor-PT based single crystals and polycrystalline ceramics at cryogenic temperatures: intrinsic and extrinsic contributions. *Appl Phys Lett*. 2010; 96:192903. [PubMed: 20531980]
364. Xu TB, Tolliver L, Jiang XN, Su J. A single crystal lead magnesium niobate-lead titanate multilayer stacked cryogenic flextensional actuator. *Appl Phys Lett*. 2013; 102:042906.
365. Martin F, Brake MT, Lebrun L, Zhang SJ, Shrout TR. Dielectric and piezoelectric activities in $(1-x)\text{PMN-xPT}$ single crystals from 5K to 300K. *J Appl Phys*. 2012; 111:104108.
366. Dong SX, Yan L, Viehland D, Jiang XN, Hackenberger WS. A piezoelectric single crystal traveling wave step motor for low temperature application. *Appl Phys Lett*. 2008; 92:153504.
367. Jiang XN, Rehrig PW, Hackenberger WS, Smith E, Dong SX, Viehland D, et al. Advanced piezoelectric single crystal based actuators. *Proceeding of SPIE*. 2005; 5761:253–262.
368. Grupp DE, Goldman AM. Giant Piezoelectric Effect in Strontium Titanate at Cryogenic Temperatures. *Science*. 1997; 276:392–394. [PubMed: 9103192]
369. Zhang QM, Wang H, Kim N, Cross LE. Direct evaluation of domain wall and intrinsic contributions to the dielectric and piezoelectric response and their temperature dependence on lead zirconate titanate ceramics. *J Appl Phys*. 1994; 75:454–459.

370. Sabat RG, Mukherjee B, Ren W, Yang G. Temperature dependence of the complete material coefficients matrix of soft and hard doped piezoelectric lead zirconate titanate ceramics. *J Appl Phys.* 2007; 101:064111.
371. Wan X, Zhang RK, Chan HLW, Choy CL, Zhao X, Luo H. Abnormal phase transitions for tetragonal $(1-x)\text{Pb}(\text{Mg}_{1/3}\text{Nb}_{2/3})\text{O}_3\text{-xPbTiO}_3$ single crystals at low temperature. *J Appl Phys.* 2004; 96:6574–6577.
372. Wang F, Or SW, Zhao X, Luo HS. Cryogenic dielectric and piezoelectric activities in rhombohedral PMN-PT single crystals with different crystallographic orientations. *J Phys D: Appl Phys.* 2009; 42:182001.
373. Pramanick A, Damjanovic D, Daniels JE, Nino JC, Jones JL. Origins of electromechanical coupling in polycrystalline ferroelectrics during subcoercive electrical loading. *J Am Ceram Soc.* 2011; 94:293–309.
374. Zhang S, Li F, Luo J, Sahul R, Shrout TR. Relaxor-PbTiO₃ single crystals for various applications. *IEEE Trans Ultrason Ferroelectr Freq Contr.* 2013; 60:1572–1580.
375. Zhang SJ, Li F, Luo J, Xia R, Hackenberger W, Shrout TR. Field stability of piezoelectric shear properties in PIN-PMN-PT crystals under large drive field. *IEEE Trans Ultrason Ferroelectr Freq Contr.* 2011; 58:274–280.
376. Van Tol, DJ.; Meyer, RJ. Acoustic transducer. US Patent. 7615912 B2. 2009.
377. Meyer, RJ., Jr; Tremper, TM.; Markley, DC.; Van Tol, D.; Han, PD.; Tian, J. Low profile, broad bandwidth projector design using d₃₆ shear mode. State College, PA: U.S. Navy Workshop on Acoustic Transduction Materials and Devices; 2010 May 11–13.
378. Kim K, Zhang SJ, Tian J, Han PD, Jiang XN. Face shear mode ultrasonic tactile sensor array. *IEEE IUS.* 2012:1059–1062.
379. Kim K, Zhang S, Jiang X. Surface load induced electrical impedance shift in relaxor-PT crystal piezoelectric resonators. *Appl Phys Lett.* 2012; 100:253501.
380. Kim K, Zhang S, Jiang X. Surface acoustic load sensing using a face-shear PMN-PT single crystal resonator. *IEEE Trans Ultrason Ferroelectr Freq Contr.* 2012; 59:2548–2554.
381. Li SY, Jiang WH, Zheng LM, Cao WW. A face shear mode single crystal ultrasonic motor. *Appl Phys Lett.* 2013; 102:183512.
382. Ci PH, Liu GX, Chen ZJ, Zhang SJ, Dong SX. High-order face-shear modes of relaxor-PT crystals for piezoelectric motor applications. *Appl. Phys. Lett.* 2014; 104:242911.
383. Zhang SJ, Li F, Shrout TR, Luo J. Relaxor-PT single crystals for various applications. *IEEE ISAF.* 2012
384. Kim, Y.; Horii, SC. Display and PACS. Washington: SPIE Press; 2000. Handbook of medical imaging, Vol. 3.
385. Callerame J, Tancrell RH, Wilson DT. Transmitters and receivers for medical ultrasonics. *IEEE IUS.* 1979:407–451.
386. Zhou D, Cheung KF, Chen Y, Lau ST, Zhou QF, Shung KK, et al. Fabrication and performance of endoscopic ultrasound radial arrays based on PMN-PT single crystal/epoxy 1–3 composite. *IEEE Trans Ultrason Ferroelectr Freq Contr.* 2011; 58:477–484.
387. Lau ST, Li H, Wong KS, Zhou QF, Zhou D, Li YC, et al. Multiple matching scheme for broadband 0.72PMN-0.28PT single crystal phased-array transducer. *J Appl Phys.* 2009; 105:094908.
388. Lee, HJ. PhD dissertation. The Pennsylvania State University; 2012. Low loss 1–3 piezocomposites for high power ultrasonic transducers.
389. Lockwood G, Turnbull D, Christopher D, Foster F. Beyond 30MHz: Applications of high frequency ultrasound imaging. *IEEE Eng Med Biol Mag.* 1996; 5:60–71.
390. Scherba G, Hoagland PA, O'Brien WD. Acoustic microscopy: a study of contrast in fresh tissue. *IEEE Trans Ultrason Ferroelectr Freq Contr.* 1994; 41:451–457.
391. Hunt JW, Arditi M, Foster FS. Ultrasound transducers for pulse-echo medical imaging. *IEEE Trans Biomed Eng.* 1983; 30:453–481. [PubMed: 6629380]
392. Cobbold, RSC. Foundations of biomedical ultrasound. New York: Oxford University Press; 2007.

393. Cannata JM, Ritter TA, Chen WH, Shung KK. Design of focused single element (50–100MHz) transducers using lithium niobate. *Proceedings of SPIE*. 2001; 4325:28–35.
394. Nakamura, K. *Ultrasonic Transducers: Materials and Design for Sensors, Actuators and Medical Applications*. Cambridge: Woodhead Publishing; 2012.
395. Chen, Y. PhD Dissertation. The HongKong Polytechnic University; 2013. High frequency and endoscopic ultrasonic transducers based on PMN-PT and PIN-PMN-PT single crystals.
396. Rehrig, PW.; Jiang, XN.; Hackenberger, WS.; Yuan, JR.; Romley, R. Micromachined imaging transducer. US Patent. 7622853 B2. 2009.
397. Xu Y, Yu Q, Li JF. A facile method to fabricate vertically aligned (K,Na)NbO₃ lead free piezoelectric nanorods. *J. Mater. Chem*. 2012; 22:23221–23226.
398. Jiang XN, Snook K, Cheng A, Hackenberger W, Geng X. Micromachined PMN-PT single crystal composite transducers 15–75MHz PC-MUT. *IEEE IUS*. 2008:164–167.
399. Jiang XN, Yuan J, Cheng A, Snook K, Cao PJ, Rehrig P, et al. Microfabrication of piezoelectric composite ultrasound transducers (PC-MUT). *IEEE IUS*. 2006:918–921.
400. Yuan J, Jiang X, Cao P, Sadaka A, Bautista R, Snook K, et al. High frequency piezo composites microfabricated ultrasound transducers for intravascular imaging. *IEEE IUS*. 2006:264–268.
401. Jiang XN, Snook K, Liu RB, Geng XC, Hackenberger W. Fabrication and characterization of high frequency phased arrays for NDE imaging. *Proceeding of SPIE*. 2010; 7649:76490X.
402. Yuan J, Rhee S, Jiang XN. 60MHz PMN-PT based 1–3 composite transducer for IVUS imaging. *IEEE IUS*. 2008:682–685.
403. Rhee S. High frequency (IVUS) ultrasound transducer technology – applications and challenges. *ISAF*. 2007:856–857.
404. Sun P, Wang G, Wu D, Zhu B, Hu C, Liu C, et al. High Frequency PMN-PT 1–3 Composite Transducer for Ultrasonic Imaging Application. *Ferroelectrics*. 2010; 408:120–128. [PubMed: 21869845]
405. Lee HJ, Zhang SJ, Shrouf TR. Scaling effects of relaxor-PT crystals and composites for ultrasonic transducers. *J Appl Phys*. 2010; 107:124107. [PubMed: 20644658]
406. Lee HJ, Zhang SJ, Luo J, Li F, Shrouf TR. Thickness dependent properties of relaxor-PT piezoelectrics for ultrasonic transducers. *Adv Funct Mater*. 2010; 20:3154–3162. [PubMed: 21954374]
407. Wada S, Yako K, Kakemoto H, Tsurumi T, Kiguchi T. Enhanced piezoelectric properties of barium titanate single crystals with different engineered domain sizes. *J Appl Phys*. 2005; 98:014109.
408. Wada S, Muraoka K, Kakemoto H, Tsurumi T, Kumagai H. Enhanced piezoelectric properties of potassium niobate single crystals by domain engineering. *Jpn J Appl Phys*. 2004; 43:6692–6700.
409. Wada S, Muraishi T, Yokoh K, Yako K, Kamemoto H, Tsurumi T. Domain wall engineering in lead free piezoelectric crystals. *Ferroelectrics*. 2007; 355:37–49.
410. Cao WW, Randall CA. Grain size and domain size relations in bulk ceramic ferroelectric materials. *J Phys Chem Solid*. 1996; 57:1499–1505.
411. Zhang S, Lee H, Ma C, Tan XL. Sintering effect on microstructure and properties of KNN ceramics. *J Am Ceram Soc*. 2011; 94:3659–3665.
412. Haertling GH, Zimmer WJ. An analysis of hot pressing parameters for lead zirconate lead titanate ceramics containing two atom percent bismuth. *Ceram Bull*. 1966; 45:1084–1089.
413. Lehmann, JF.; Warren, CG.; Guy, AW. Therapy with continuous wave ultrasound. In: Fry, FJ., editor. *Ultrasound: its applications in medicine and biology, Part II, Chapter 10*. New York: Elsevier; 1978. p. 566–585.
414. Zhou YF. High intensity focused ultrasound in clinical tumor ablation. *World J Clin Oncol*. 2011; 10:8–27. [PubMed: 21603311]
415. Pitt WG, Hussein GA, Staples BJ. Ultrasonic drug delivery- a general review. *Expert Opin Drug Deliv*. 2004; 1:37–56. [PubMed: 16296719]
416. Ng, K.; Matsunaga, TO. Ultrasound-mediated drug delivery, Chapter 12. In: Wang, B.; Siahaan, T.; Soltero, R., editors. *Drug Delivery: Principles and Applications*. John Wiley&Sons-Interscience; 2005.

417. Vaezy S, Andrew M, Kaczkowski P, Crum L. Image guided acoustic therapy. *Annu. Rev Biomed Eng.* 2001; 3:375–390. [PubMed: 11447068]
418. Muto, S.; Horie, S. High Intensity Focused Ultrasound. In: Polascik, TJ., editor. Chapter 20 in *Imaging and Focal Therapy of Early Prostate Cancer*. New York: Humana Press Springer; 2013.
419. Uchino, K. Manufacturing technologies for piezoelectric transducers, Chapter 15, *Advanced Piezoelectric Materials: Science and technology*. Uchino, K., editor. New York: Woodhead Publishing, CRC Press; 2010.
420. Fellingner, K.; Schmid, J. *Klinik und therapie des chronischen gelenkrheumatismus*. Wien, Germany, Maudrich: 1954. p. 549-552.
421. Skauen KM, Zentner GM. Phonophoresis. *Inter J Pharmaceutics.* 1984; 20:235–245.
422. Ng KY, Liu Y. Therapeutic ultrasound: its application in drug delivery. *Med Res Rev.* 2002; 22:204–223. [PubMed: 11857639]
423. Shaw A, ter Haar GR. Requirements for measurement standards in high intensity focused ultrasound fields. National Phys. Lab (NPL) report, ISSN 1744-0599.
424. Lee H, Zhang S. Design of low loss 1–3 piezoelectric composites for high power transducer applications. *IEEE Trans. Ultrason Ferroelectr Freq Contr.* 2012; 59:1969–1975.
425. Zhang S, Xia R, Lebrun L, Anderson D, Shrout TR. Piezoelectric materials for high power, high temperature applications. *Mater Lett.* 2005; 59:3471–3475.
426. Lebrun L, Sebald G, Guiffard B, Richard C, Guyomar D, Pleska E. Investigations on ferroelectric PMN-PT and PZN-PT single crystals ability for power or resonant actuators. *Ultrasonics.* 2004; 42:501–505. [PubMed: 15047336]
427. Zheng LM, Sahul R, Zhang S, Jiang WH, Li SY, Cao WW. Orientation dependence of piezoelectric properties and mechanical quality factors of PIN-PMN-PT:Mn single crystals. *J Appl Phys.* 2013; 114:104105.
428. Sherlock NP, Meyer RJ. Electromechanical nonlinearities and losses in piezoelectric sonar transducer materials. *IEEE Trans Ultrason Ferroelectr Freq Contr.* 2012; 59:1618–1623.
429. Sherlock NP, Garten L, Zhang S, Shrout TR, Meyer RJ Jr. Nonlinear dielectric response in piezoelectric materials for SONAR transducer applications. *J Appl Phys.* 2012; 112:124108.
430. Sherlock NP, Meyer RJ. Modified single crystals for high power underwater projectors. *IEEE Trans. Ultrason Ferroelectr Freq Contr.* 2012; 59:1285–1291.
431. Sherlock NP, Meyer RJ. Large signal response and harmonic distortion in piezoelectrics for SONAR transducers. *J Electroceram.* 2012; 28:202–207.
432. Moffett MB, Robinson HC, Powers JM, Baird PD. Single crystal lead magnesium niobate-lead titanate (PMN/PT) as a broadband high power transduction material. *J Am Acoust Soc.* 2007; 121:2591–2599.
433. Powers JM, Moffett MB, Nussbaum F. Single crystal naval transducer development. *IEEE ISAF.* 2000:351–354.
434. Snook KA, Rehrig PW, Hackenberger W, Jiang XN, Meyer RJ, Markley D. Advanced piezoelectric single crystal based transducers for naval sonar applications. *Proceeding of SPIE.* 2005; 5761:263–271.
435. Rehrig PW, Hackenberger WS, Jiang XN, Meyer RJ, Geng XC. High performance tonpizl transducers utilizing d₃₂ cut piezoelectric single crystals. *Proceeding of SPIE.* 2003; 5053:445–452.
436. Cochran S, Marker M, Marin-Franch P. Ultrabroadband single crystal composite transducers for underwater ultrasound. *IEEE IUS.* 2005:231–234.
437. Snook K, Rehrig P, Hackenberger W, Jiang XN, Meyer RJ, Markley D. Advanced piezoelectric single crystal based transducers for naval sonar applications. *Proceeding of SPIE.* 2006; 6170:61700H.
438. Snook KA, Rehrig P, Hackenberger W, Meyer RJ, Markley D. Tailored single crystal orientations for improved tonpizl transducer performance. *IEEE IUS.* 2006:359–362.
439. Li HD, Deng D, Carlson TJ. Piezoelectric materials used in underwater acoustic transducers. *Sens Lett.* 2012; 10:679–697.

440. Tressler JF, Alkoy S, Newnham RE. Piezoelectric sensors and sensor materials. *J Electroceram.* 1998; 2:257–272.
441. Safari A, Lee YH, Halliyal A, Newnham RE. 0–3 piezoelectric composites prepared by coprecipitated PT powder. *Am Ceram Soc Bull.* 1987; 66:668–670.
442. Safari A. Development of piezoelectric composites for transducers. *J Phys III France.* 1994; 4:1129–1149.
443. Bhalla AS, Ting RY. Hydrophone figure of merit. *Sens Mater.* 1988; 4:181–185.
444. Gao JJ, Xu Z, Li F, Zhang CH, Liu Y, Liu GM. The effect of the hydrostatic pressure on the electromechanical properties of ferroelectric rhombohedral single crystals PMN-PIN-PT. *Appl Phys Lett.* 2011; 99:062903.
445. Ting RY. Composite piezoelectric materials for transduction. *Appl Acoust.* 1994; 41:325–335.
446. Budimir M, Damjanovic D, Setter N. Piezoelectric anisotropy phase transition relations in perovskite single crystals. *J Appl Phys.* 2003; 94:6753–6761.
447. Haun MJ, Furman E, Jang SJ, Cross LE. Thermodynamic theory of the lead zirconate titanate solid solution system, part I Phenomenology. *Ferroelectrics.* 1989; 99:13–25.
448. Budimir M, Damjanovic D, Setter N. Piezoelectric response and free energy instability in the perovskite crystals BT, PT and PZT. *Phys Rev B.* 2006; 73:174106.
449. Bokov AA, Ye ZG. Domain structure in the monoclinic *Pm* phase of PMN-PT single crystals. *J Appl Phys.* 2004; 95:6347–6359.
450. Li F, Zhang SJ, Xu Z, Li ZR, Wei XY. dc bias electric field dependent piezoelectricity for [001] poled PIN-PMN-PT crystals. *J Adv Dielectrics.* 2011; 1:303–308.
451. Li F, Zhang SJ, Xu Z, Lin DB, Li ZR, Wang L. Shear piezoelectric behavior of PIN-PMN-PT crystals under uniaxial stress perpendicular to polar direction. *Appl Phys Lett.* 2012; 100:192901.
452. Luo J, Taylor S, Hackenberger W, Zhang S. Large field property assessment of Mn:PIN-PMN-PT crystals for high power transducers. *IEEE 2013 UFFC, EFTF and PFM Symposium.* :1–4.
453. Zhang S, Taylor S, Li F, Luo J, Meyer RJ. Piezoelectric property of relaxor-PT crystals under uniaxial transverse stress. *Appl Phys Lett.* 2013; 102:172902.
454. Amin A, McLaughlin E, Robinson H, Ewart L. Mechanical and thermal transitions in morphotropic PZN-PT and PMN-PT single crystals and their implication for sound projectors. *IEEE Trans Ultrason Ferroelectr Freq Contr.* 2007; 54:1090–1095.
455. Veihland D, Li JF, Gittings K, Amin A. Electroacoustic properties of <110> oriented PMN-PT crystals under uniaxial stress. *Appl Phys Lett.* 2003; 83:132–134.
456. Budimir M, Damjanovic D, Setter N. Enhancement of the piezoelectric response of tetragonal perovskite single crystals by uniaxial stress applied along the polar axis: a free energy approach. *Phys Rev B.* 2005; 72:064107.
457. Amin A, Haun MJ, Badger B, McKinstry H, Cross LE. A phenomenological Gibbs function for the single cell region of the PZ-PT solid solution system. *Ferroelectrics.* 1985; 65:107–130.
458. Damjanovic D. Comments on origins of enhanced piezoelectric properties in ferroelectrics. *IEEE Trans Ultrason Ferroele Frequency Control.* 56(2009):1574–1585.
459. Uchino K, Hirose S. Loss mechanisms in piezoelectrics: how to measure different losses separately. *IEEE Trans Ultrason Ferroelectr Freq Contr.* 2001; 48:307–321.
460. Gautschi, G. *Piezoelectric Sensorics.* New York: Springer; 2002. p. 106–109.
461. Deng, KK. Underwater acoustic vector sensor using transverse response free, shear mode, PMN-PT crystal. US Patent. 7066026 B2. 2006.
462. Zou, L.; Deng, KK. High sensitivity, low noise piezoelectric flexural sensing structure using <011> poled relaxor-based piezoelectric single crystals. US Patent. 7104140 B2. 2006.
463. Goljahi S, Gallagher J, Zhang S, Luo J, Sahul R, Hackenberger W, et al. A relaxor ferroelectric single crystal cut resulting in large d_{312} and zero d_{311} for shear mode accelerometer and related applications. *Smart Mater Struct.* 2012; 21:055005.
464. Bechmann R, Fair IE. IRE Standards on Piezoelectric Crystals: determination of the elastic, piezoelectric and dielectric constants- the electromechanical coupling factor. *Proc IRE.* 1958; 46:764–778.

465. Bechmann R. Contour modes of square plates excited piezoelectrically and determination of elastic and piezoelectric coefficients. *Proc Phys Soc.* 1951; B64:323–337.
466. Han, PD. 2014 Joint IEEE ISAF-IWATMD-PFM. PA, US: State College; 2014 May 12–16. Review on development of shear mode of PMN-PT based piezoelectric crystals.
467. Dahiya RS, Metta G, Valle M, Sandini G. Tactile sensing-from humans to humanoids. *IEEE Transactions on Robotics.* 2010; 26:1–20.
468. Dahiya, RS.; Valle, M. *Robotic Tactile Sensing.* New York: Springer; 2013.
469. Wilson, JS. *Sensor technology handbook.* New York: Elsevier; 2005.
470. Drafts B. Acoustic wave technology sensors. *IEEE Transactions on Microwave Theory and Techniques.* 2001; 49:795–802.
471. Vellekoop MJ. Acoustic wave sensors and their technology. *Ultrasonics.* 1998; 36:7–14.
472. Jalkanen, V.; Andersson, B.; Lindahl, O. Stiffness of a small tissue phantom measured by a tactile resonance sensor; *Mediterranean conference;* 2010. p. 395-398.
473. Hemsel T, Stroop R, Oliva Uribe D, Wallaschek J. Resonant vibrating sensors for tactile tissue differentiation. *Journal of Sound and Vibration.* 2007; 308:441–446.
474. Oie T, Suzuki H, Murayama Y, Fukuda T, Omata S, Kanda K, et al. Surface elasticity imaging of vascular tissues in a liquid environment by a scanning haptic microscope. *Journal of Artificial Organs.* 2010; 13:121–125. [PubMed: 20473627]
475. Murayama Y, Yoshida M, Mizuno J, Nakamura H, Inoue S, Watanabe Y, et al. Elasticity measurement of zona pellucida using a micro tactile sensor to evaluate embryo quality. *Journal of Mammalian Ova Research.* 2008; 25:8–16.
476. Bonakdar A, Narayanan N. Determination of tissue properties using microfabricated piezoelectric tactile sensor during minimally invasive surgery. *Sens Rev.* 2010; 30:233–241.
477. Dargahi J, Sedaghati R, Singh H, Najarian S. Modeling and testing of an endoscopic piezoelectric-based tactile sensor. *Mechatronics.* 2007; 17:462–467.
478. Chuang CH. Flexible piezoelectric tactile sensors with structural electrodes array. *Recent Advances in Sensing Technology.* 2009; 49:189–202.
479. Lindahl O, Constantinou C, Eklund A, Murayama Y, Hallberg P, Omata S. Tactile resonance sensors in medicine. *J Med Eng Tech.* 2009; 33:263–273.
480. Benes E, Gröschl M, Burger W, Schmid M. Sensors based on piezoelectric resonators. *Sens Actua A: Phys.* 1995; 48:1–21.
481. Schmitt, RM. Method and system for multi-mode mechanical resonator. U. S. Patent. 12117468. 2008 May 8.
482. Sokhanvar S, Packirisamy M, Dargahi J. A multifunctional PVDF-based tactile sensor for minimally invasive surgery. *Smart materials and structures.* 2007; 16:989–998.
483. Dahiya, RS.; Valle, M. *Robotic Tactile Sensing.* Springer; 2013.
484. Itoh H, Nomura M, Katakura N. Quartz-Crystal Tuning-Fork Tactile Sensor. *Japanese Journal of applied physics.* 1999; 38:3225–3227.
485. Watanabe H. A new tactile sensor using the edge mode in a piezoelectric-ceramic bar. *Japanese Journal of Applied Physics.* 2001; 40:3704–3706.
486. Schewe H. Piezoelectricity of uniaxially oriented polyvinylidene fluoride. 1982 *Ultrasonics Symposium.* 1982:519–524.
487. Kwok KW, Chan HLW, Choy CL. Evaluation of the material parameters of piezoelectric materials by various methods. *Ultrasonics, Ferroelectrics and Frequency Control, IEEE Transactions on.* 1997; 44:733–742.
488. Mattiat, OE.; Belincourt, D.; Kikuchi, Y.; Meitzier, AH. *Ultrasonic transducer materials.* New York, NY, USA: Plenum Press; 1971.
489. Balasubramanian, R.; Santos, VJ. *The Human Hand as an Inspiration for Robot Hand Development.* Springer; 2014.
490. MacDonald M, Spalding G, Dholakia K. Microfluidic sorting in an optical lattice. *Nature.* 2003; 426:421–424. [PubMed: 14647376]
491. Fritzsche FS, Dusny C, Frick O, Schmid A. Single-cell analysis in biotechnology, systems biology, and biocatalysis. *Annual review of chemical and biomolecular engineering.* 2012; 3:129–155.

492. Neuman KC, Nagy A. Single-molecule force spectroscopy: optical tweezers, magnetic tweezers and atomic force microscopy. *Nat Meth.* 2008; 5:491–505.
493. Lee J, Shung KK. Radiation forces exerted on arbitrarily located sphere by acoustic tweezer. *The Journal of the Acoustical Society of America.* 2006; 120:1084–1094. [PubMed: 16938994]
494. Kozuka, T.; Tuziuti, T.; Mitome, H.; Arai, F.; Fukuda, T. Three-dimensional acoustic micromanipulation using four ultrasonic transducers. *Micromechatronics and Human Science, 2000. MHS 2000; Proceedings of 2000 International Symposium on; 2000.* p. 201–206.
495. Woodside SM, Bowen BD, Piret JM. Measurement of ultrasonic forces for particle–liquid separations. *AIChE journal.* 1997; 43:1727–1736.
496. Hertz H. Standing-wave acoustic trap for noninvasive positioning of microparticles. *J Appl Phys.* 1995; 78:4845–4849.
497. Wiklund M, Günther C, Lemor R, Jäger M, Fuhr G, Hertz HM. Ultrasonic standing wave manipulation technology integrated into a dielectrophoretic chip. *Lab on a Chip.* 2006; 6:1537–1544. [PubMed: 17203158]
498. Evander M, Lenshof A, Laurell T, Nilsson J. Acoustophoresis in wet-etched glass chips. *Analytical chemistry.* 2008; 80:5178–5185. [PubMed: 18489126]
499. Hammarström B, Evander M, Barbeau H, Bruzelius M, Larsson J, et al. Non-contact acoustic cell trapping in disposable glass capillaries. *Lab on a Chip.* 2010; 10:2251–2257. [PubMed: 20589284]
500. Shi J, Mao X, Ahmed D, Colletti A, Huang TJ. Focusing microparticles in a microfluidic channel with standing surface acoustic waves (SSAW). *Lab on a Chip.* 2008; 8:221–223. [PubMed: 18231658]
501. Ding X, Shi J, Lin SCS, Yazdi S, Kiraly B, Huang TJ. Tunable patterning of microparticles and cells using standing surface acoustic waves. *Lab on a chip.* 2012; 12:2491–2497. [PubMed: 22648600]
502. Wang Z, Zhe J. Recent advances in particle and droplet manipulation for lab-on-a-chip devices based on surface acoustic waves. *Lab on a Chip.* 2011; 11:1280–1285. [PubMed: 21301739]
503. Lee J, Teh SY, Lee A, Kim HH, Lee C, Shung KK. Single beam acoustic trapping. *App Phys Lett.* 2009; 95:073701.
504. Lam KH, Hsu HS, Li Y, Lee C, Lin A, Zhou Q, et al. Ultrahigh frequency lensless ultrasonic transducers for acoustic tweezers application. *Biotechnology and bioengineering.* 2013; 110:881–886. [PubMed: 23042219]
505. Lee J, Ha K, Shung KK. A theoretical study of the feasibility of acoustical tweezers: Ray acoustics approach. *The Journal of the Acoustical Society of America.* 2005; 117:3273–3280. [PubMed: 15957793]
506. Lee C, Lee J, Lau ST, Zhou Q, Shung KK. Single microparticle manipulation by an ultrasound microbeam. *Ultrasonics Symposium (IUS), 2010 IEEE.* 2010:849–852.
507. Hwang JY, Lee C, Lam KH, Kim HH, Lee J, Shung KK. Cell membrane deformation induced by a fibronectin-coated polystyrene microbead in a 200-MHz acoustic trap. *IEEE Trans Ultrason Ferroelectr Freq Contr.* 2014; 61:399–406.
508. Guo S, Zhao L, Zhang K, Lam K, Lau ST, Zhao X, et al. Ultrasonic particle trapping in microfluidic devices using soft lithography. *Appl Phys Lett.* 2008; 92:213901.
509. Lau S, Zhao L, Chan H, Luo H. 60-MHz PMN-PT single crystal transducers for microfluidic analysis systems. *Sens Actua A: Phys.* 2010; 161:78–82.
510. Hsu HS, Zheng F, Li Y, Lee C, Zhou Q, Shung KK. Focused high frequency needle transducer for ultrasonic imaging and trapping. *Appl Phys Lett.* 2012; 101:024105.
511. Li X, Zhang R, Huang N, Lu T, Cao W. Surface acoustic wave propagation in Y-and Z-cut 0.67PbMgNbO₃–0.33PbTiO₃ single crystals. *Journal of applied physics.* 2009; 106:054110.
512. Hsu H-S, Zheng F, Li Y, Lee C, Zhou Q, Shung KK. Focused high frequency needle transducer for ultrasonic imaging and trapping. *Applied physics letters.* 2012; 101:024105.
513. Dong S. Review on piezoelectric, ultrasonic, and magnetoelectric actuators. *Journal of Advanced Dielectrics.* 2012:2.

514. Guo M, Dong S, Ren B, Luo H. A double-mode piezoelectric single-crystal ultrasonic micro-actuator. *Ultrasonics, Ferroelectrics and Frequency Control, IEEE Transactions on*. 2010; 57:2596–2600.
515. Shi Y, Zhao C, Huang W. Linear ultrasonic motor with wheel-shaped stator. *Sensors and actuators A: Physical*. 2010; 161:205–209.
516. Sashida T, Kenjo T. *Introduction to ultrasonic motors*. 1993
517. Uchino K. Materials issues in design and performance of piezoelectric actuators: an overview. *Acta Materialia*. 1998; 46:3745–3753.
518. Uchino K. Piezoelectric ultrasonic motors: overview. *Smart Materials and Structures*. 1998; 7:273.
519. Morita T. Miniature piezoelectric motors. *Sensors and Actuators A: Physical*. 2003; 103:291–300.
520. Guo M, Dong S, Ren B, Luo H. A piezoelectric single-crystal ultrasonic microactuator for driving optics. *Ultrasonics, Ferroelectrics and Frequency Control, IEEE Transactions on*. 2011:58.
521. Ci P, Chen Z, Liu G, Dong S. A square-plate piezoelectric linear motor operating in two orthogonal and isomorphic face-diagonal-bending modes. *Ultrasonics, Ferroelectrics and Frequency Control, IEEE Transactions on*. 2014; 61:159–165.
522. Hemsell T, Wallaschek J. Survey of the present state of the art of piezoelectric linear motors. *Ultrasonics*. 2000; 38:37–40. [PubMed: 10829624]
523. Li X, Wu Y, Chen Z, Wei X, Luo H, Dong S. Cryogenic motion performances of a piezoelectric single crystal micromotor. *Journal of Applied Physics*. 2014; 115:144103.

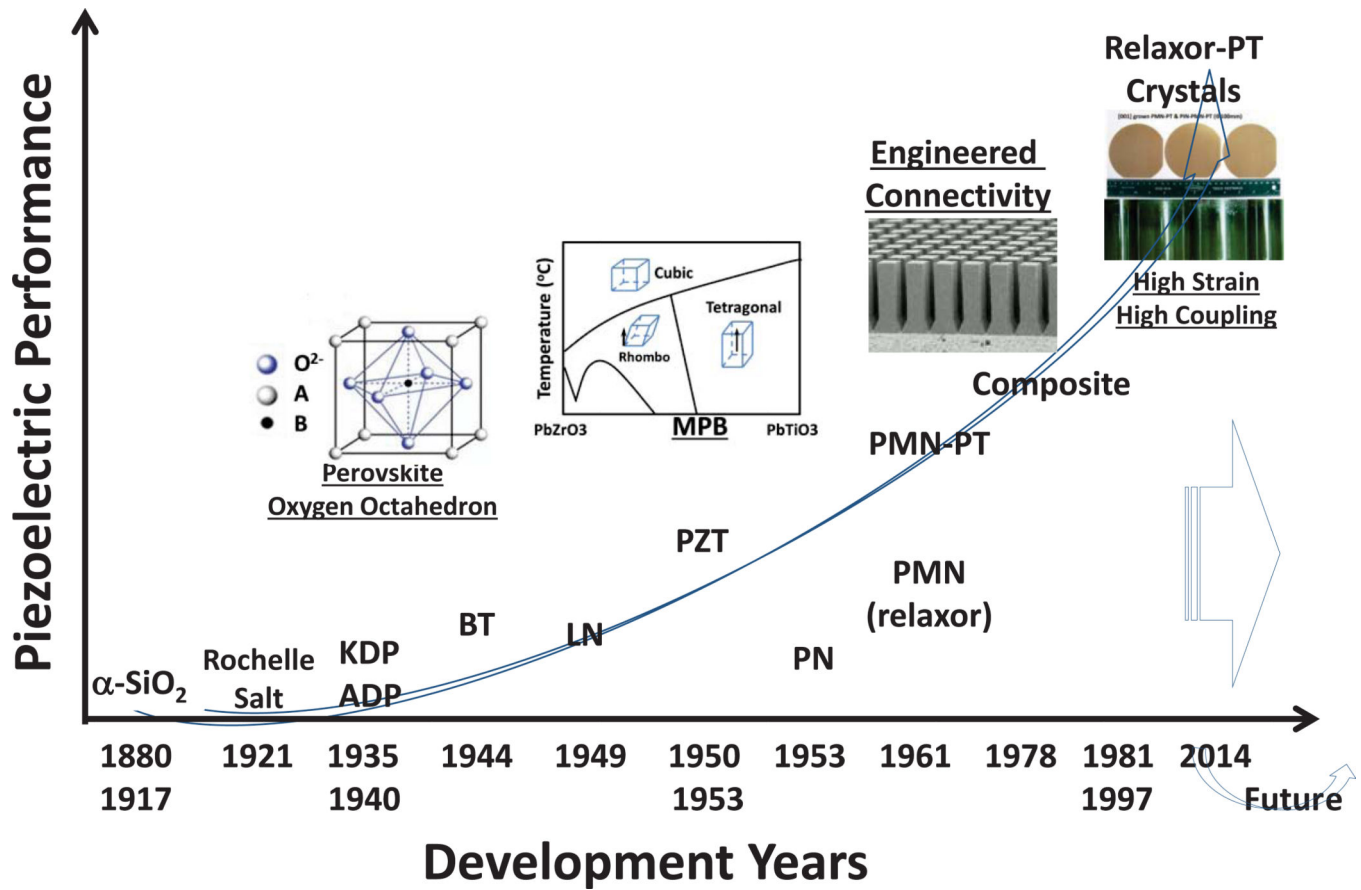
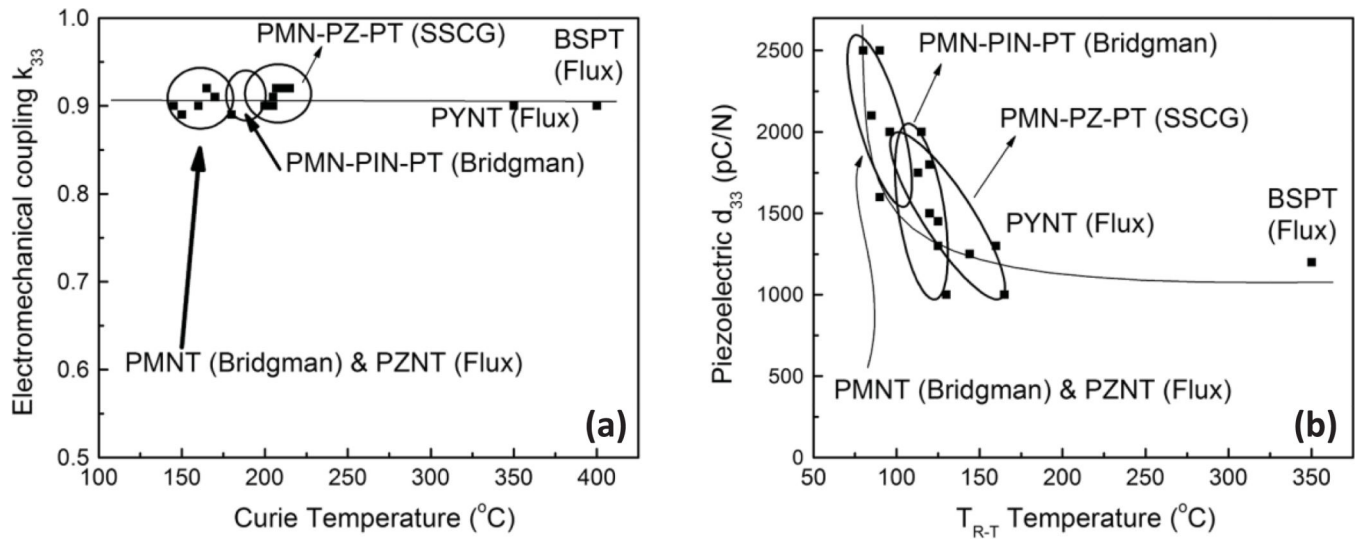


Fig. 1. General milestone map for piezoelectric transducer material development. KDP/ADP: $\text{KH}_2\text{PO}_4/(\text{NH}_4)\text{H}_2\text{PO}_4$; BT: BaTiO_3 ; LN: LiNbO_3 ; PZT: $\text{Pb}(\text{Zr},\text{Ti})\text{O}_3$; PN: PbNb_2O_6 ; PMN: $\text{Pb}(\text{Mg}_{1/3}\text{Nb}_{2/3})\text{O}_3$; PMN-PT: $\text{Pb}(\text{Mg}_{1/3}\text{Nb}_{2/3})\text{O}_3\text{-PbTiO}_3$.

**Fig. 2.**

(a) Electromechanical coupling of relaxor-PT crystals as a function of Curie temperature; (b) Piezoelectric coefficient of relaxor-PT crystals as a function of T_{RT} . BSPT: $\text{BiScO}_3\text{-PbTiO}_3$; PYNT: $\text{Pb}(\text{Yb}_{0.5}\text{Nb}_{0.5})\text{O}_3\text{-PbTiO}_3$. (Reprinted with permission from S. J. Zhang and T. R. Shrout, IEEE Transactions on Ultrasonics Ferroelectrics Frequency Control 57, 2138 (2010). Copyright© 2010, IEEE) [318]

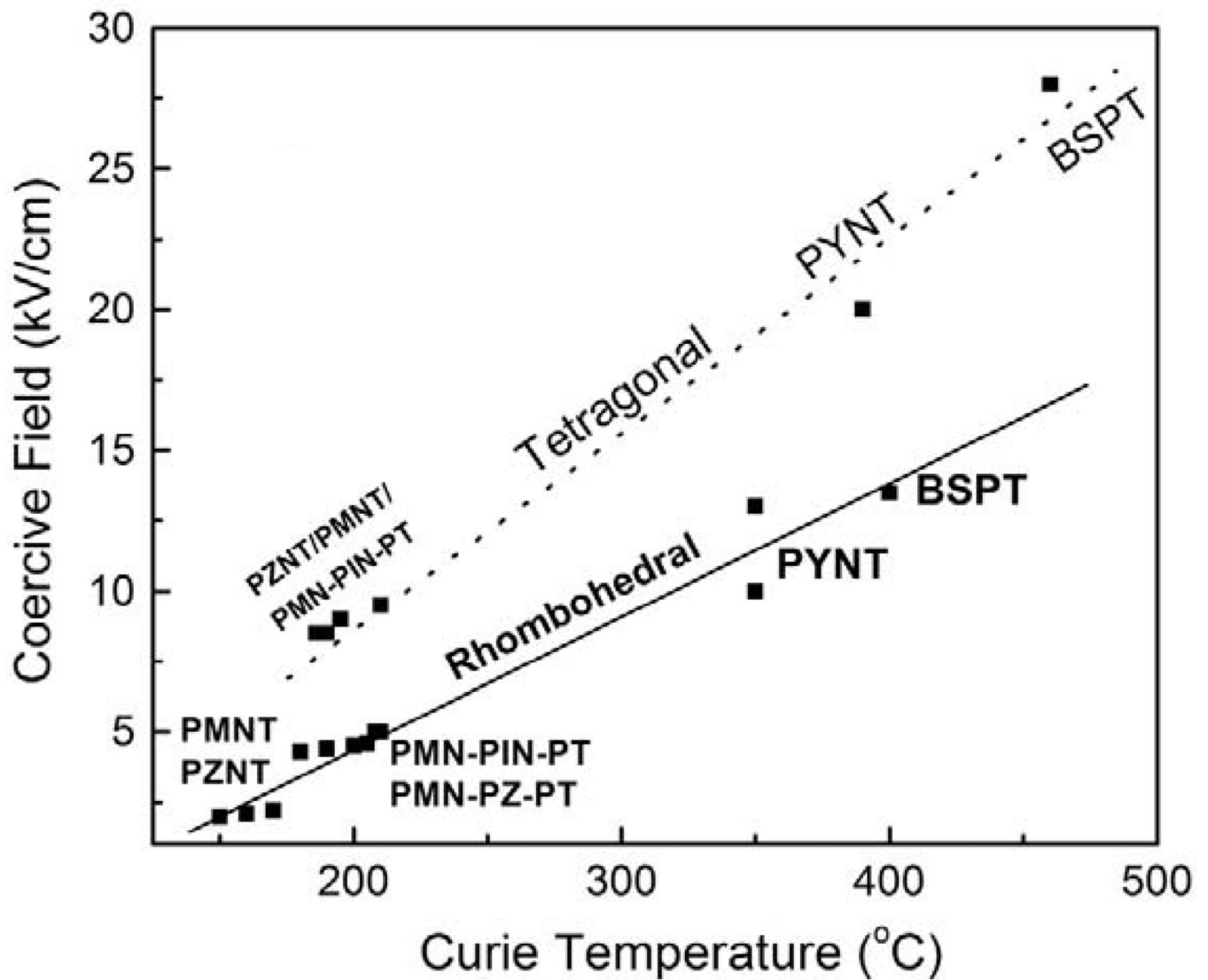


Fig. 3. Coercive field as a function of Curie temperature for perovskite relaxor-PT crystals. (Reprinted with permission from S. J. Zhang and T. R. Shrout, IEEE Transactions on Ultrasonics Ferroelectrics Frequency Control 57, 2138 (2010). Copyright© 2010, IEEE) [318].

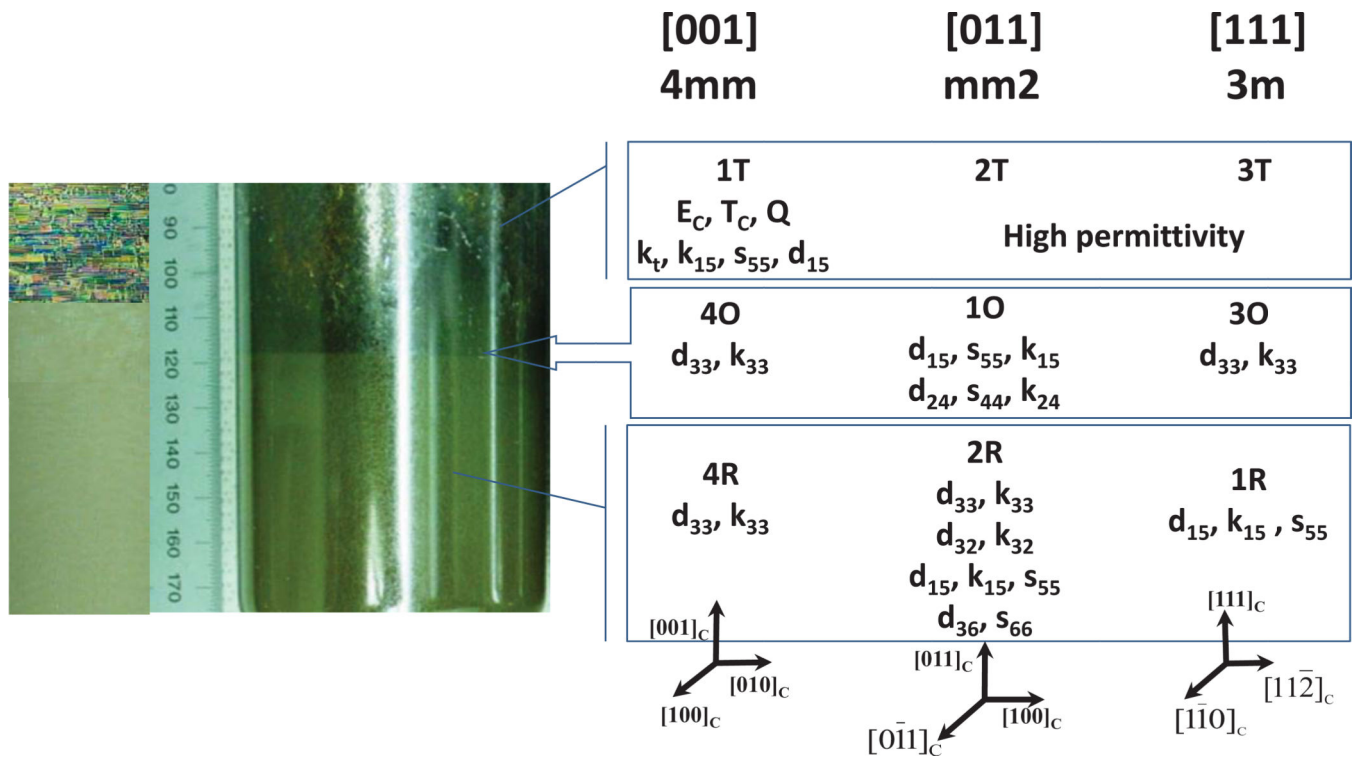


Fig. 4.

As grown relaxor-PT crystal (middle), domain observation under polarized light for unpoled crystal wafer with R, O and T phases (left), where there is no clear domain wall observed in R crystals, while cloudy and clear domain walls being observed in O and T crystals, respectively. The relevant macroscopic symmetries when poled along different crystallographic directions and the desirable properties corresponding to different domain configurations are listed in the figure (right).

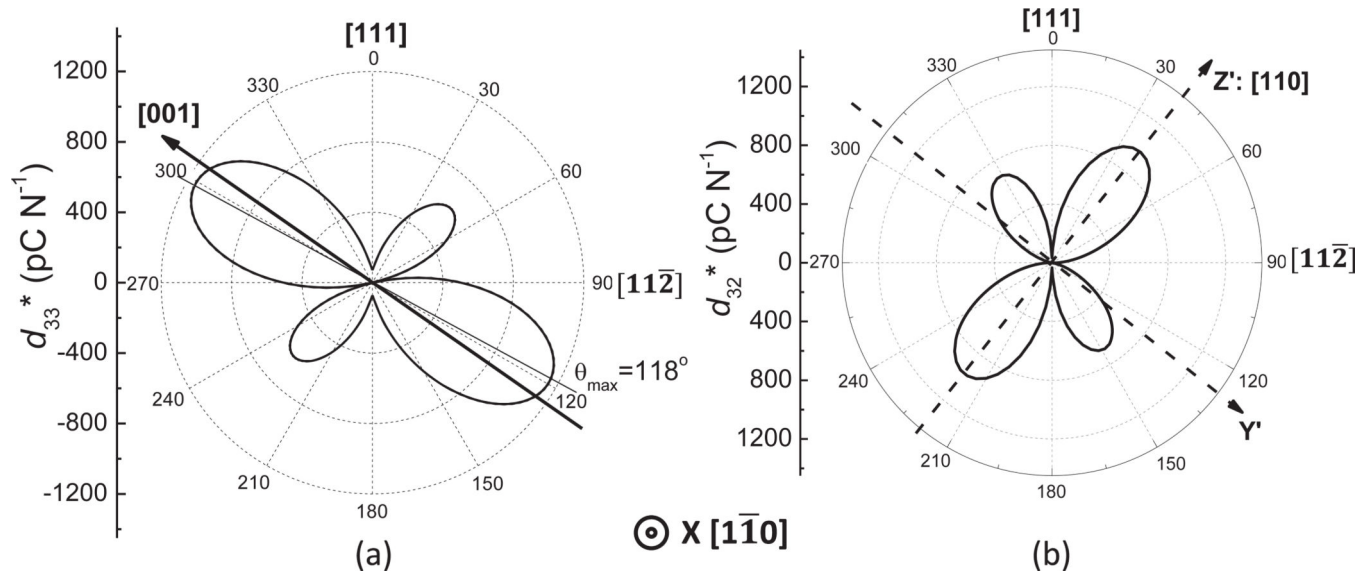


Fig. 5. Orientation dependence of the piezoelectric coefficient (left) d_{33}^* and (right) d_{32}^* for single domain PIN-PMN-PT crystals. For plotting the figures, the X axis is fixed along $[1\bar{1}0]$ direction, the Z and Y axis are rotated around X axis. It can be seen from figure (a) and (b) that the maximum piezoelectric coefficients of rhombohedral PIN-PMM-PT crystal are not presented in the standard coordinate system of $3m$ point group (X, Y, and Z axis are along $[1\bar{1}0]$, $[1\bar{1}\bar{2}]$ and $[111]$ direction, respectively). For d_{33}^* , the maximum value is observed when the Z' axis is rotated to $[001]$ direction. For d_{32}^* , the maximum value is presented in the coordinate system with Z' and Y' axis being along $[110]$ and $[001]$ directions, respectively.

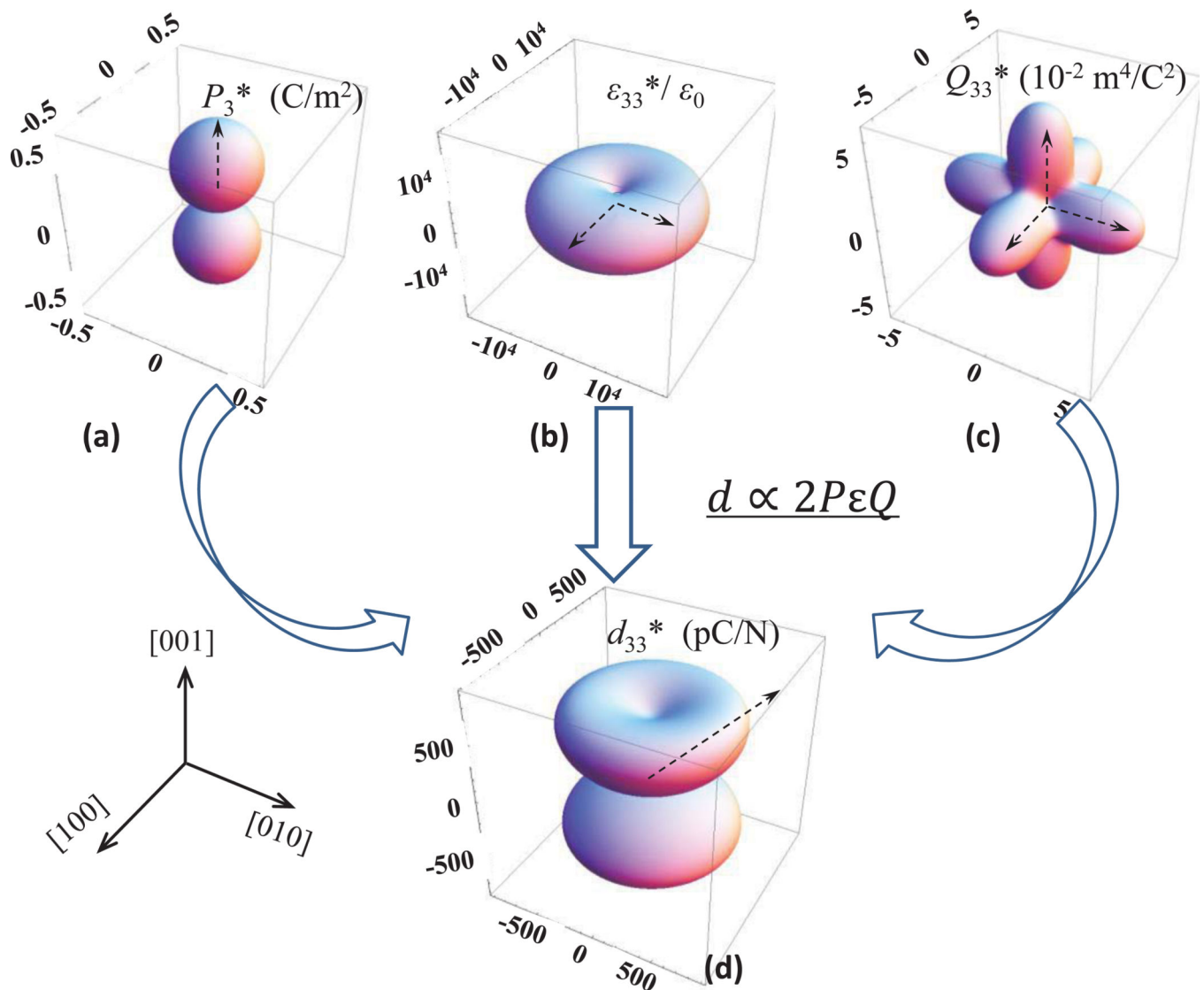


Fig. 6. The orientation dependence of the spontaneous polarization P_3^* , dielectric permittivity ϵ_{33}^* , electrostrictive coefficient Q_{33}^* and piezoelectric coefficient d_{33}^* for tetragonal PIN-PMN-PT crystals. Based on the equation $d \propto P\epsilon Q$, the orientation dependence of d_{33}^* is determined by orientation dependence of spontaneous polarization P_3^* , dielectric permittivity ϵ_{33} and electrostrictive coefficient Q_{33}^* . To obtain the coefficient value (Q_{33}^* , d_{33}^* , or ϵ_{33}^*) of one direction, a line along this direction should be plotted from the origin to surface of 3D figure. An intersection point can be found between the line and surface of 3D figure. The distance between this intersection point and the origin indicates the coefficient value along the direction of this line. (input data from ref. [293])

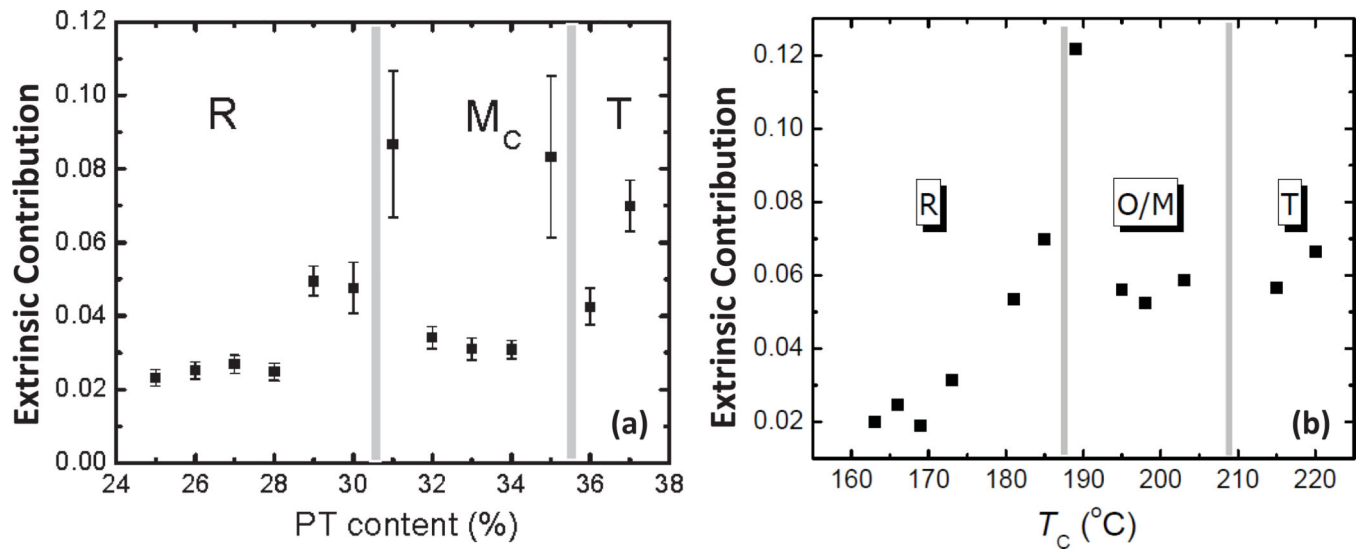
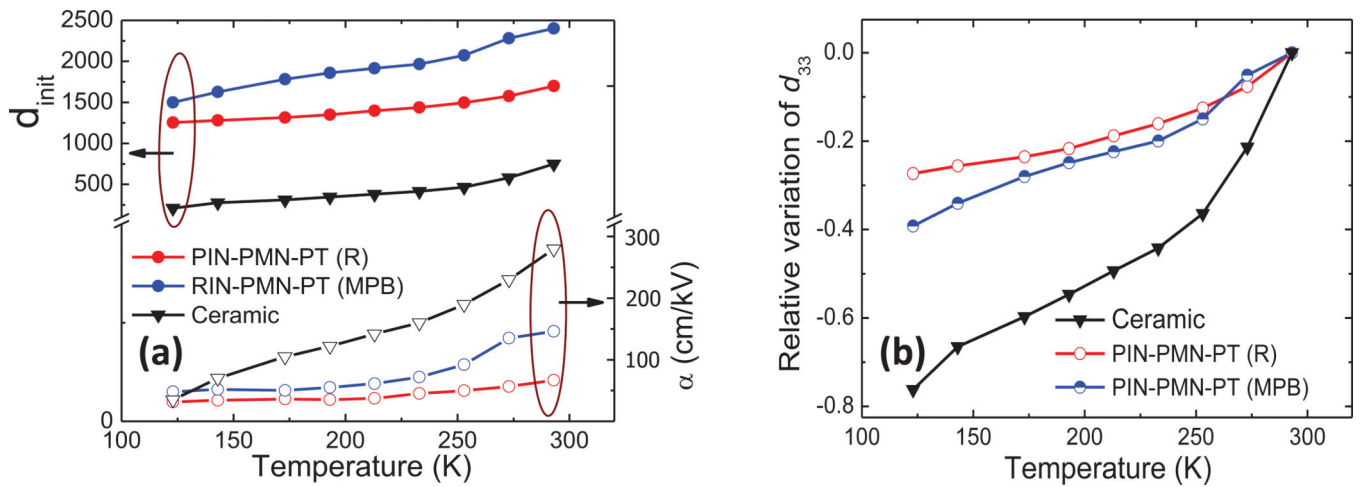


Fig. 7.

The level of extrinsic contribution to piezoelectric response at 1kV/cm for (a) (1-x)PMN-xPT crystals with various compositions [Reprinted with permission from F. Li et al., Journal of Applied Physics 108, 034106 (2010). Copyright © 2010, the American Institute of Physics.]; (b) PIN-PMN-PT crystals, where the increase of T_C represents the PT content increasing in PIN-PMN-PT crystals. Reprinted with permission from F. Li et al., Journal of Applied Physics 109, 014108 (2011). Copyright © 2011, the American Institute of Physics.

**Fig. 8.**

(a) The temperature dependent Rayleigh parameters, (b) Variation of d_{33} as a function of temperature for [001] poled PIN-PMN-PT crystals and PMN-PT ceramics. (data from ref. [363])

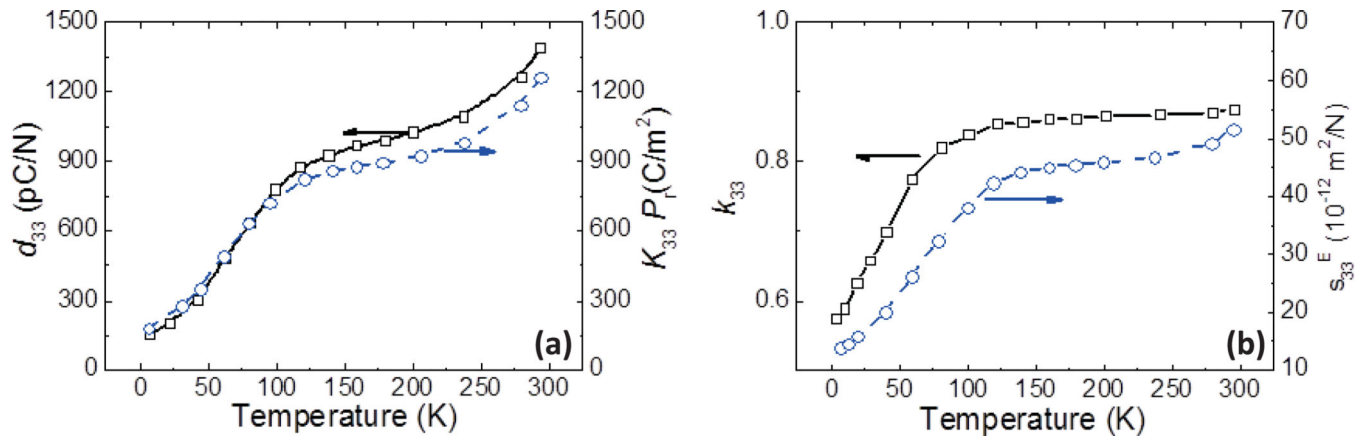


Fig. 9.

Temperature dependence of d_{33} and $K_{33}P_r$; (b) Temperature dependence of k_{33} and s_{33}^E for PMN-0.28PT crystals. (Reprinted with permission from F. Martin et al., Journal of Applied Physics 111, 104108 (2012). Copyright © 2012, the American Institute of Physics. [365])

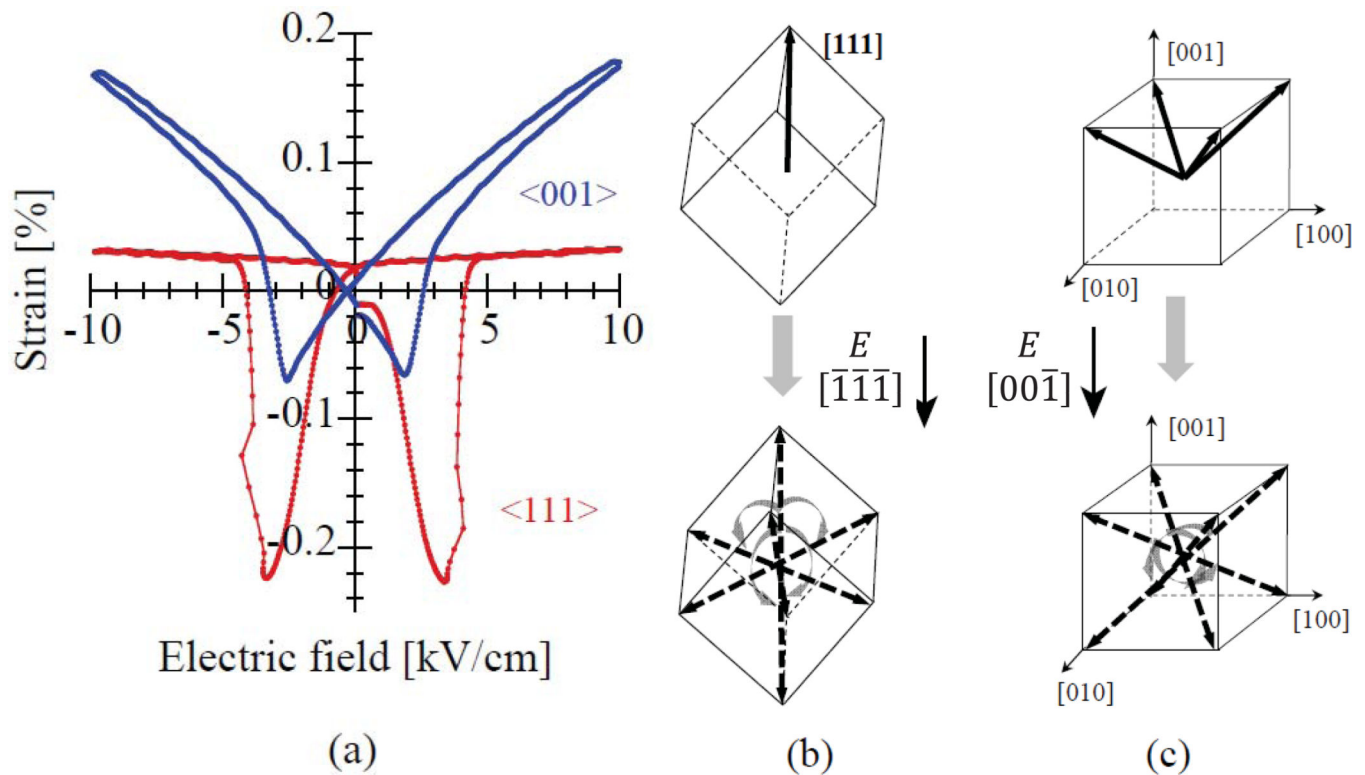


Fig. 10.

(a) Strain versus electric field curves for PMN-0.29PT crystals measured along $[001]$ and $[111]$ directions at room temperature. (b) Schematic illustration of the domain switching for rhombohedral crystal. (b) $[111]$ oriented crystal. At the coercive, which is antiparallel to the $[111]$ direction, $[111]$ domain could transform to the $[111]$, $[1\bar{1}\bar{1}]$, $[\bar{1}1\bar{1}]$, $[\bar{1}\bar{1}1]$, $[11\bar{1}]$, and $[\bar{1}11]$ domains, (c) $[001]$ oriented crystal. At the coercive, which is antiparallel to the $[001]$ direction, $[111]$, $[111]$, $[1\bar{1}\bar{1}]$ and $[\bar{1}\bar{1}1]$ domains transform to the $[111]$, $[1\bar{1}\bar{1}]$, $[\bar{1}1\bar{1}]$, and $[\bar{1}\bar{1}1]$ domains). Reprinted with permission from L. Jin et al. Journal of the American Ceramic Society 97, 1 (2014) Copyright © 2014, The American Ceramic Society. [42]

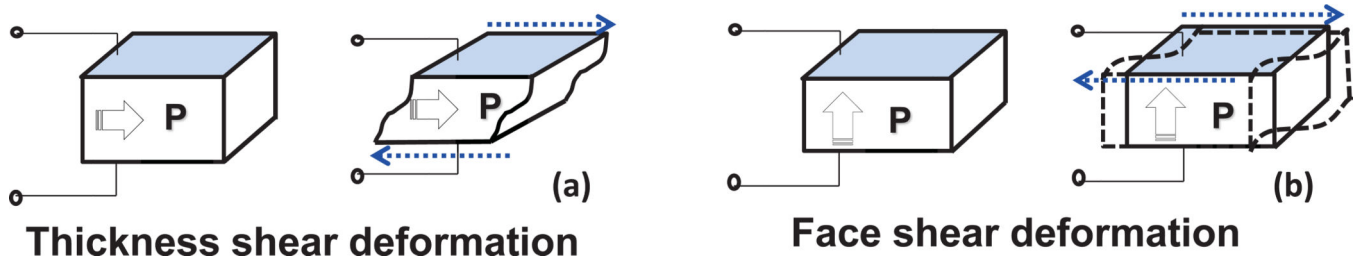


Fig. 11.

(a) Schematic figure of thickness shear piezoelectric deformation, (b) Schematic figure of face shear piezoelectric deformation. P is the poling direction. It should be noted that the resonance frequency is controlled by the thickness of the piezoelectric element in thickness shear deformation, while it is controlled by the edge length of the element in face shear deformation. Reprinted with permission S.J. Zhang *et al.* IEEE Transactions on Ultrasonics Ferroelectrics Frequency Control 60, 1572 (2013) Copyright © 2013, IEEE. [374]

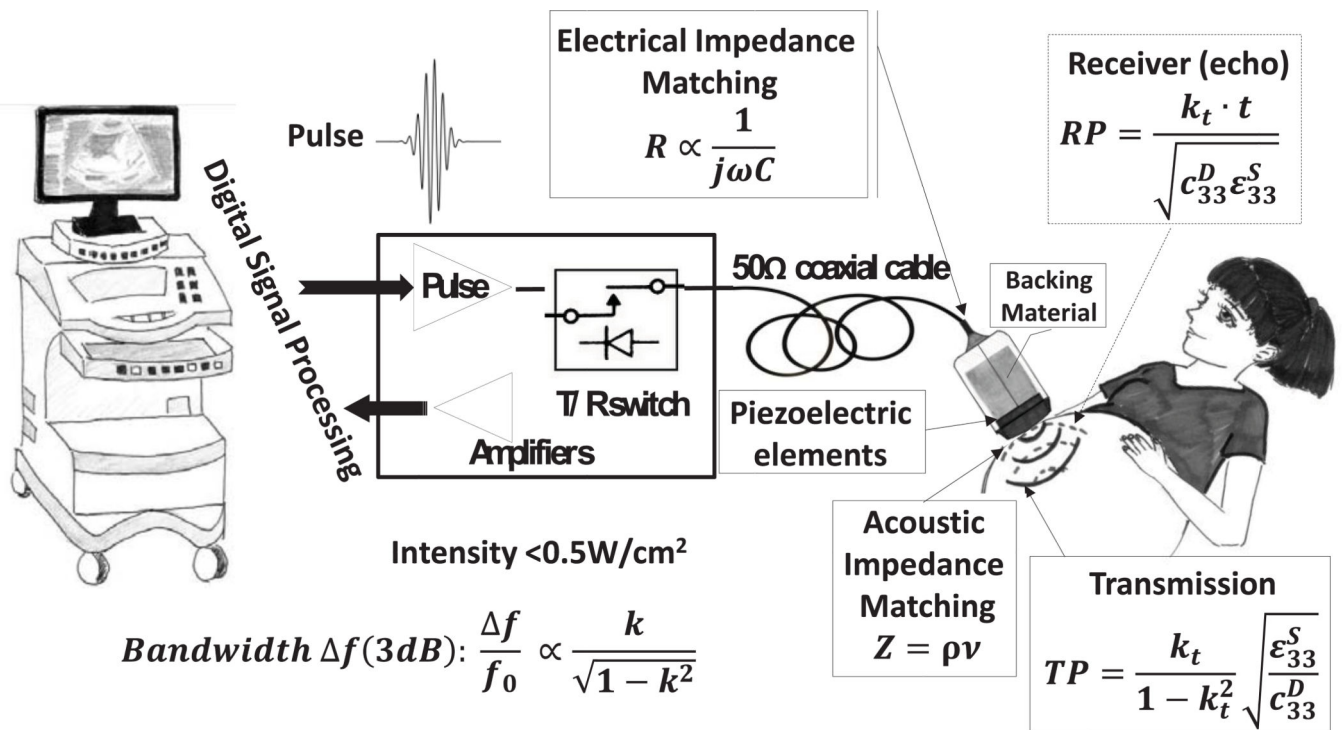
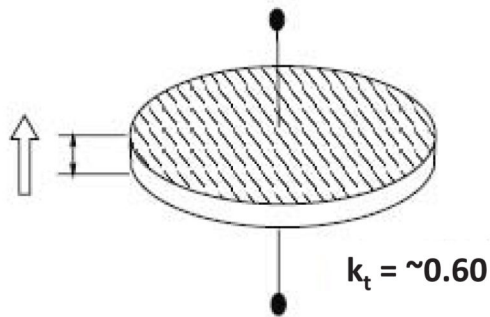


Fig. 12. Schematic view of the medical imaging system and the operational mechanism. The equations are from references [3,385]. k : coupling; ϵ_{33}^S : clamped dielectric, c_{33}^D : elastic stiffness, ρ : density, v : sound velocity, R : electrical impedance, C : capacitance, Z : acoustic impedance.

Monolithic Thickness Mode



Composite Thickness Mode

1-3 composite

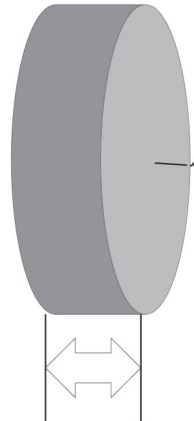
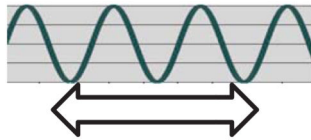


2-2 composite



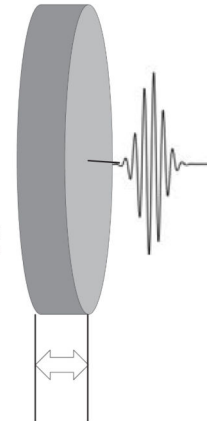
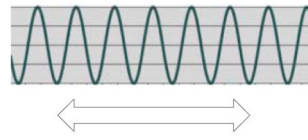
Fig. 13. The comparison of various vibration modes of relaxor-PT crystals and their corresponding electromechanical coupling values.

Low Frequency Transducer



Thick

High Frequency Transducer



Thin

$$C = \epsilon A / t$$

$$c^D = \rho v^2$$

$$v = 2f_a \cdot t$$

$$\lambda = \frac{v}{f}$$

Medical Imaging Frequencies

Abdomen	2.5-3.5MHz
Vascular, Brest (Gyn)	5MHz
Echocardiography	2-7MHz
Brest, Thyroid	7.5-10MHz
Superficial veins	10MHz
Ophthalmic	10-60MHz
Intravascular	20-80MHz
Skin	20- >100MHz

$$Resolution \propto 1/\lambda \text{ @ constant } \Delta f \text{ and } f(\text{number})$$

Fig. 14. Medical imaging transducer operational frequency and the corresponding imaging human tissues. The equations are from [391]. *C*: capacitance; *A*: sample area; *t*: sample thickness; *f_a*: antiresonance frequency; *c^D*: elastic stiffness; *v*: sound velocity; *λ*: wavelength; *f*: frequency.

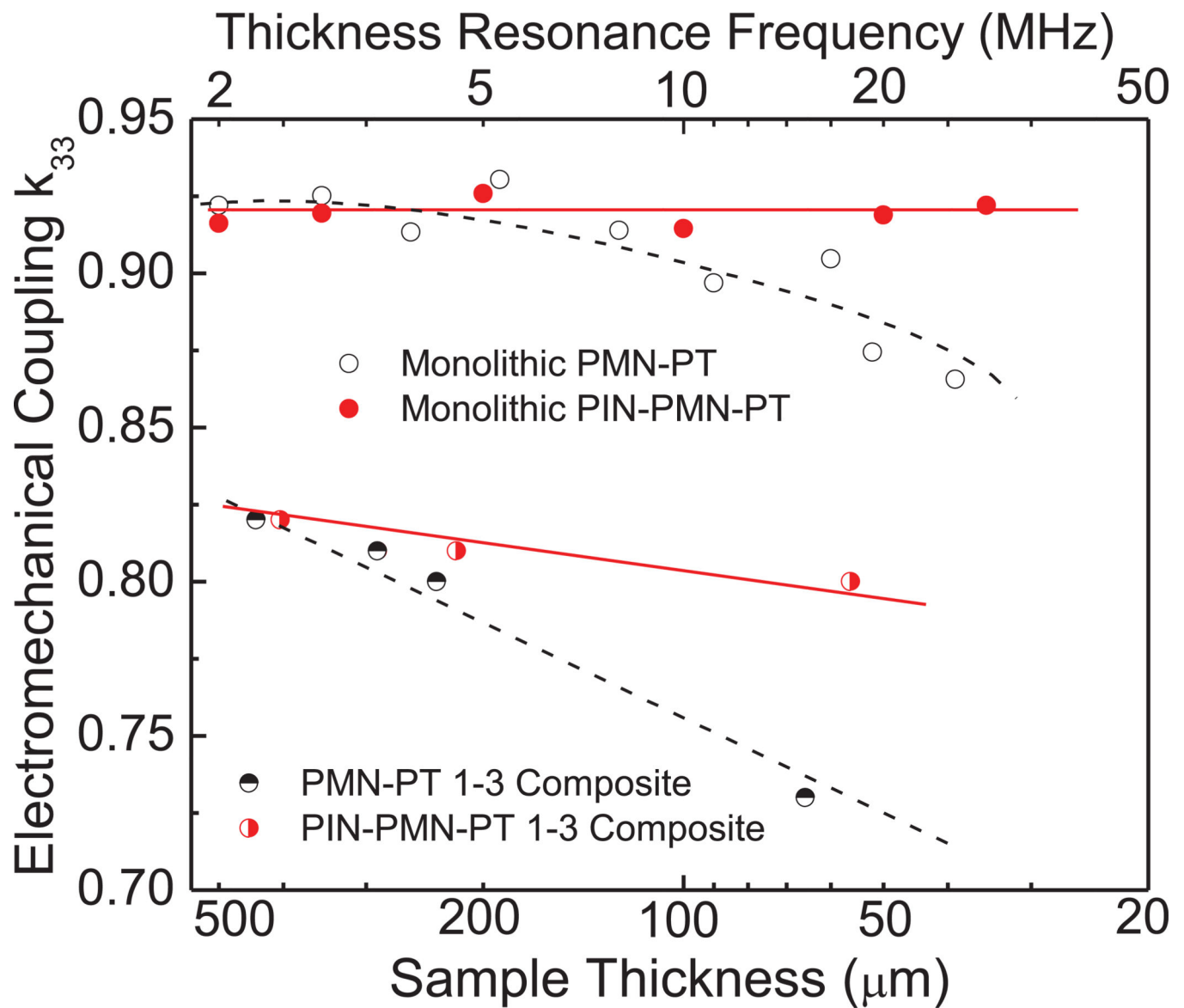


Fig. 15. Electromechanical coupling factor for monolithic and crystal/epoxy 1–3 composites as a function of sample thickness and corresponding ultrasound frequency. Reprinted with permission from H. J. Lee et al., *Journal of Applied Physics* 107, 124107 (2010). Copyright © 2010, the American Institute of Physics. [405]

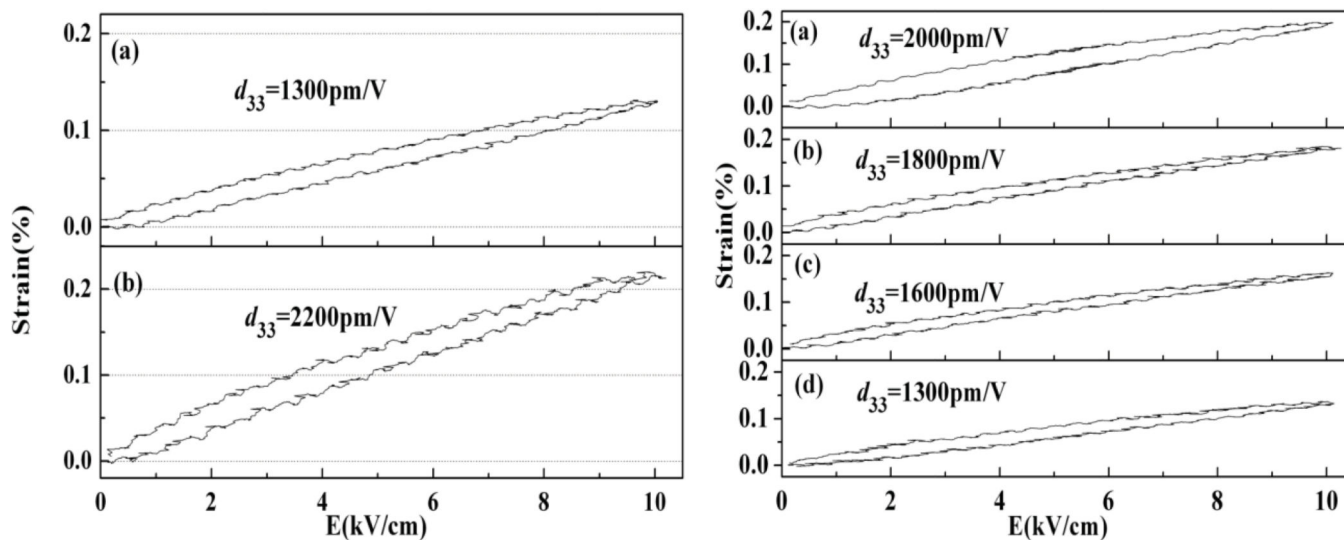


Fig. 16.

Left: Unipolar strain as a function of electric field for room temperature poled (a) and field cooling poled (b) [001] oriented PMN-PT crystals (with thickness of 100 μm); Right: the unipolar strain behavior after pulse tests (a) 3 kV/cm, 7×10^5 cycles, (b) 3 kV/cm, 7×10^7 cycles, (c) 6 kV/cm, 7×10^5 cycles, (d) 6 kV/cm, 1.5×10^6 cycles. Reprinted with permission from D. B. Lin *et al.* Scripta Materialia 64, 1149 (2011), Copyright © 2011, Acta Materialia Inc. [198]

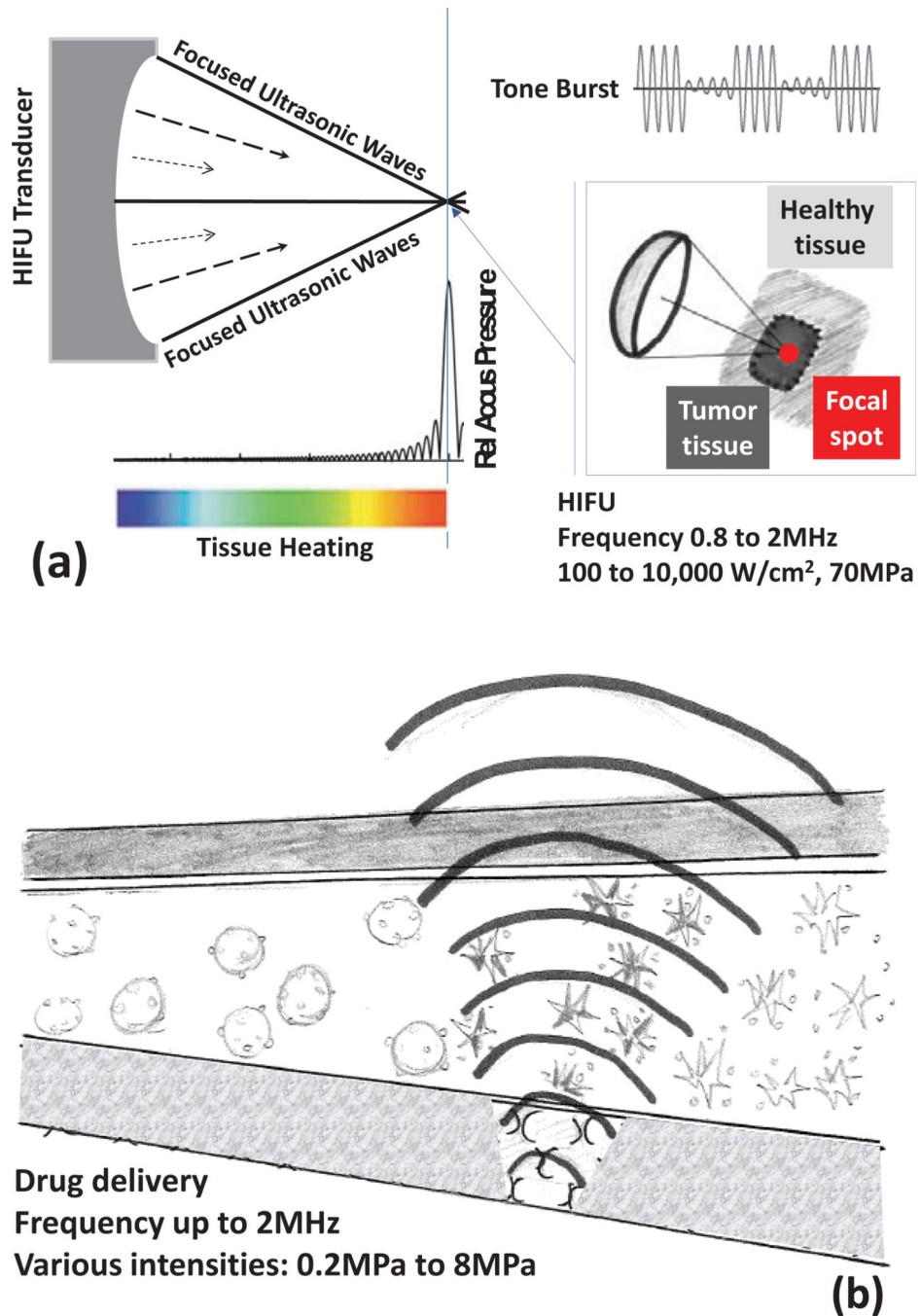


Fig. 17. The basic principles of HIFU producing tissue necrosis (a), Operational mechanism for drug delivery using ultrasound waves (b).

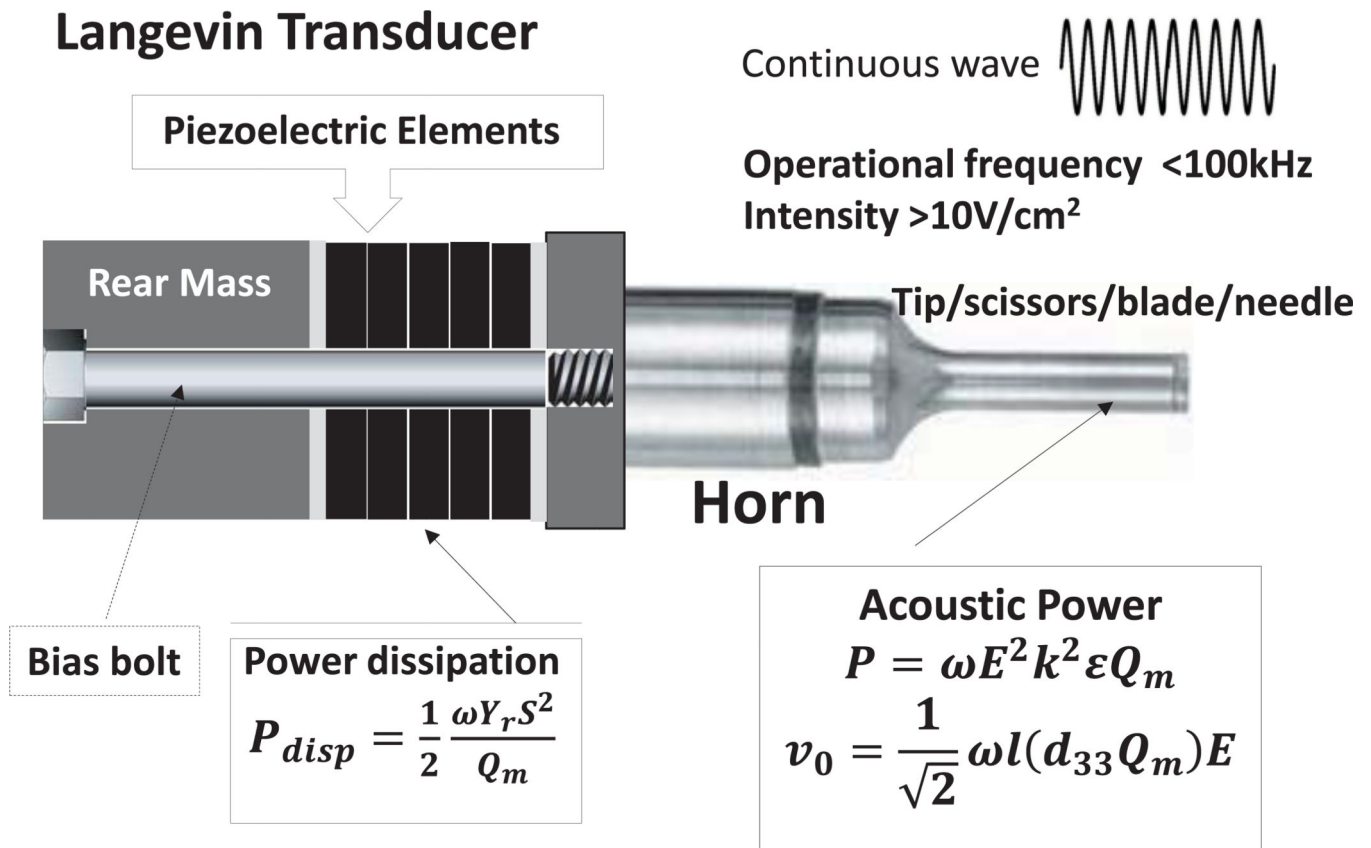


Fig. 18. Langevin transducer with a horn for medical surgery applications. Equations are from [3,10,388]. P_{disp} : dissipated power; ω : angular frequency; Y_r : Young's modulus; S : strain; Q_m : mechanical quality factor; k : electromechanical coupling; d : piezoelectric coefficient; v_0 : vibration velocity at the horn tip; P : acoustic power; ε : dielectric permittivity; E : electric field.

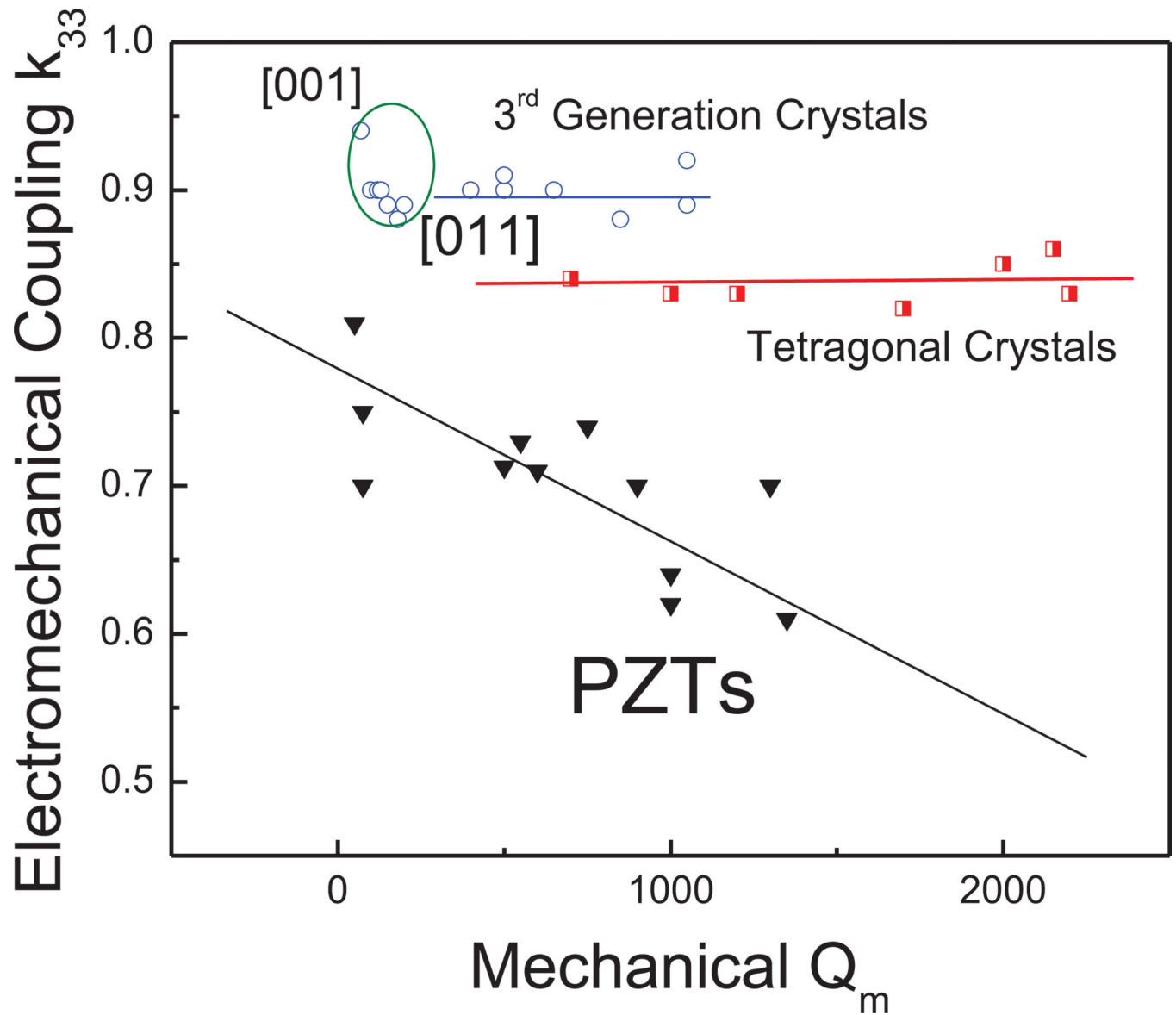


Fig. 19. The relationship between mechanical Q_m and electromechanical coupling factor for different polycrystalline and single crystal systems. Reprinted with permission from S. J. Zhang and T. R. Shrout, IEEE Transactions on Ultrasonics Ferroelectrics Frequency Control 57, 2138 (2010). Copyright© 2010, IEEE [318]

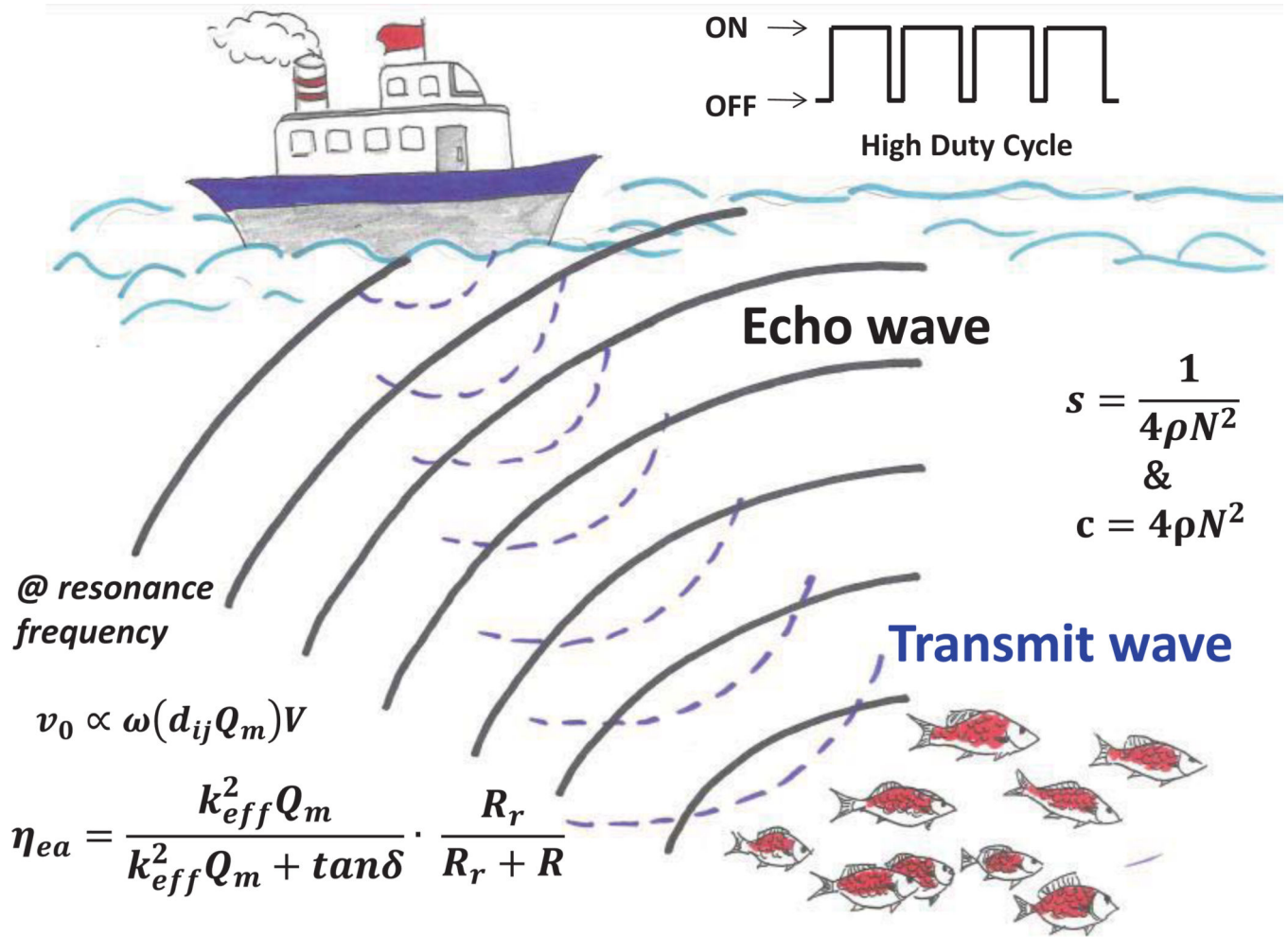


Fig. 20.

Schematic figure for underwater electroacoustic transducer applications, locating a large school of fish. Equations are from [3]. R_r : radiation resistance; R : internal mechanical resistance; v_0 : vibration velocity at transducer surface; η_{ea} : electroacoustic efficiency; k_{eff} : electromechanical coupling; Q_m : mechanical quality factor; s : elastic compliance; c : elastic stiffness; ρ : density; N : frequency constant; V : voltage; d : piezoelectric coefficient.

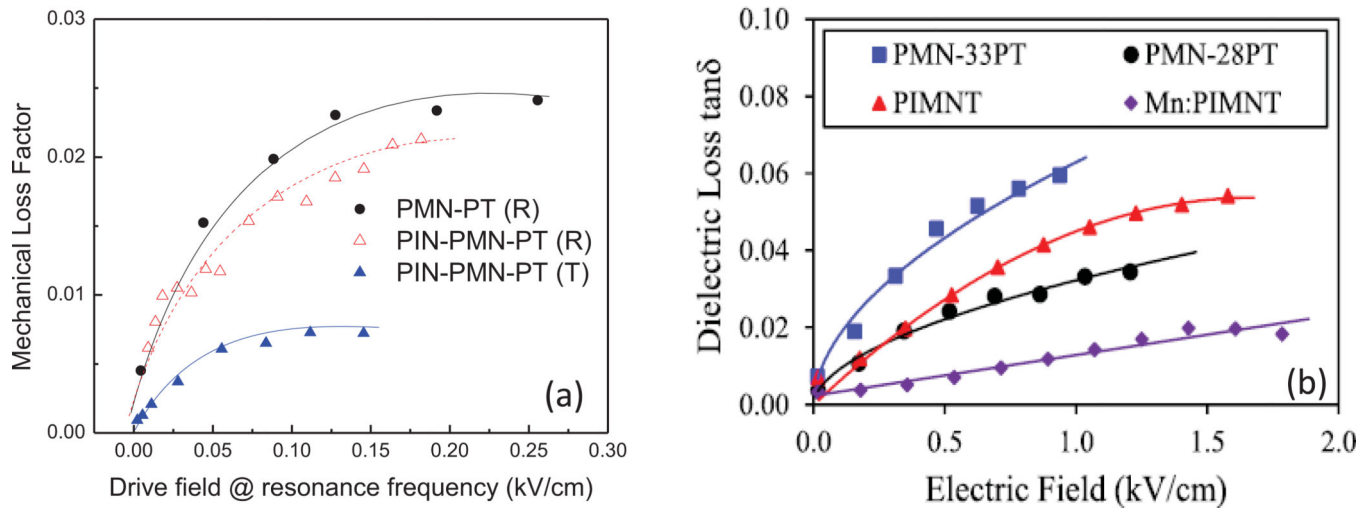


Fig. 21.

(a) Mechanical loss factor (inverse of mechanical Q_m) of various relaxor-PT crystals as a function of drive field at resonance frequency. Reprinted with permission from S. J. Zhang and F. Li, *Journal of Applied Physics* 111, 031301 (2012). Copyright © 2012, the American Institute of Physics. [141] (b) Dielectric loss of various relaxor-PT crystals as a function of drive field at 1Hz. Reprinted with permission from N. Sherlock, L. Garten, S. Zhang, T. Shrout and R. Meyer, *Journal of Applied Physics* 112, 124108 (2012). Copyright © 2012, the American Institute of Physics. [429].

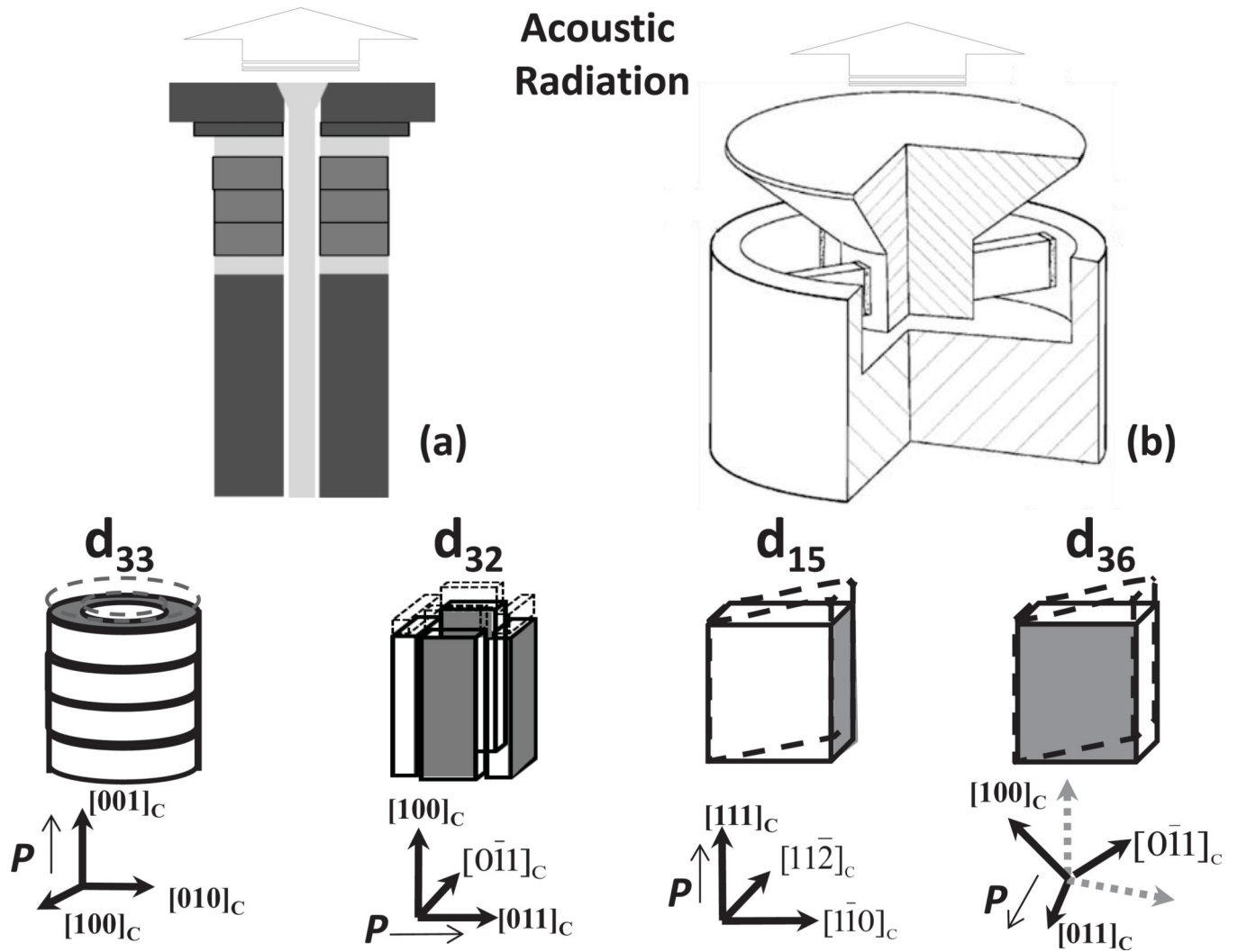


Fig. 22. Schematic figures of acoustic transducers with various geometries. The piezoelectric elements with different vibration mechanisms used in these transducers are given at the bottom, P : poling direction; ■: Electrodes on piezoelectric elements. (Figures adapted from ref. [10, 376])

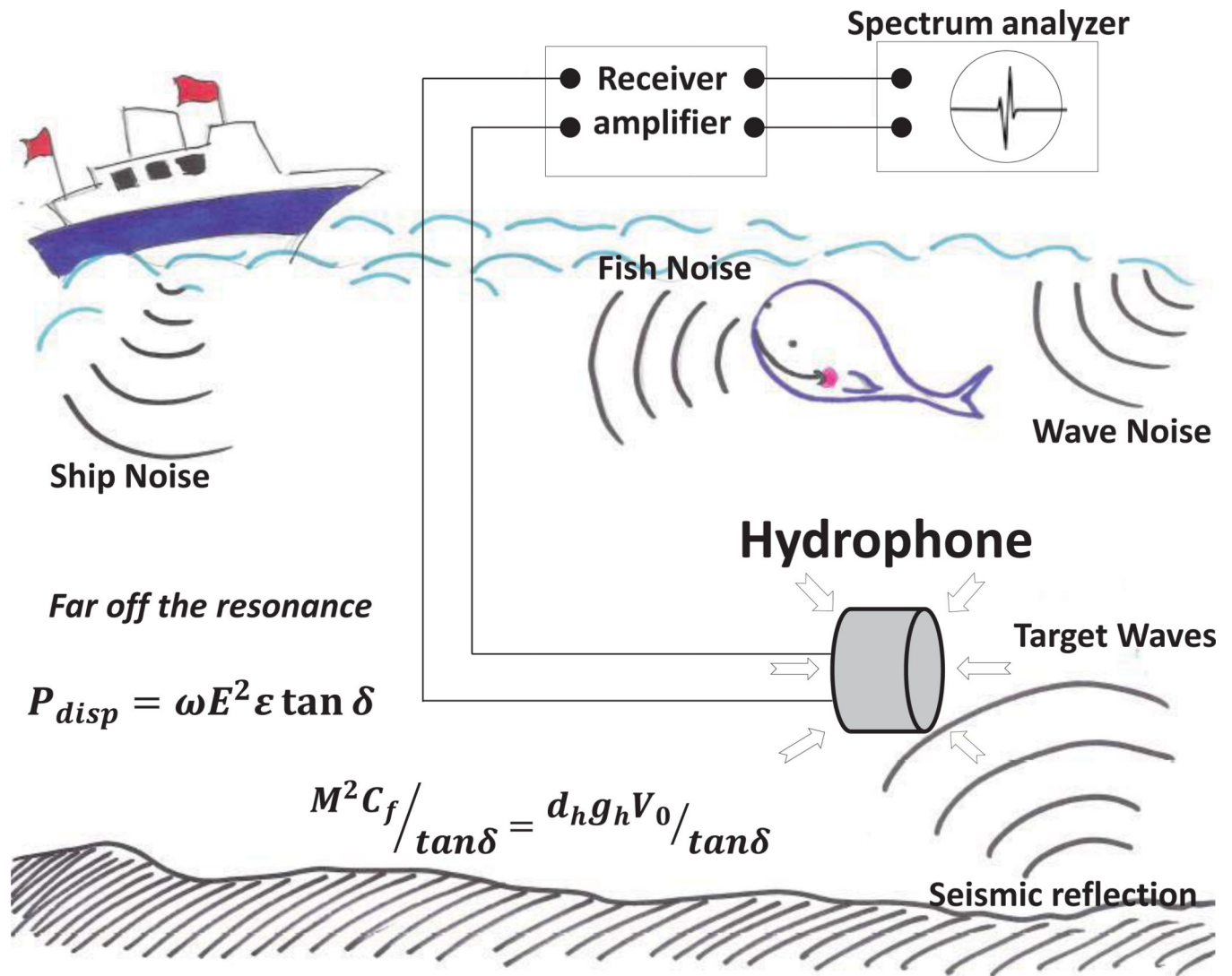


Fig. 23. Schematic of hydrophone operational mechanism. Equations are from [3,10]. P_{disp} : dissipated power; $\tan \delta$: dielectric loss; ω : angular frequency; E : electric field; ε : dielectric constant; d_h : hydrostatic piezoelectric charge coefficient; g_h : hydrostatic piezoelectric voltage coefficient; V_0 : volume of the sensing material.

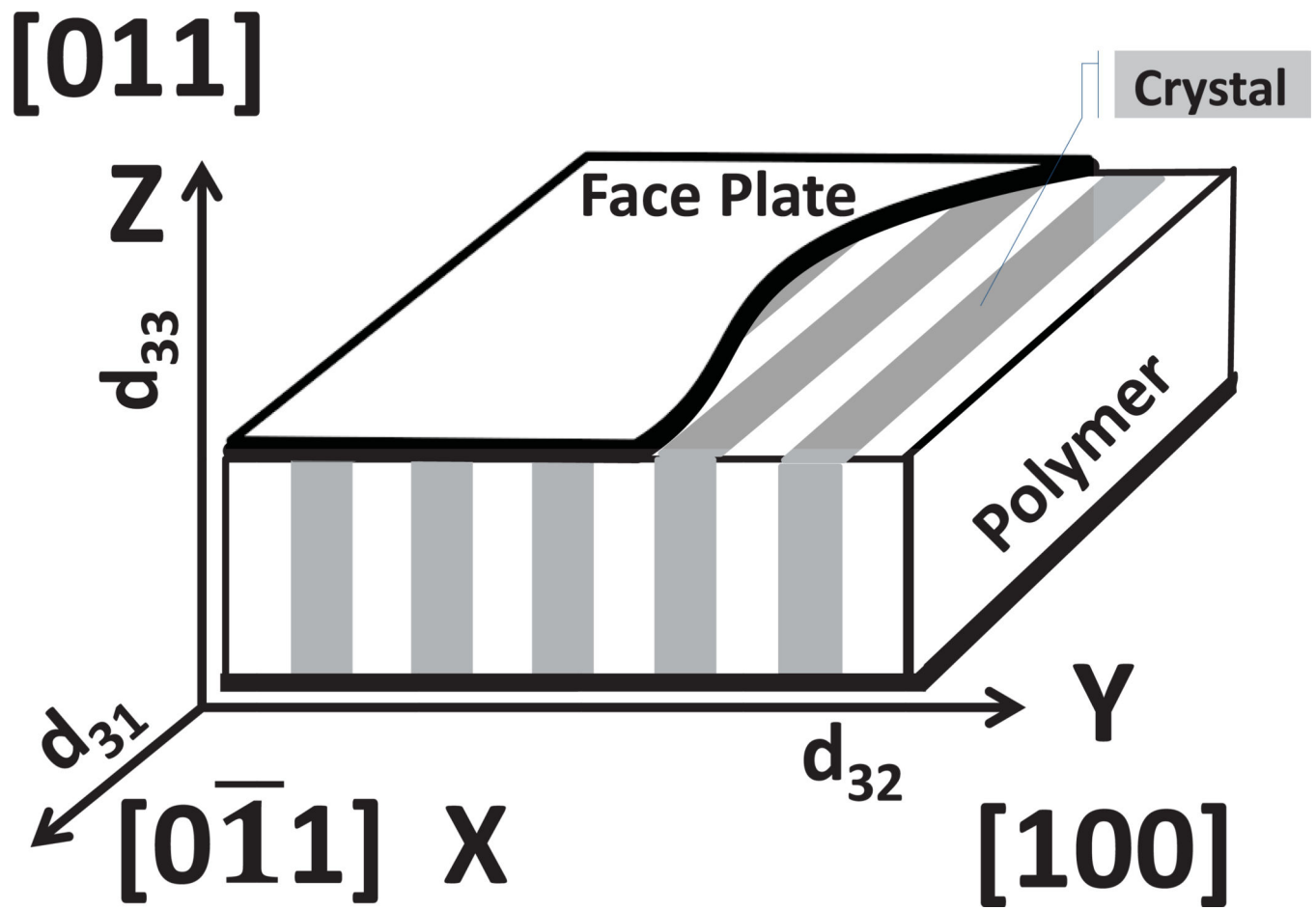
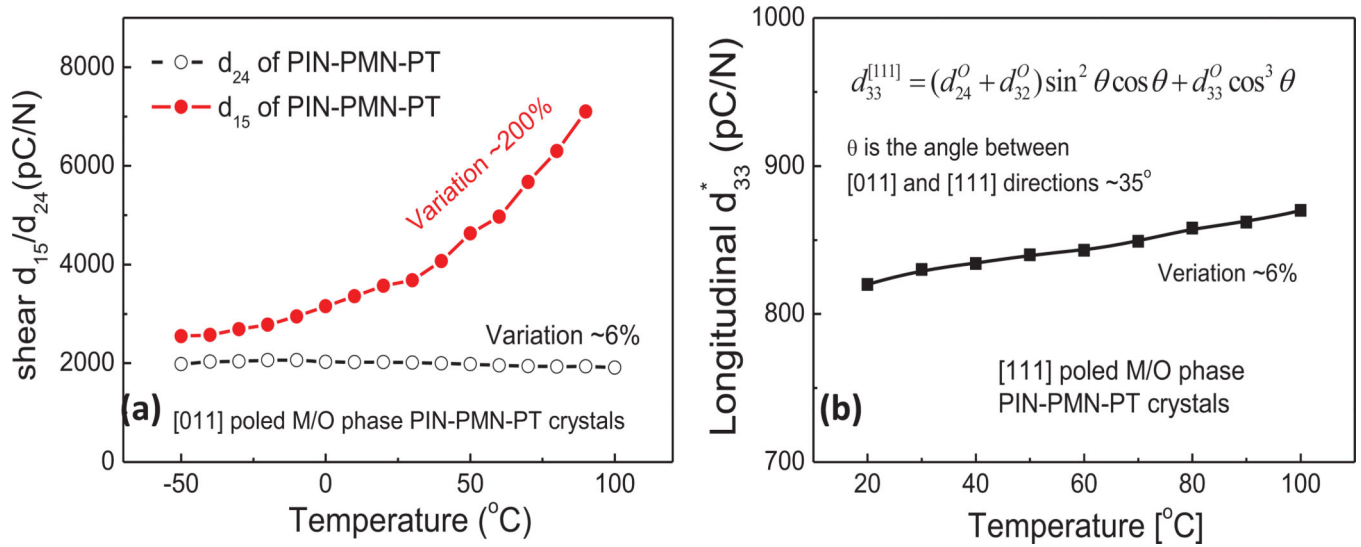


Fig. 24. Schematic diagram of 2-2 crystal/epoxy composite comprised of $[011]$ poled relaxor-PT single crystals, with layers parallel to X axis. (Figure adapted from ref. [99])

**Fig. 25.**

(a) Temperature dependent shear piezoelectric coefficients for PIN-PMN-PT crystals with “1O” single domain state (data from [339–340]), (b) Temperature dependent longitudinal piezoelectric coefficient for PIN-PMN-PT crystals with “3O” engineered domain configuration (data from [141]).

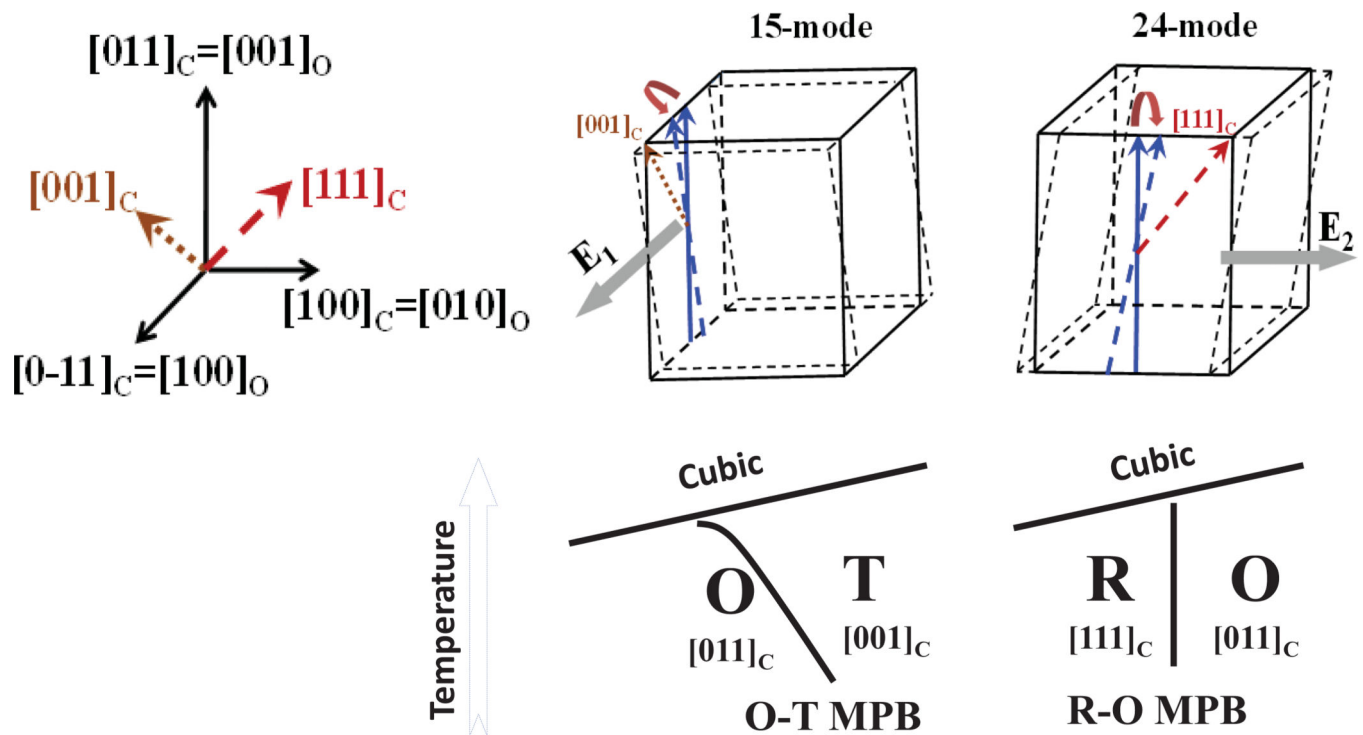


Fig. 26.

Two independent shear piezoelectric responses (15- and 24-mode) and related polarization rotation path in orthorhombic crystals, where the solid and dotted blue arrows represent the polarization rotation process under perpendicular electric field. The coordinate system of orthorhombic crystal is presented on the left. The principal axis of orthorhombic phase are notated as $[001]_o$, $[010]_o$ and $[100]_o$, being equal to $[011]_c$, $[0-11]_c$ and $[100]_c$ cubic axis, respectively (adapted from [339]). The related phase diagram exhibiting strongly curved O-T MPB and vertical R-O MPB were given at the bottom of the figure.

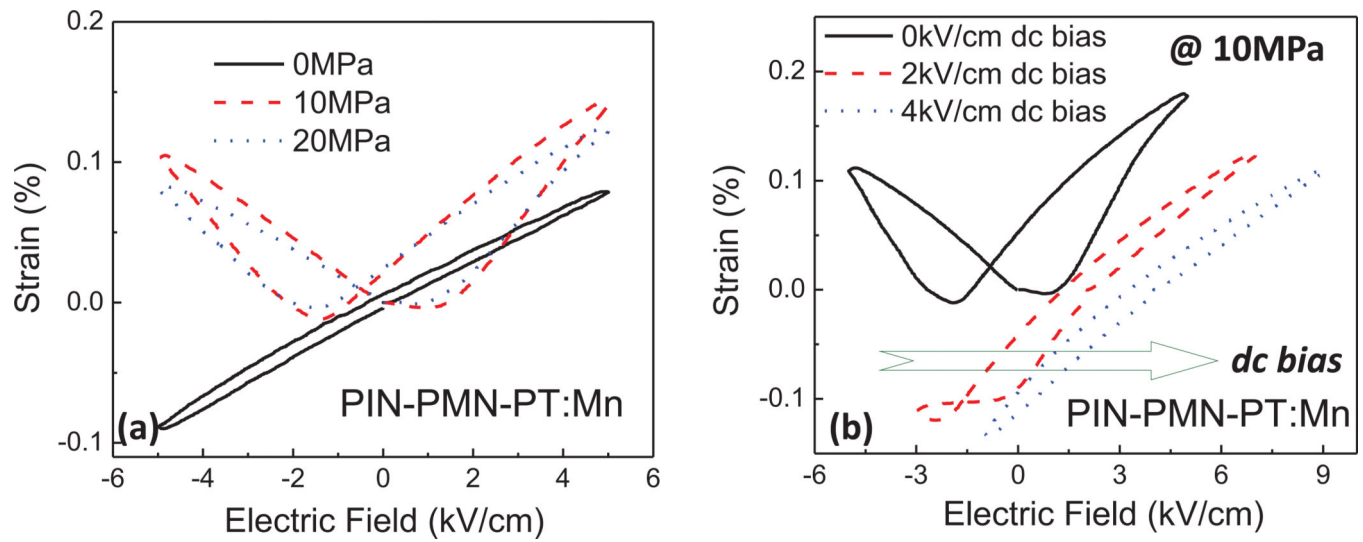


Fig. 27.

Strain electric field loops for PIN-PMN-PT:Mn (a) as a function of applied compressive prestress, (b) measured at 10MPa prestress and as a function of dc bias. (data from [452])

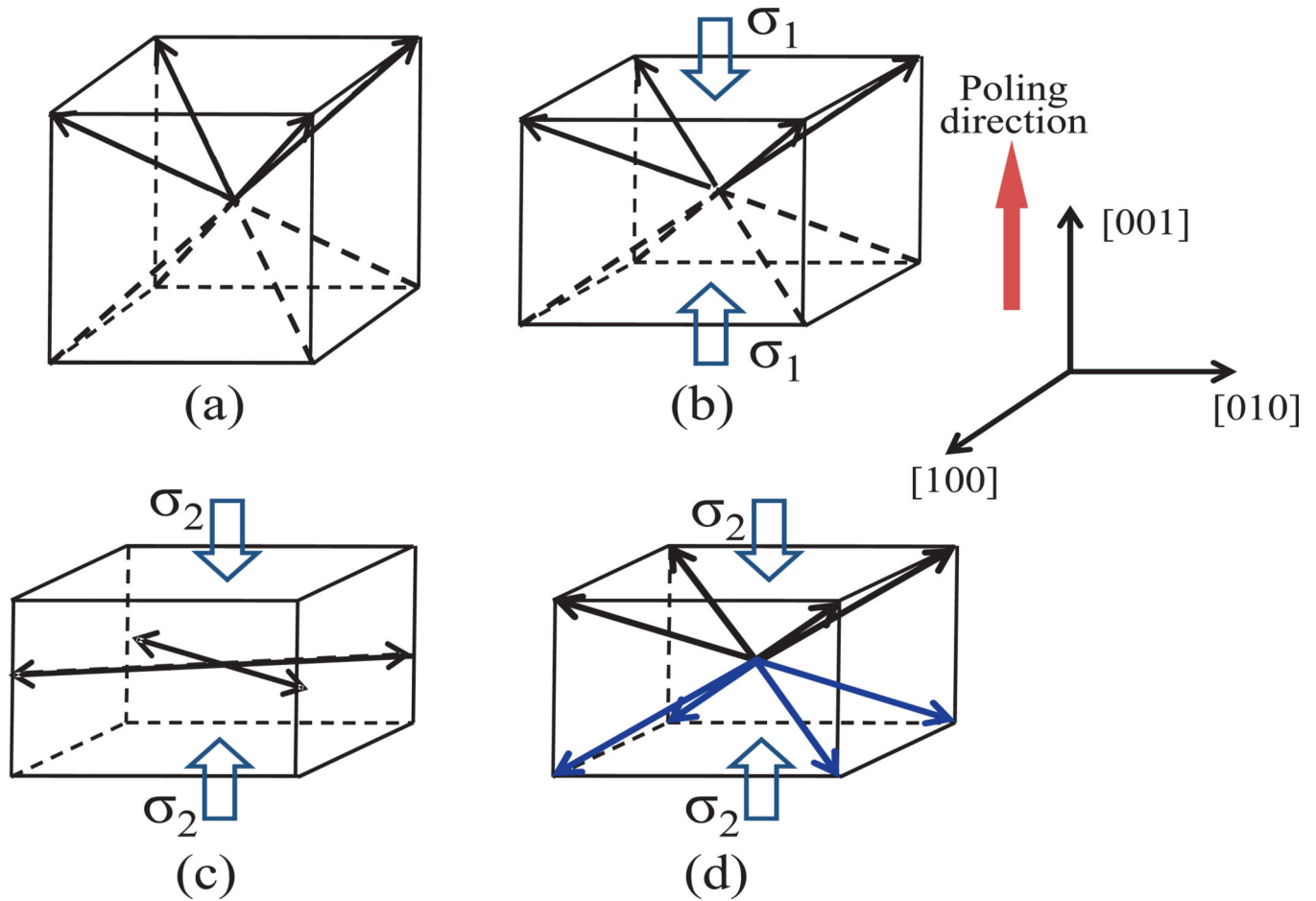


Fig. 28.

Schematic of domain variation for [001] poled rhombohedral relaxor-PT crystal under uniaxial stress. (a) original state for [001] poled rhombohedral relaxor-PT crystal, where the solid arrows represent the possible domain directions. (b) under a moderate uniaxial stress. (c) and (d) show the two possible conditions of domain variation under a strong stress. For (c), the rhombohedral domains are transformed to orthorhombic domains by applying a stress. For condition (d), rhombohedral crystal is depolarized by the stress, where the blue arrows represent the new domain directions.

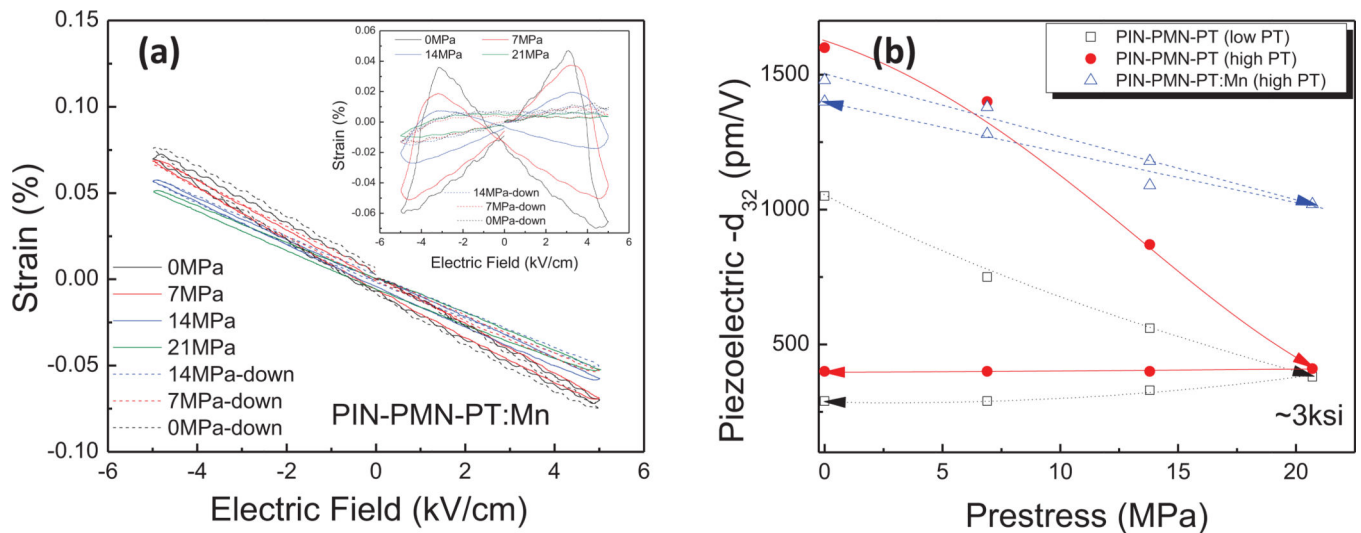
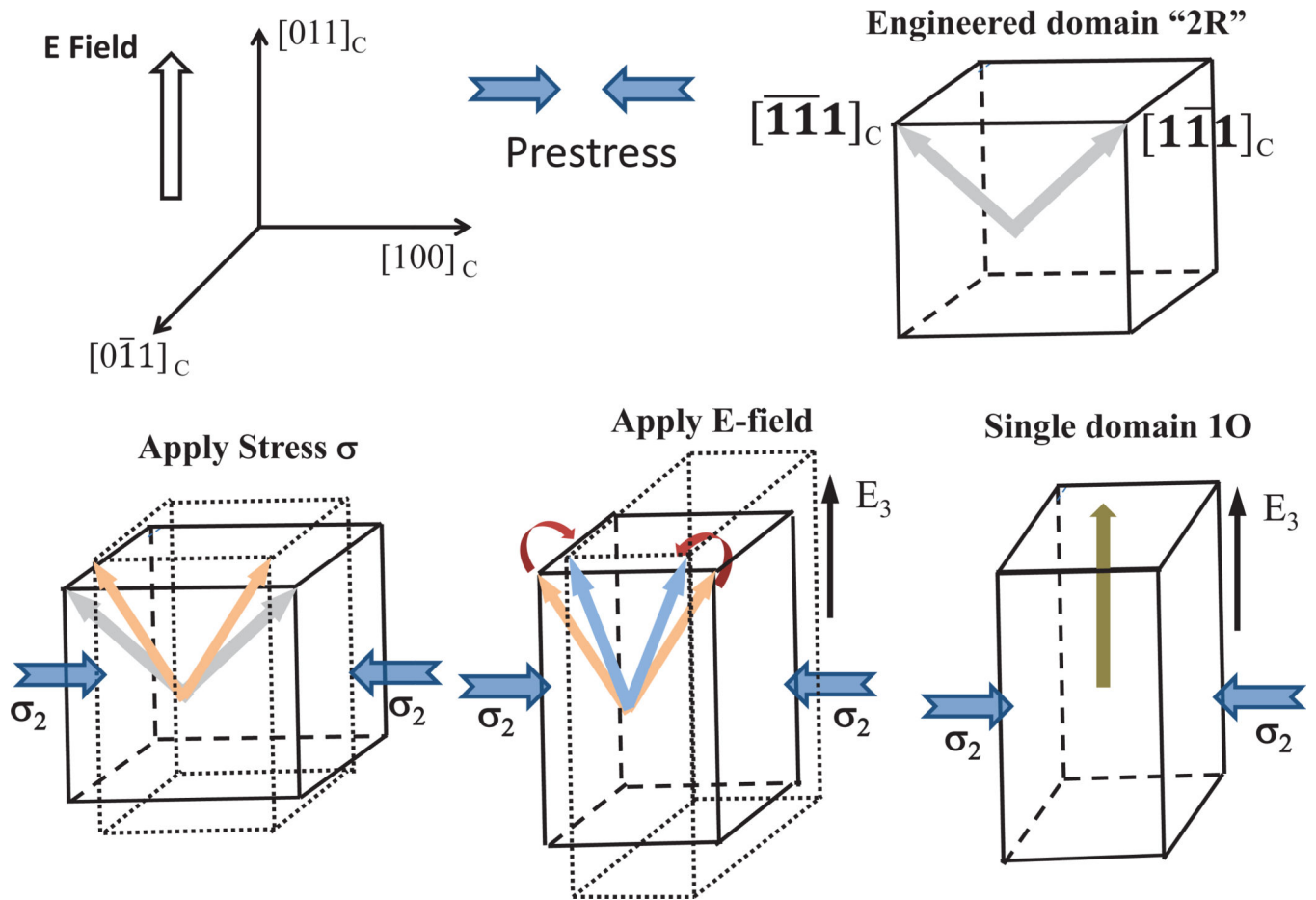


Fig. 29.

(a) Bipolar strain behavior for PIN-PMN-PT:Mn crystals under various prestress levels (small inset shows strain behavior of pure PIN-PMN-PT for comparison), (b) Piezoelectric coefficient d_{32} as a function of prestress for PIN-PMN-PT:Mn and compared to its pure counterparts Reprinted with permission from S. J. Zhang *et al.*, Applied Physics Letters 102, 172902 (2013). Copyright © 2013, the American Institute of Physics [453].

**Fig. 30.**

Polarization rotation for [011] poled crystals under applied transverse compressive stress σ^2 and electric field E_3 . Reprinted with permission from S. J. Zhang *et al.*, Applied Physics Letters 102, 172902 (2013). Copyright © 2013, the American Institute of Physics [453].

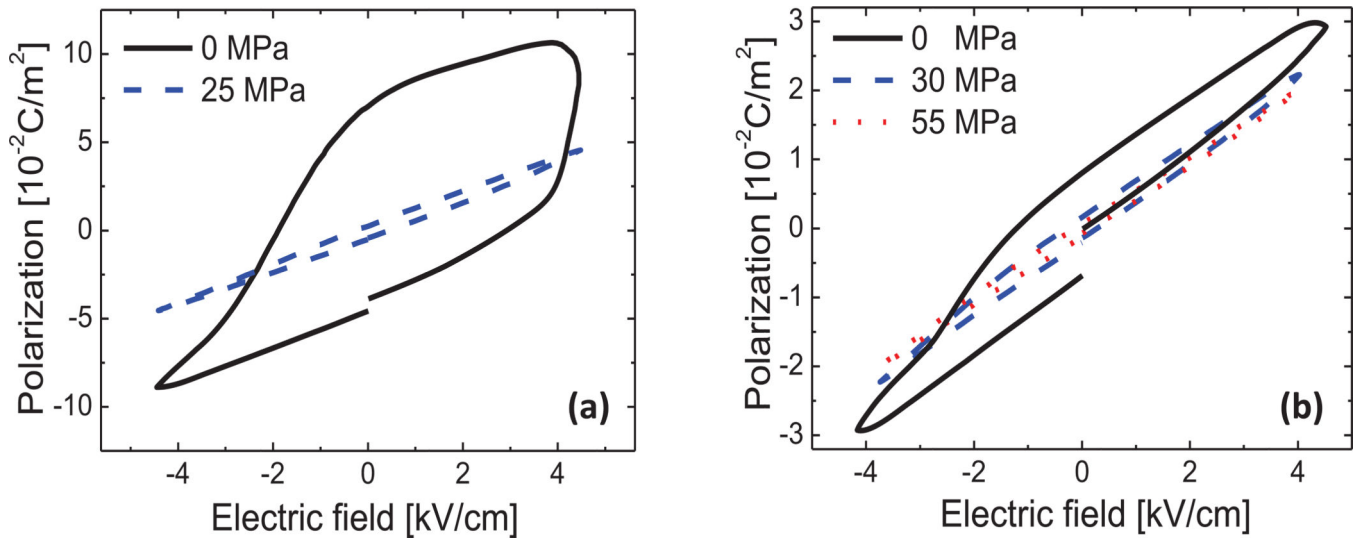


Fig. 31. P-E loops at various uniaxial compressive stress for PIN-PMN-PT crystals with “IT” (a) and “2R” (b) domain states (measured at 1Hz). Reprinted with permission from F. Li *et al.*, Applied Physics Letters 100, 192901 (2012). Copyright © 2012, the American Institute of Physics. [451].

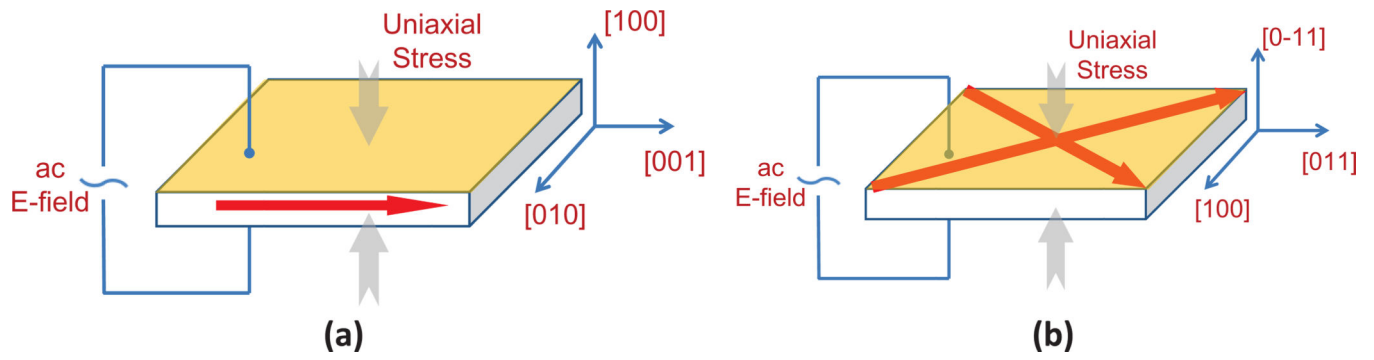


Fig. 32. Schematic of polar vectors for (a) $[001]$ poled tetragonal crystal and (b) $[011]$ poled rhombohedral crystal under perpendicular uniaxial stress. (Figures adapted from ref. [451])

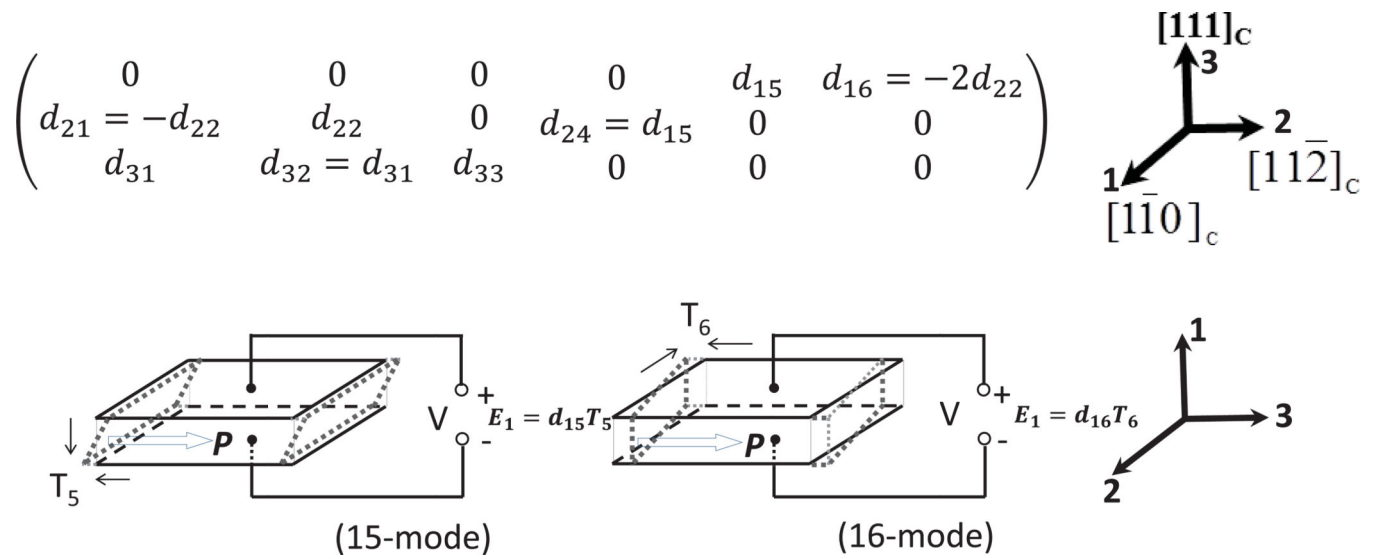


Fig. 33.

Piezoelectric coefficient matrix and cross-talk of piezoelectric 15- and 16-mode in *IR* relaxor-PT crystals. The arrows represent the polarization of *IR* relaxor-PT crystal. The coordinate systems for piezoelectric coefficient matrix and the shear sample are given on right.

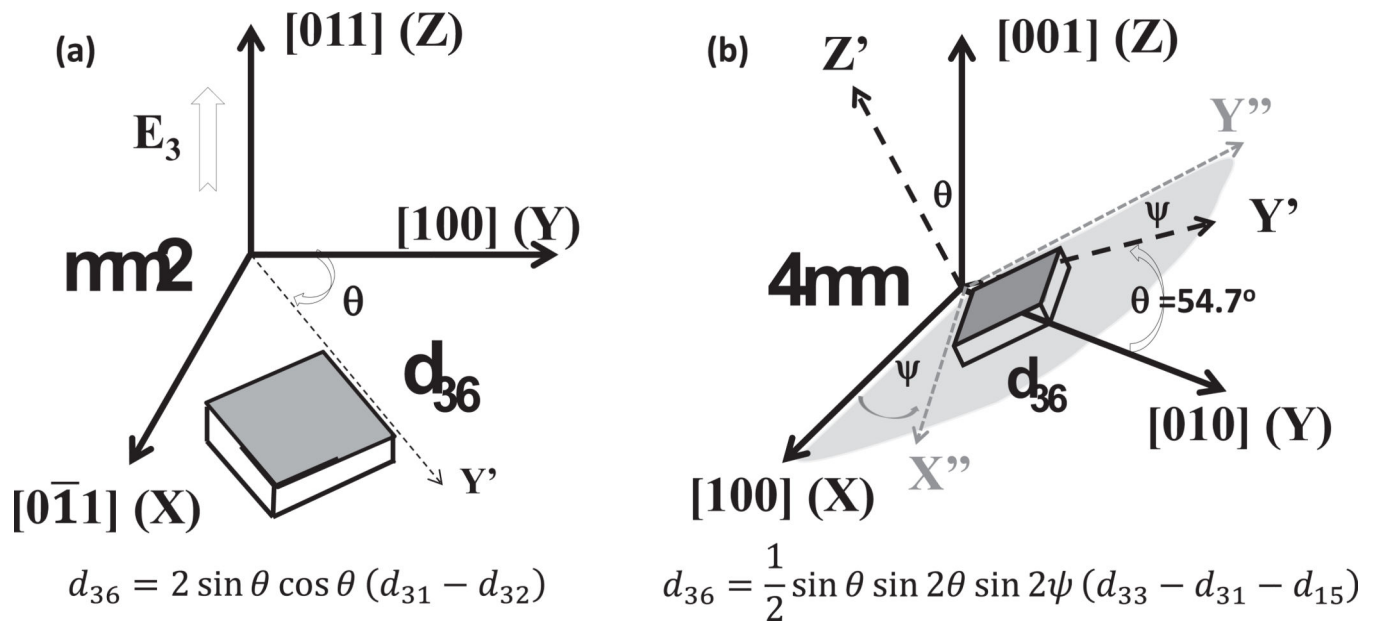


Fig. 34. Schematic of $Zt\theta$ cut sample (a) and $ZXlt\theta/\psi$ cut sample (b).

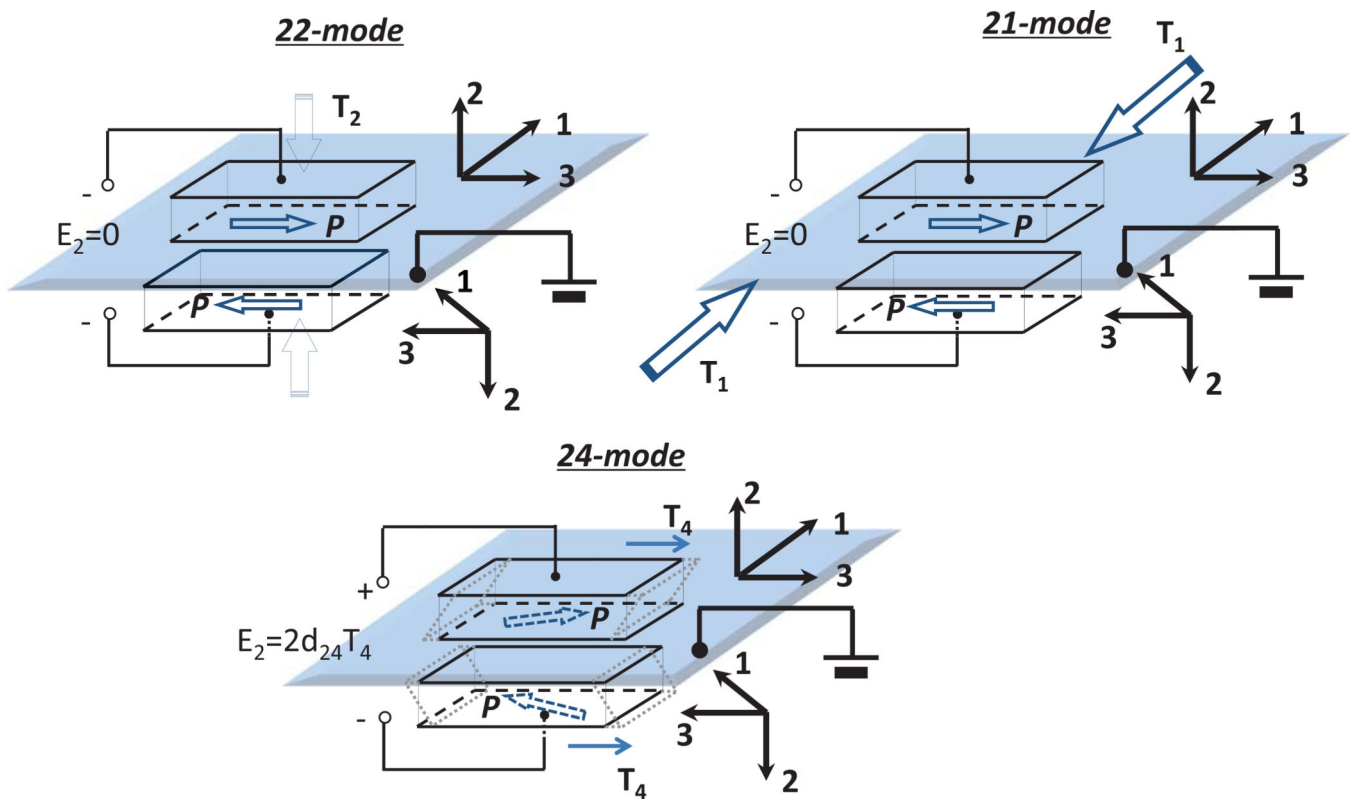


Fig. 35.

The design of 24-mode sensor by using IR relaxor-PT crystal. In this figure, the blue arrows represent the polarization of IR crystal. By this design, the cross-talks from d_{21} and d_{22} piezoelectric effects can be eliminated. (Figures adapted from ref. [466])

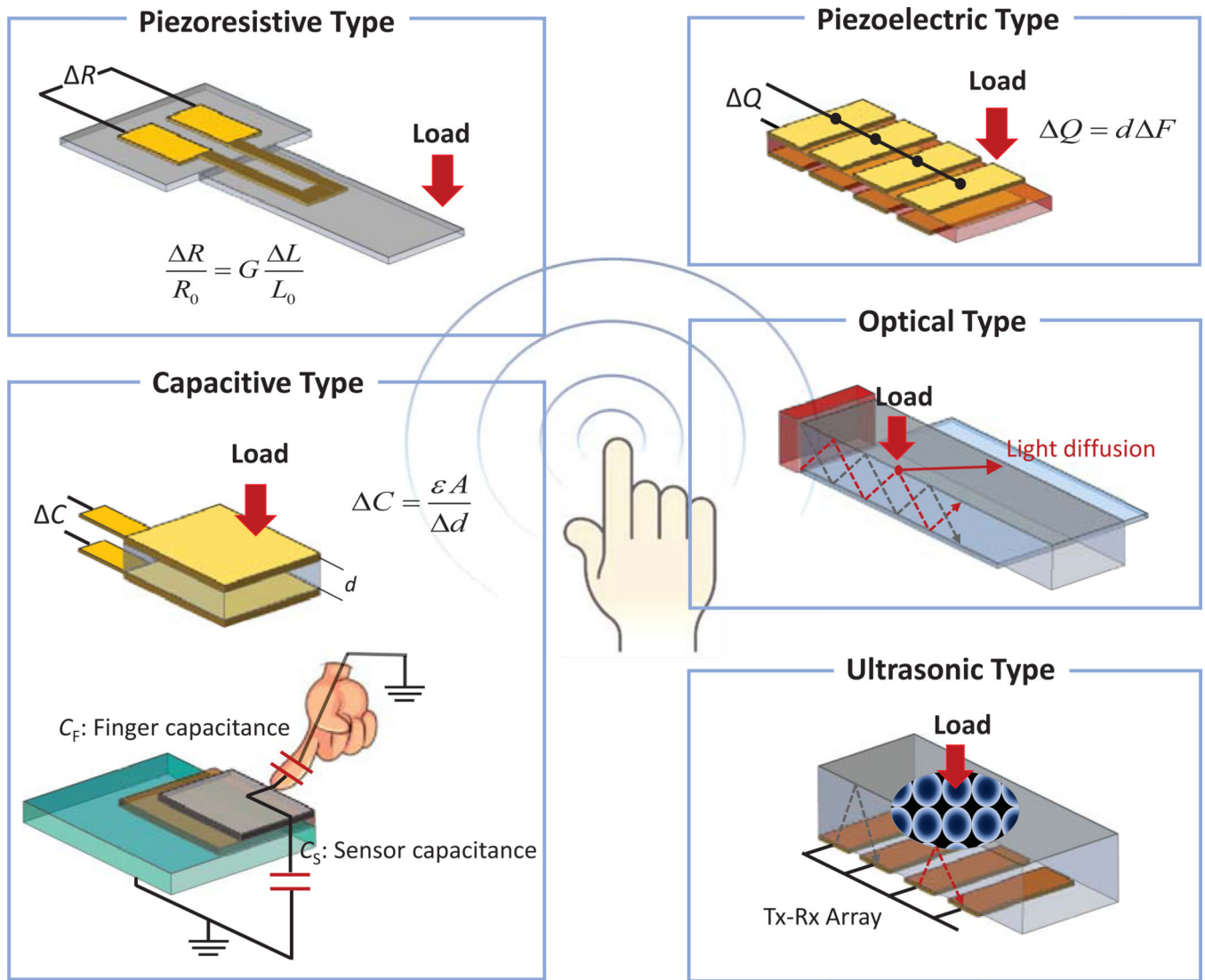


Fig. 36. Schematic of tactile sensing techniques.

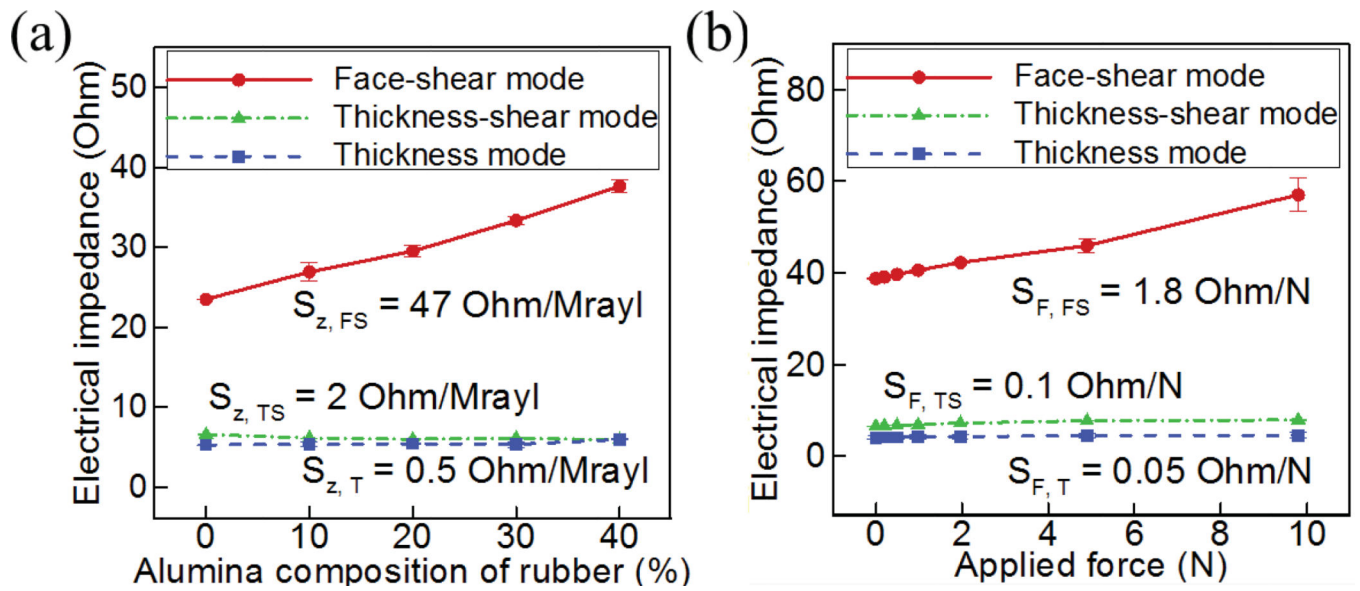


Fig. 37.

Measured electrical impedance at the resonant frequency; impedance change in relation to (a) material properties of sensing layer and (b) applied force. Reprinted with permission from K. Kim *et al.*, Applied Physics Letters 100, 253501 (2012). Copyright © 2012, the American Institute of Physics. [379].

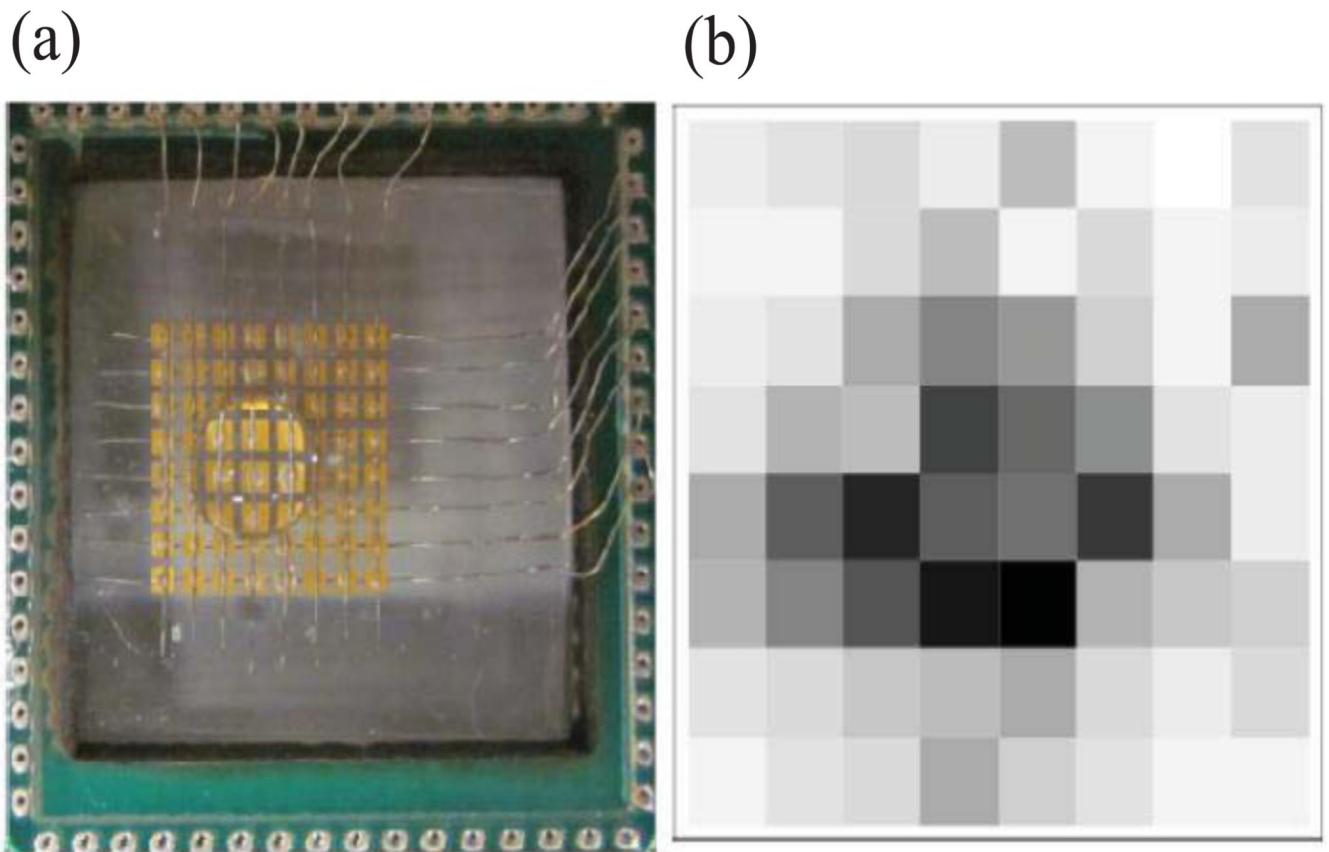


Fig. 38.

(a) Sensor array with an applied water drop; (b) Mapped image for water drop. Reprinted with permission from K. Kim et al., IEEE IUS 2012, 1059 (2012). Copyright © 2012, IEEE. [378].

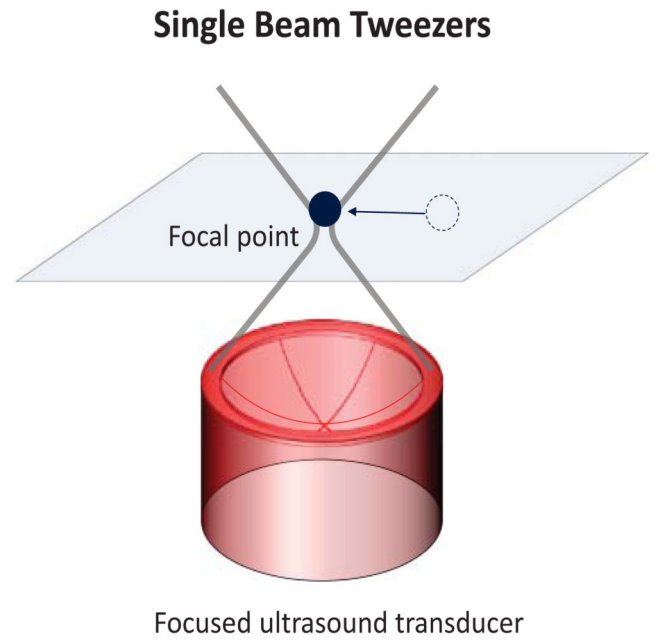
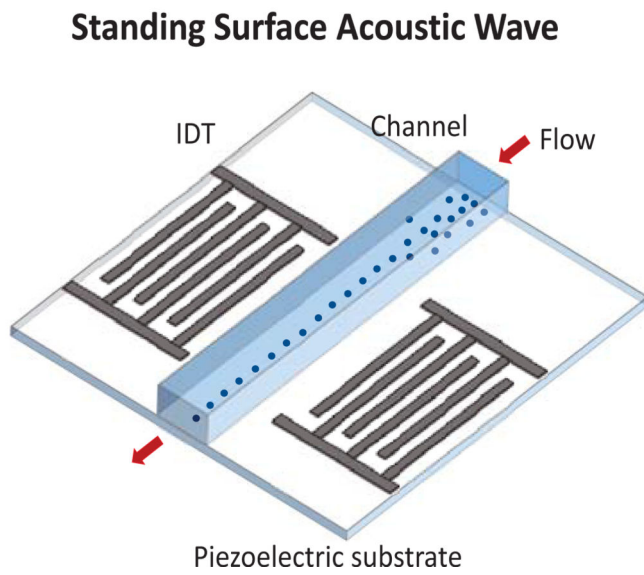
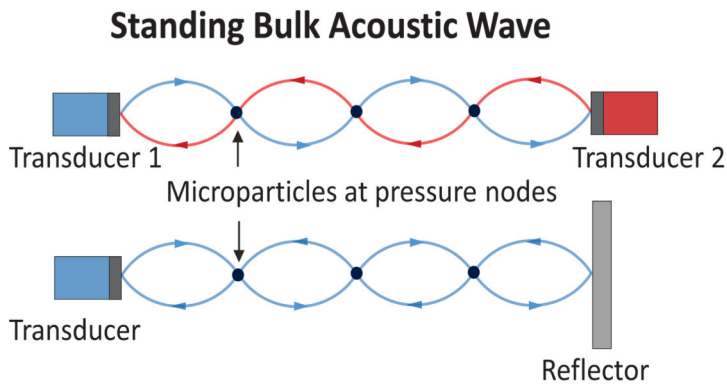


Fig. 39.
Schematic of acoustic tweezers.

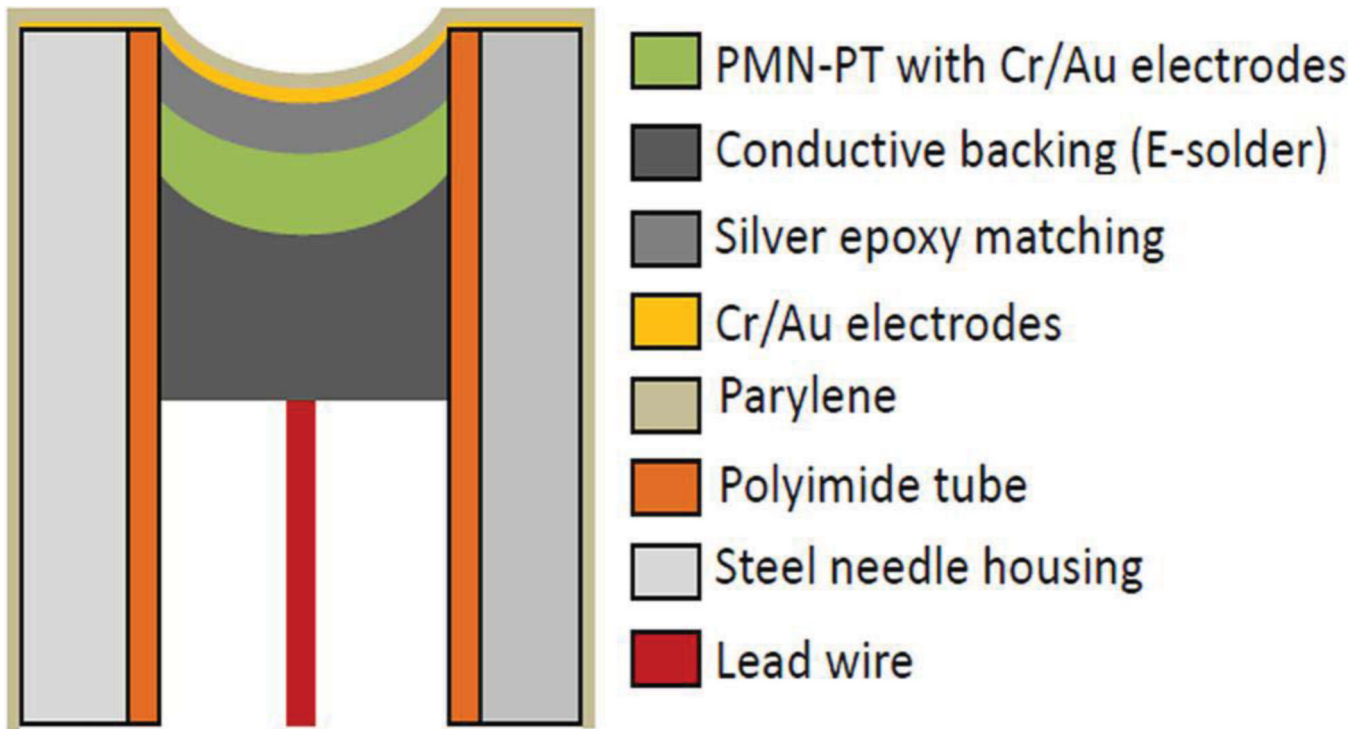


Fig. 40.

Design cross section of a self-focused needle transducer. Reprinted with permission from H. Hsu *et al.*, *Applied Physics Letters* 101, 024105 (2012). Copyright © 2012, the American Institute of Physics. [512].

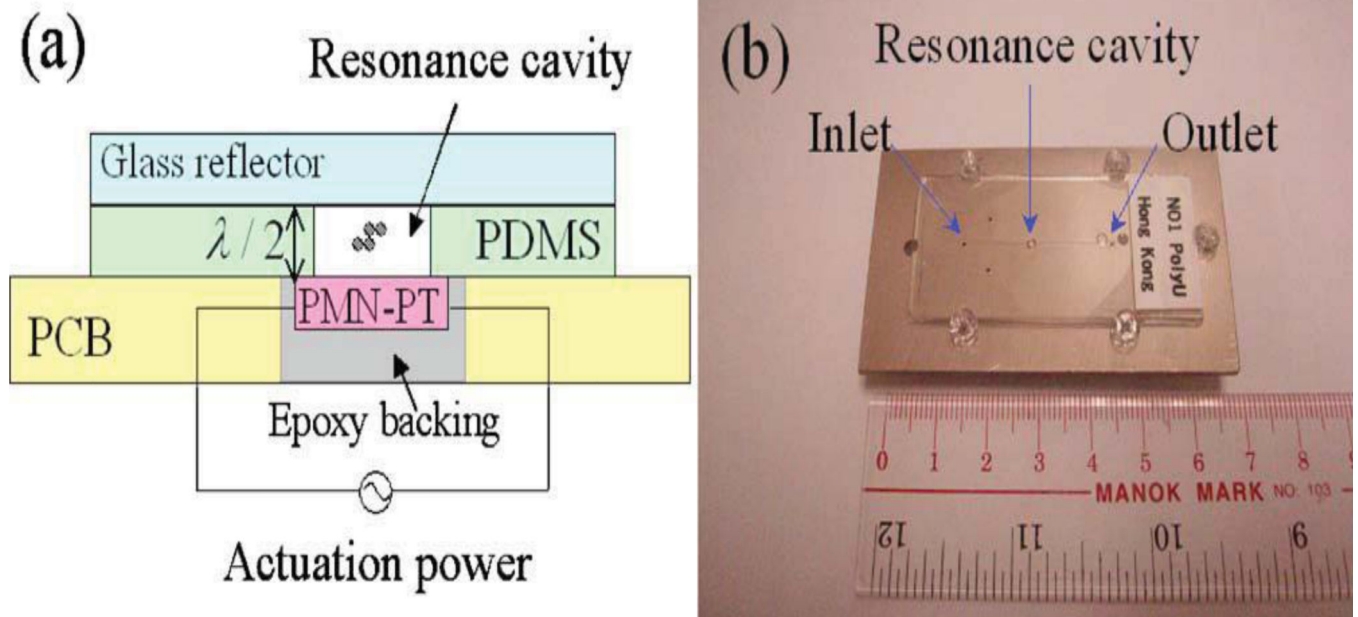


Fig. 41.

(a) Schematic and (b) photograph of the microfluidic device for ultrasonic trapping of microparticles. Reprinted with permission from S. Guo *et al.*, *Applied Physics Letters* 92, 213901 (2008). Copyright © 2008, the American Institute of Physics. [508].

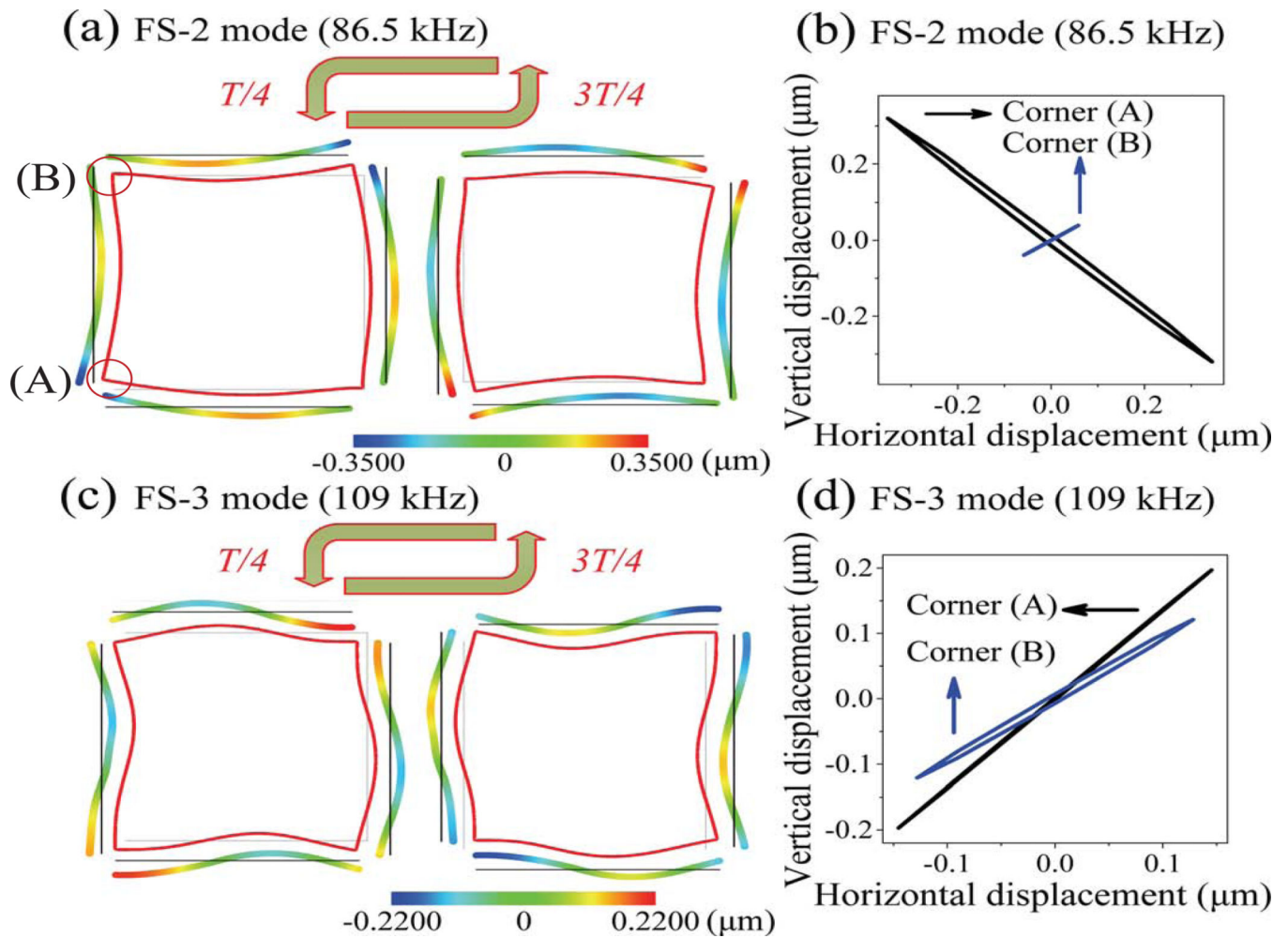


Fig. 42.

Vibration amplitude properties of FS-2 and FS-3 modes, (a) and (c) measured displacement amplitudes (colored contours) and simulated deformation shapes (red contours), corresponding to $T/4$ and $3T/4$ cycle, (b) and (d) measured motion trajectories of the Corners (A) and (B). Reprinted with permission from P. H. Ci et al., Applied Physics Letters 104, 242911 (2014). Copyright © 2014, the American Institute of Physics [382]

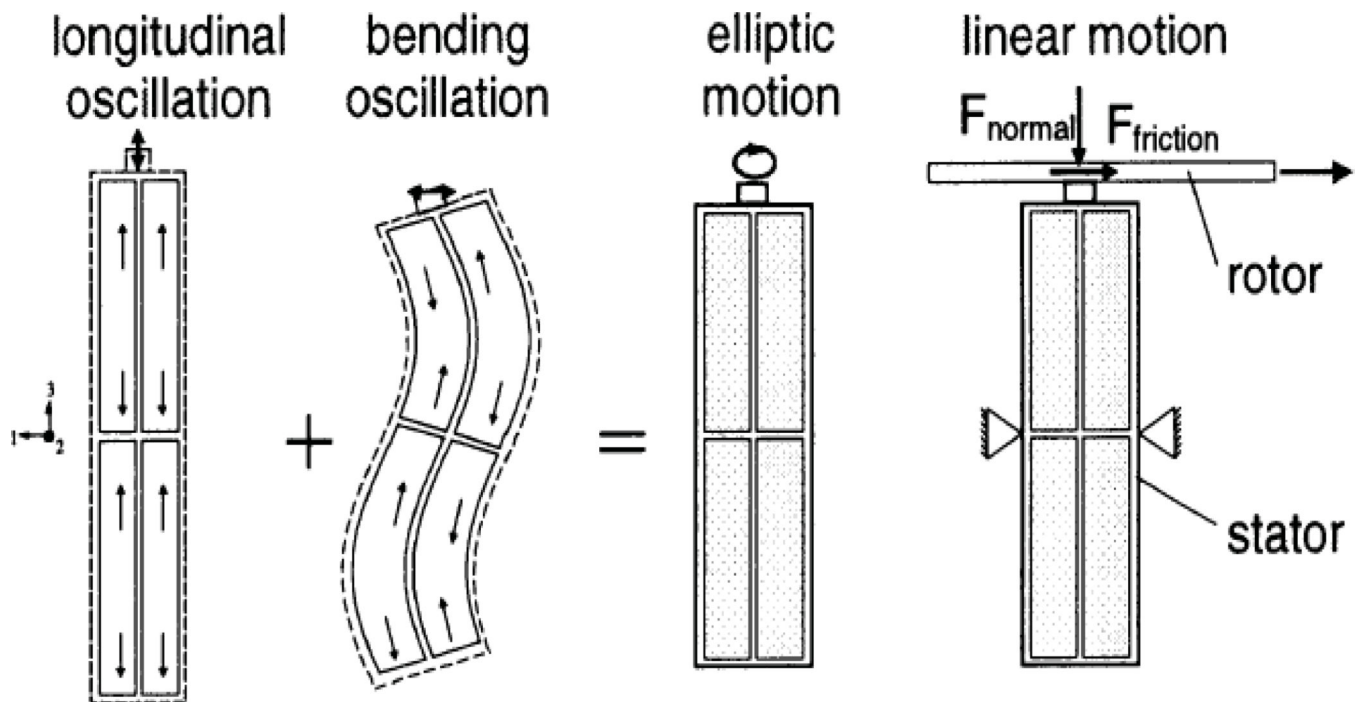


Fig. 43. Schematic drawings of piezoelectric single-crystal PIN-PMN-PT L1-B2 double-mode micro-motor. Reprinted with permission from T. Hemsel and J. Wallaschek, *Ultrasonics* 38, 37–40 (2000). Copyright © Elsevier B.V. (2000) [522].

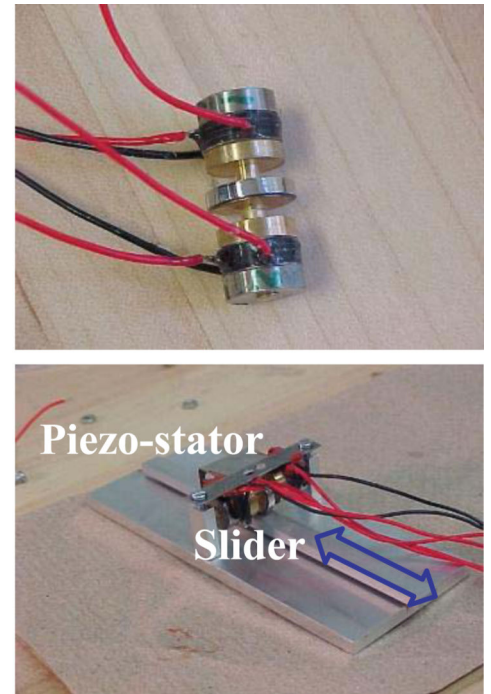
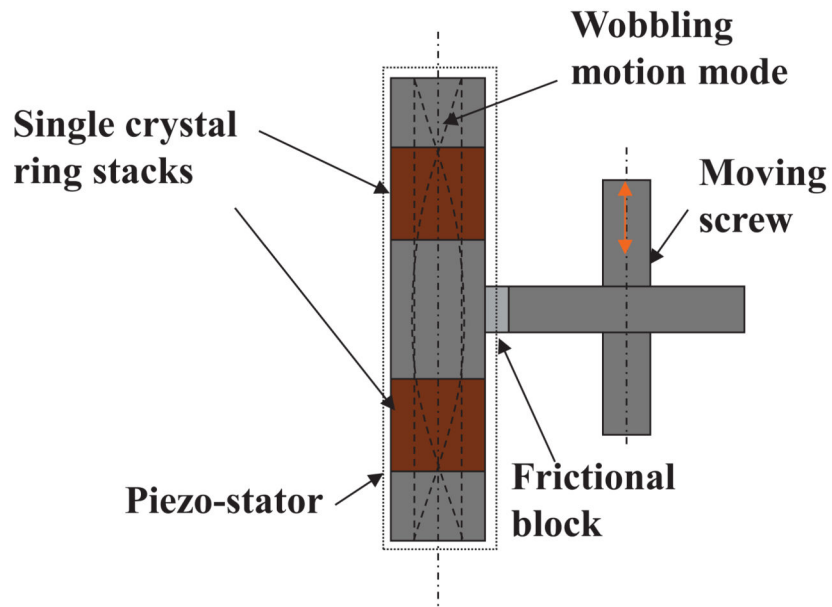


Fig. 44. Wobbling mode piezomotor. Left: schematic view of a wobbling motor; Middle: photograph of an assembled stator with two single crystal stacks; Right: assembled single crystal linear motor. Reprinted with permission from S. X. Dong *et al.*, *Applied Physics Letters* 86, 053501 (2005). Copyright © 2005, the American Institute of Physics [359]

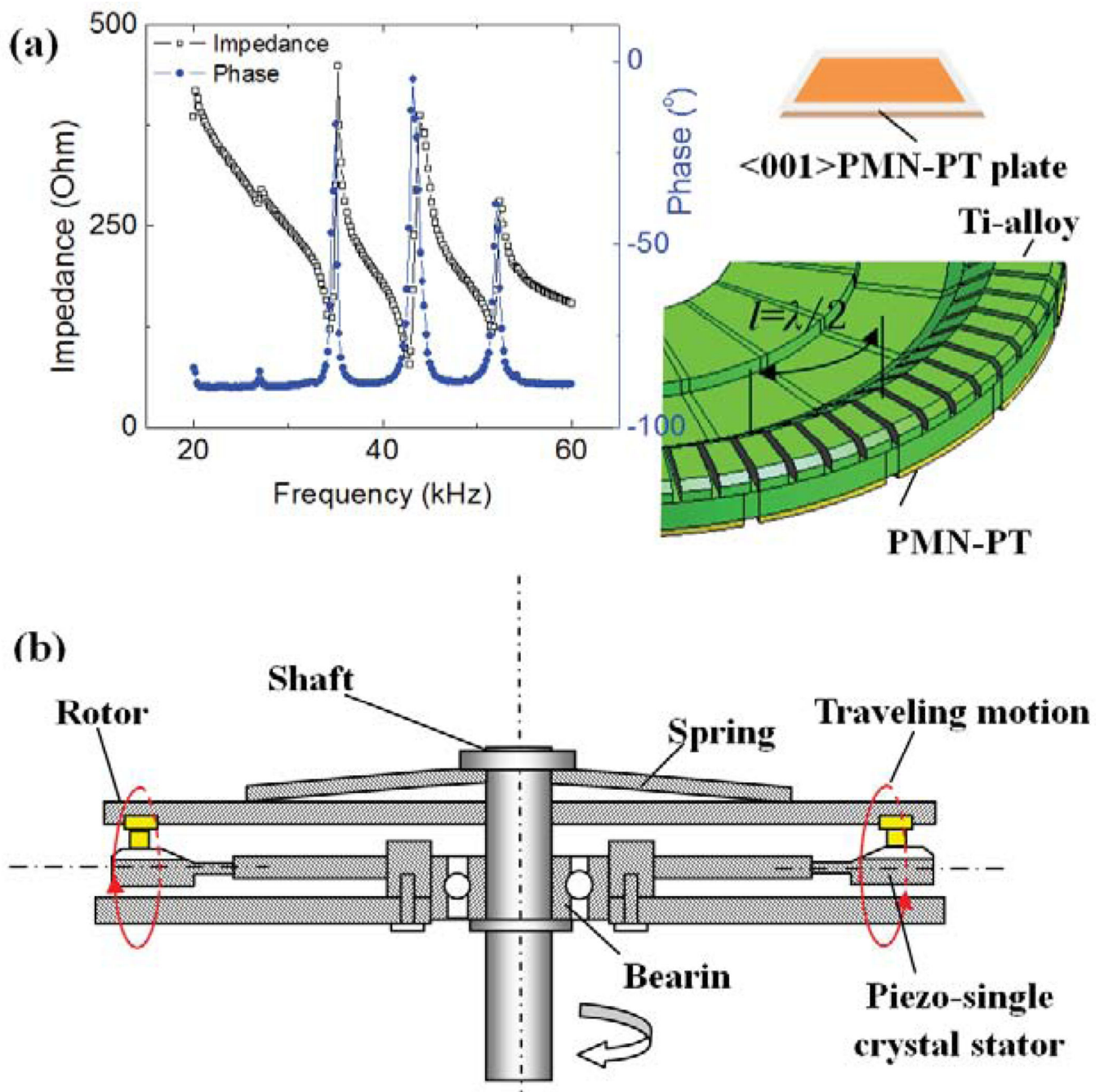


Fig. 45. PMN-PT single crystal/Ti-alloy 9λ traveling wave motor: (a) PMN-PT/Ti-alloy stator and its impedance spectrum; and (b) motor configuration. Reprinted with permission from S. X. Dong *et al.*, Applied Physics Letters 92, 153504 (2008). Copyright © 2008, the American Institute of Physics [366]

Table I

Principal properties of various PZT based polycrystalline ceramics, compared to BaTiO₃ (BT), PbNb₂O₆ (PN) ceramics and LiNbO₃ (LN) crystals. T_C (°C); d (pC/N); s (pm²/N) [70–71]

	T_C	K_{33}^{-T}	K_{11}^{-T}	d_{33}	d_{15}	k_{33}	k_{15}	k_t	E_{33}^E	E_{55}^E	Q_m
PZT2	370	450	990	152	440	0.63	0.70	0.51	14.8	45	680
PZT4	328	1300	1475	289	496	0.70	0.71	0.51	15.5	39	500
PZT5A	365	1700	1730	374	584	0.705	0.685	0.49	18.8	47.5	75
PZT5H	193	3400	3130	593	741	0.75	0.675	0.505	20.7	43.5	65
PZT6B	350	460	475	71	130	0.375	0.377	0.30	9.35	28.2	1300
PZT7A	350	425	840	150	362	0.66	0.67	0.50	13.9	39.5	600
PZT8	300	1000	1290	225	330	0.64	0.55	0.48	13.5	31.9	1000
BT	115	1700	1450	190	260	0.50	0.48	0.38	9.5	22.8	300
PN	570	225	/	85	/	0.38	/	/	25.4	/	15
LN	1150	30	84	6	68	0.16	0.61	0.16	5.02	17	3000

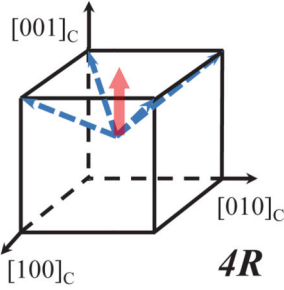
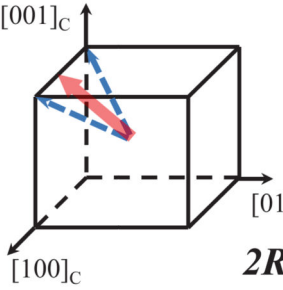
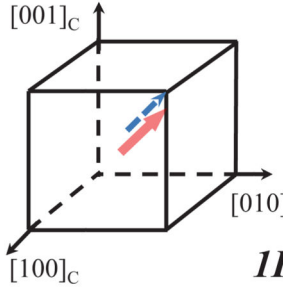
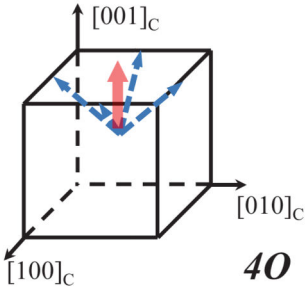
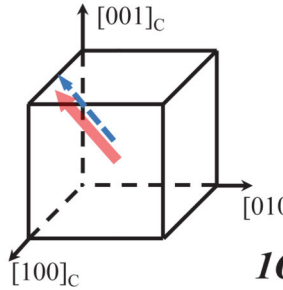
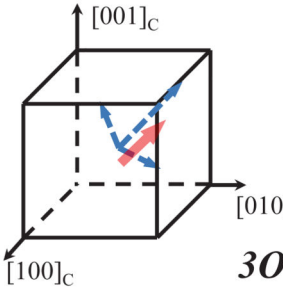
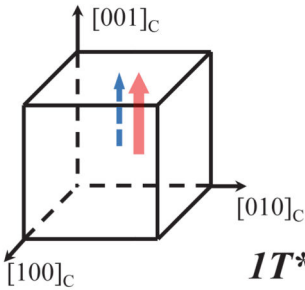
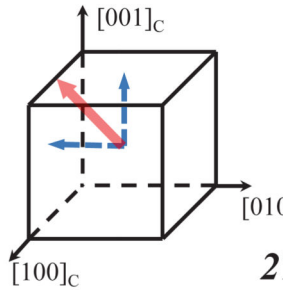
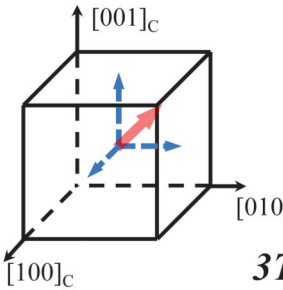
Table II

Property comparison of the three generations relaxor-PT crystals.

Crystal	T_C (°C)	T_{RT} (°C)	E_C (kV/cm)	E_{int} (kV/cm)	K_{33}^{-T}	d_{33} (pC/N)	k_{33}	Q_m
PMN-PT29 (Gen I)	135	96	2.3	0	5400	1700	0.91	150
PMN-PT (MPB) (Gen I)	155	65	2.8	0	8200	2800	0.95	100
PIN-PMN-PT (Gen II)	191	125	5.0	0	4400	1500	0.92	180
PIN-PMN-PT (MPB) (Gen II)	197	96	5.5	0	7200	2700	0.95	120
Mn:PIN-PMN-PT (Gen III)	193	119	6.0	1.0	3700	1100	0.90	800
Mn:PMN-PZT (Gen III)	203	141	6.3	1.6	3400	1100	0.92	1050

Table III

The relationship between the engineered domain configurations and crystal phase/poling directions. The standard coordinate for [111] poled crystals is X:[110]/Y:[112]/Z:[111], while they are X:[011]/Y:[100]/Z:[011] and X:[100]/Y:[010]/Z:[001] for [011] and [111] poled crystals (after [176]).

Symmetry	[001] poled	[011] poled	[111] poled
Phase	$4mm$	$mm2$	$3m$
Rhombohedral	 $4R$	 $2R$	 $1R^*$
Orthorhombic	 $4O$	 $1O^*$	 $3O$
Tetragonal	 $1T^*$	 $2T$	 $3T$

* Single domain crystals mean that the crystals are poled along the direction parallel to their respective spontaneous polarization directions, where almost all domains are aligned along poling directions, the electromechanical properties of crystals can be treated as that of single domain. It should be noted that ideal single domain state is hard to be achieved in perovskite crystals, since it possesses very high levels of electrical and mechanical energies, and is not stable.

Table IV

Property anisotropic ratio for rhombohedral PMN-PT crystals with different domain configurations, and compare to PMN-PT ceramic counterpart, d_{ij} : pC/N, the values in this table are small due to the fact that the listed compositions are in deep rhombohedral phase. [128,233]

PMN-PT Crystal		Piezoelectric property				Mechanical Q_m		Anisotropic ratio			
Poling direction	Domain Configuration	d_{33}/d_{33}^*	d_{31}/d_{31}^*	d_{32}/d_{32}^*	d_{15}/d_{15}^*	d_{24}/d_{24}^*	Q_{33}	Q_{15}	$\epsilon_{11}/\epsilon_{33}$	s_{55}/s_{33}	d_{15}/d_{33}
[001]	4R	1180	-570	-570	122	122	140	30	/	/	/
[011]	2R	860	450	-1150	2160	160	750	40	/	/	/
[111]	1R	97	-43	-43	2380	2380	2000	25	8.4	21.9	24.5
	PMN-PT ceramic	800	-395	-395	1090	1090	75	15	0.81	2.7	1.36

Table V

Property anisotropic ratio for orthorhombic and tetragonal PIN-PMN-PT crystals with single domain states, d_{ij} : pC/N. [293, 306].

PIN-PMN-PT Crystal		Piezoelectric property					Mechanical Q		Anisotropic ratio		
Poling direction	Domain Configuration	d_{33}	d_{31}	d_{32}	d_{15}	d_{24}	Q_{m33}	Q_{m15}	$\epsilon_{11}/\epsilon_{33}$	s_{55}^E/s_{33}^E	d_{15}/d_{33}
[011]	<i>10</i>	350	153	-346	4550	4100	1500	30	5.38	18.8	13.0
[001]	<i>1T</i>	530	-200	-200	2350	2350	1800	30	13.8	1.34	4.43

Table VI

Comparison of the shear vibration modes in various domain configurations, and compared to PZT5 and PZT8 ceramics [340,375]. [hkl]/(hkl)=poling direction/electrode face.

Poling/ electrode	Engineered domain	Crystal	E_c (kV/cm)	E_{int} (kV/cm)	K^T	d_{15} (pC/N)	k_{15}	N_{15} (Hz.m)	Q_{m15}
111/11 $\bar{0}$	1R	Pure PIN	5.0	0	6000	3030	0.93	470	30
110/1 $\bar{10}$	2R	Pure PIN	5.0	0	6500	2800	0.92	570	20
		PIN-Mn	7.3	1.2	4600	2200	0.91	520	30
110/1 $\bar{10}$	1O	Pure PIN	5.5	0	5600	3400	0.95	380	20
		PIN-Mn	9.0	0.6	5800	3500	0.95	360	25
001/100	1T	Pure PIN	12.0	0	15000	2200	0.85	850	20
		PIN-Mn	11.5	1.5	8000	1200	0.77	950	30
		PZT5 (Ceramic)		17	0	1730	0.685	830	15
		PZT8 (Ceramic)		15	8	1290	0.55	1010	150

Table VII

The comparison of thickness shear and face shear in [011] poled rhombohedral PIN-PMN-PT and PIN-PMN-PT:Mn crystals with “2R” engineered domain configuration. [300,333,383] N_r : Resonance frequency constant, where N_{r5} is not necessarily related to the s_{55}^E , while $N_{r36} = \frac{F}{\sqrt{4\rho s_{66}^E}}$ [333]

Crystal	Vibration mode	K^T	$\tan\delta$	d_{eff} (pC/N)	k_{eff}	s^E (pm ² /N)	N_r (Hz·m)	Q_m	Drive stability ratio
PIN	Face shear	4500	0.004	2000	0.81	170	550	180	100%
PIN:Mn	Face shear	3790	0.002	1800	0.80	170	550	350	100%
PIN	Thickness shear	6500	0.015	2800	0.92	161	570	20	40%

Table VIII

Comparison of 1st generation crystals and PZT5H ceramics for medical imaging transducers. T : °C; E_C : kV/cm; d : pC/N; s : pm²/N.

	T_C	T_{KT}	E_C	K_{33}^T	$\tan\delta$	K_{33}^S	k_{33}	d_{33}	k_{33}'	k_t	$\frac{E}{S_{33}}$
PMNT	135	96	2.2	5400	0.004	910	0.91	1540	0.82	0.60	60.0
PZT5H	193	/	7.0	3400	0.02	1470	0.75	593	0.67	0.505	20.7

Table IX

Mechanical Q_m as a function of polarization rotation angle for relaxor-PT single crystals with different engineered domain configurations (the angle between the direction of applied electric field and spontaneous polarization vectors). [141]

Domain configuration	Vibration mode	Polarization rotation angle	Mechanical quality factor	Dielectric loss	Piezoelectric coefficient (pC/N)
4R	longitudinal	54.7°	100~200	0.2~1%	>1500
4O/M	longitudinal	45°	200~400	0.2~1%	>1500
2R	longitudinal	35.3°	500~800	0.2~0.5%	1000~1500
1T/1R	longitudinal	0°	>1000	0.2%	60~500
1T/1R	shear	90°	<30	1~2%	>2000

Table X

Comparison of hard PZT ceramics and single crystals for high power applications [278,300,345].

	T_C (°C)	T_{FF} (°C)	E_C (kV/cm)	E_{int} (kV/cm)	d_{33} (pC/N)	k_{33}	$\tan\delta$	Q_m	S_{33}^E (pm ² /N)	$d \cdot Q_m$ (pC/N)	$k^2 \cdot Q_m$
PIN [001]	191	125	5.0	0	1510	0.92	0.002	150	68.4	226k	127
PIN [011]	192	93/118	5.5	0	1360	0.92	0.002	500	56.8	680k	423
PIN:Mn [001]	192	125	5.0	0.2	1340	0.92	0.002	700	62.4	938k	592
PIN:Mn [011]	197	106/121	5.9	0.3	1050	0.90	0.002	1000	43.8	1050k	810
PZT4	328	/	12	5	289	0.70	0.004	500	15.5	145k	245
PZT8	300	/	15	8	225	0.64	0.004	1000	13.5	225k	410

Table XI

Comparison of the shear vibration modes with the longitudinal and transverse modes for PIN-PMN-PT crystals. [278,300,340]

	K^T	d_{eff} (pC/N)	k_{eff}	s^E (pm ² /N)	Q_m	dQ_m (pC/N)
Thickness shear	6000	3030	0.93	200	30	105k
Face shear	4500	2000	0.82	170	180	360k
Longitudinal	4400	1510	0.92	68	150	226k
Transverse	4360	1780	0.92	101	150	267k

Comparison of hydrostatic properties for various materials [99]. For R -soft+bubbles, R means rhombohedral crystal, soft means epoxy with low Young's modulus and bubbles means micro bubbles being added in the epoxy to further decrease the Poisson's ratio of the epoxy.

Table XII

Material	K^T	d_h (pC/N)	g_h (mVm/N)	$d_h \cdot g_h$ (pm ² /N)	$\tan\delta$
PVDF polymer	13	6	53	0.32	0.02
PbNb ₂ O ₆ ceramic	225	67	34	2.3	0.01
PZT5 ceramic	1800	40	2.5	0.10	0.02
[100] PMN-PT crystal	4436	80	2	0.16	0.004
[011] PIN-PMN-PT "2R"	3000	87	3	0.29	0.002
[011] PIN-PMN-PT "1O"	1500	110	8	0.91	0.002
PZT 0-3 composite	43	7	17	0.11	0.01
PZT 1-3 composite	54	27	56	1.5	0.01
[011] R composite	1500	160	12	1.9	<0.01
[011] O composite	470	100	24	2.4	<0.01
[011] R -soft+bubbles	1500	390	29	11	<0.01
[011] O -soft+bubbles	400	570	161	92	<0.01

Thickness shear properties comparison for [011] poled rhombohedral relaxor-PT crystals (in 2R engineered domain configuration) [233,300,358,375].

Table XIII

Poling/ electrode	Crystal	E_c (kV/cm)	E_{int} (kV/cm)	K_{11}^T	d_{15} (pC/N)	k_{15}	S_{55}^E (pm ² /N)	Allowable field level (kV/cm)	Field Stability Ratio
1 st Generation	PMNT	2.2	0	4240	2160	0.92	147	1.0	45%
2 nd Generation	Pure PIN	5.0	0	6500	2800	0.92	161	2.0	40%
3 rd Generation	PIN-Mn	5.9	0.3	4900	2030	0.90	117	4.0	68%

Piezoelectric properties of $Zr45^\circ$ cut [011] poled and $ZXlt\ 54.7^\circ/45^\circ$ cut [001] poled relaxor-PT crystals, s_{ij} ; pm^2/N ; d_{ij} ; pC/N .

Table XIV

Crystal cut	Domain configuration	Symmetry	$s_{11}^* = s_{22}^*$	$s_{16}^* = s_{26}^*$	s_{66}^*	$d_{31}^* = d_{32}^*$	d_{36}^*	k_{36}^*	K^T
$ZX45^\circ$	2R	<i>mm</i> 2	11.0	21.9	120	364	1650	0.83	3800
$ZXlt\ 54.7^\circ/45^\circ$	4R	<i>4mm</i>	10.3	-14.9	190	2.7	1540	0.61	3800

Table XV

Properties of piezoelectric materials for tactile sensors [486–488].

Type	Material	k_t	d_{33} (pC/N)	$\frac{T}{\epsilon_{33}/\epsilon_0}$	Q_m
Non-resonant	PVDF	0.146	-32.5	7.6	8.5
Resonant	PZT-8	0.48	225	1000	1,000
	Quartz (X cut)	0.10	2.3	4.6	~27,000

Table XVI

Comparison of hard ceramics and relaxor-PT crystals for USM application [278,317,304].

Piezo Materials	k_{31}	d_{31} (pC/N)	T_{33}/ϵ_0	Q_{m31}	$Q_{m31}^2 k_{31}^2 \epsilon_{33} (\times 10^6)$
PMN-PT29 (Gen I)	0.44	-699	5400	120	15
PMN-PT (MPB) (Gen I)	0.59	-1330	8200	80	18
PIN-PMN-PT (Gen II)	0.50	-712	4400	150	25
PIN-PMN-PT (MPB) (Gen II)	0.65	-1337	7240	100	31
Mn:PIN-PMN-PT (Gen III)	0.49	-609	3810	500	229
Mn:PMN-PZT (Gen III)	0.45	-531	3410	600	249
PZT4	0.33	-123	1300	500*	35
PZT8	0.30	-97	1000	1000*	90

* The mechanical Q_{m31} for polycrystalline ceramics is assumed to be the same value of Q_{m31} .